# Numerical and Experimental Study of Flows with Variable Density

**Sepideh Khorshid**

A thesis submitted to University of Ottawa
in partial fulfillment of the requirements for the
Doctorate in Philosophy degree in Civil Engineering

Department of Civil Engineering
Faculty of Engineering
University of Ottawa

**Abstract**

The knowledge of density current behaviours as a result of two or more fluids of different densities interacting is of particular importance in many practical applications. Within the field of hydraulic engineering, examples include buoyant effluent discharges from desalination plants, advancements of saline water under freshwater in estuaries, and flows occurring when a gate is removed at the outflow/inflow of a river. The main goal of this study is to improve the understanding of the mixing patterns of density currents as well as their related numerical simulation. In this study, first, an advanced numerical solver for 2D variable-density shallow water equations is developed and validated where both well balanced and positivity preserving properties are achieved over an unstructured grid. The improved numerical scheme is flexible, and accounts for flooding over irregular bed topographies by using a triangular grid. Second, a numerical study of two-layer stratified flows over an isolated submerged dune is conducted. This part focuses on modeling density currents created when a narrow channel connects two water bodies with different densities and a stratified two-layer flow is subsequently generated. A 3D Large Eddy Simulation (LES) model is developed in OpenFoam and validated with the experimental data to investigate the flow patterns and entrainment. In addition to the LES model, a RANS numerical model is also used, and the results are compared in order to prove the superiority of the LES method in modeling complex mixing behaviours. LES predictions showed good agreement with the experimental measurements, as the LES model was able to capture the KH instabilities. In the third part of this study, the interaction between inclined negatively buoyant jets and waves, such as in the case of brine discharges from desalination plants into the ocean, is experimentally investigated. In addition to discharges in a wave environment, experiments are also performed in a stagnant environment and a wave-current environment in order to compare the results. A combination of the Particle Image Velocimetry (PIV) technique and the full-field Laser Induced Fluorescence (LIF) technique is employed to reveal the mixing patterns. The results showed that the wave motion affects the inclined negatively buoyant jet geometry, resulting in the jet's rotation and an increase in its width. This study led to derivation of empirical formulae calculating terminal rise height and minimum dilution at specific points. In the fourth part, the numerical simulations of 45° inclined dense jets in wavy ambient have been conducted using a finite volume model (OpenFOAM). The selected turbulence models include RNG $k$-$\varepsilon$, realizable $k$-$\varepsilon$; Nonlinear $k$-$\varepsilon$; and LRR. The results of this study are compared to the results from experimental investigations in the third part and comparative figures and tables are presented and discussed. It has been observed that the LRR turbulence model as well as the realizable k-ε model predict the flow more accurately among the various turbulence models studied herein.

## Acknowledgements

I would like to express my deepest gratitude to my supervisors, Dr. Majid Mohammadian and Dr. Ioan Nistor, for their invaluable guidance, advice, and continued supports. I appreciate all their contributions of time and inspiration to make my PhD experience productive and stimulating. None of this would have been possible without their dedication.

I would like to acknowledge my committee members, Drs. Samuel Li, Colin Rennie, Stephanie Moore, and Ousmane Seidou for providing precious suggestions and comments on my thesis. I would like to thank my family for their everlasting encouragement and specially my parents for their unconditional love and support in all my pursuits.

# Table of Contents

## List of Figures

List of Tables

List of Symbols

| | |
|---|---|
| $a_{jk}^{\text{in}}$ and $a_{jk}^{\text{out}}$ | Directional local speeds |
| B | buoyancy flux |
| B (x,y) | Bed elevation at (x,y) coordinate |
| $b_u$ | Velocity spread width, using the $e^{-1}$ notation |
| $C_s$ | Smagorinsky constant |
| F | Flux vector in x-direction |
| Fr | Froud number |
| $Fr_c$ | Froud number of the cross flow current |
| G | Flux vector in y-direction |
| $g'$ | Reduced gravity based on the density difference between the layers in a channel |
| $g$ | Acceleration of gravity |
| H | Wave height |
| h (x,y) | Depth of fluid at (x,y) coordinate |
| $H_s$ | Significant height |
| k | Von Kármán constant |
| k | Wave number |
| $k_L$ | Geometrical model scale |
| L | Wavelength |
| $l_{jk}$ | Length of the *k*-th side of the $T_j$ triangle |
| $l_a$ | Length scale corresponds to wave-current condition |
| $l_m$ | Length scale corresponds to current-only ambient condition |
| $l_w$ | Length scale corresponds to wavy ambient condition |
| M | momentum flux |
| $M_{jk}$ | Midpoint of the *k*-th side of the $T_j$ triangle |
| $\vec{n}_{jk}$ | Normal unit vector of the *k*-th side of the $T_j$ triangle |
| p | Velocity term, $p \coloneqq vh$ |
| p | Pressure |
| q | Velocity term, $q \coloneqq uh$ |
| $Q_j$ | SGS scalar flux |
| Q | discharge volume flux |
| $q_{net}$ | Normalized net flow at the dune crest |
| r | Density term, $r \coloneqq \rho h$ |
| r | Radical distance |
| $R_i$ | Bulk Richardson number |
| Re | Reynolds number |
| S | Source term vector |
| $S_c$ | Minimum dilution at centerline peak |
| $S_{rp}$ | Return point dilution |
| $\lvert\tilde{S}\rvert$ | Strain-rate tensor |
| $t$ | Time |
| $\Delta t$ | Time step of the analysis |
| T | Wave period |
| $T_j$ | Triangular cells of size $\lvert T_j \rvert$ |
| $T_p$ | Peak period |
| U | Flow characteristics vector |
| u | Depth-averaged velocity in x-direction |
| $U_c$ | Maximum velocity along the cross-section |
| $u_c$ | Crossflow velocity |

| | |
|---|---|
| $u_i$ | Velocity of fluid in layer i |
| $u_w$ | Characteristic wave velocity |
| $u_{max}$ | maximum horizontal wave induced velocity at the port |
| $u_r$ | Velocity ratio |
| $\overline{U}$ | Mean velocity of fluid at given point |
| $U^+$ | Non-dimensional velocity |
| $\Delta U$ | Difference in fluid velocities in different layers |
| v | Depth-averaged velocity in y-direction |
| x | x-coordinate of a point in the mesh |
| $X_0$ | Horizontal location of the initial nozzle |
| $X_c$ | Horizontal location of centerline peak |
| $X_t$ | Horizontal location of terminal rise |
| y | y-coordinate of a point in the mesh |
| z | z-coordinate of a point in the mesh |
| $z^+$ | Non-dimensional height |
| $Z_c$ | Centerline trajectory |
| $Z_t$ | Terminal rise height |
| $Z_0$ | The initial nozzle height |
| $\Gamma$ | Scalar diffusivity |
| $(\nabla U)_{i1}$, $(\nabla U)_{i2}$ and $(\nabla U)_{i3}$ | Three non-limited gradients defined by Fraccarollo and Armanini |
| $(\nabla U_b)_i$ | Limited numerical gradient |
| $\overline{\Delta}$ | LES filter width (defined by the grid spacing) |
| $\Delta_{i1}$, $\Delta_{i2}$ and $\Delta_{i3}$ | Eeights for the velocity gradient calculations |
| $\varepsilon$ | Infinitesimal positive number |
| $\sigma$ | Wave frequency |
| $\omega$ (x,y) | Free surface elevation of fluid at (x,y) coordinate |
| $E$ | Constant value |
| $F$ | Froude number |
| $a$ | wave amplitude |
| $\delta$ | Shear layer thickness (also known as vorticity thickness) |
| $\eta$ | Density layer thickness |
| $\rho$ | Average density of the fluid |
| $\tau$ | Triangular domain of analysis |
| $\alpha_e$ | Entrainment rate |
| $\theta_{jk}$ | Normal angle of the *k*-th side of the $T_j$ triangle |
| $\lambda_i[V_{jk}]$ | i-th eigenvalue of the matrix of matrix $V_{jk}$ |
| $\rho_0$ | Reference freshwater density |
| $\rho_a$ | density of the receiving water |
| $\tau_{b,x}$ | Bed shear stress values in x-direction |
| $\tau_{b,y}$ | Bed shear stress values in y-direction |
| $\tau_{ij}$ | SGS Reynold stresses |
| $\tau_{kk}$ | Isotropic part of SGS stress |
| $\emptyset$ | Scalar concentration |

# 1. Introduction and Objectives

## 1.1. Introduction

The occurrence of density currents as a result of the interaction of two or more fluids of different densities is common in nature. When a partition dividing two liquids of different densities is removed, the denser liquid flows beneath the other, thus forming a 'density current'. The density differences may occur as a result of the interaction of the different fluids, with different temperatures, concentrations of suspended sediments, or dissolved solid concentrations, as well as due to different salinity levels between the fluids.

Density currents occur in both natural and man-made environments. The understanding of density current inflows has important applications in reservoir and outflow water quality management. Knowing how contamination, including dissolved salts, excess heat, or suspended solids and chemicals, in an inflow in which they are transported and distributed enables making better decisions regarding the discharge of municipal and industrial waste, cooling waters, and water used for irrigation from different levels within a reservoir. The density current parameters, such as propagation speed, thickness, dilution, and points of plunging and separation, can be used to determine changes in water quality and flow parameters at different depths and time instants.

Density-induced flow phenomena occur in many different forms and have been studied in various fields of science and engineering, including geophysics, hydraulics, heat and mass transfer, oceanography, snow mechanics, oil spill cleanup, and weather prediction. Within the field of hydraulic engineering, examples include buoyant effluent discharges from desalination plants, advancements of saline water under freshwater in estuaries, and flows occurring when a gate is removed at the outflow/inflow of a river.

Another important influence on water quality is human intervention. Some human interventions result in hydrological changes, such as building dams, draining wetlands, and diverting flows. Another example is polluting activities such as the discharge of domestic, industrial, and urban wastewater into water bodies. Domestic and industrial effluents from outfall structures often have different densities than those of the ambient water body, which imposes various changes in the flow and the mixing characteristics of the discharge. An example of such an industrial effluent is

the Ras Laffan Industrial City (RLIC) outfall in Qatar. Most of this country's water is supplied from desalination plants (Darwish and Mohtar 2013), so the water pollution arising from these industrial activities has always been a major concern in Qatar.

Environmental free surface shallow water flows often transport debris and suspended sediment. When such flows enter rivers or other types of water bodies such as lakes, the densities between the two water systems are often significantly different. Moreover, when a narrow channel connects two water bodies with different densities, the lower-density fluid flows over the one with greater density, and therefore a shear interface between the two fluids develops. This exchange phenomenon is commonly observed in estuaries and coastal straits and caused by temperature or salinity differences, which leads in turn to differences in water density. This is, for example, the case with the exchange of the more saline Mediterranean Sea water with the less saline Atlantic Ocean water through the Strait of Gibraltar (Armi and Farmer, 1988). The mixing behaviour of the two water bodies is affected by this difference in densities, and as such, to ensure accurate simulation results, this difference needs to be accounted for.

### 1.2.Research Objectives, Significance, and Background

The main goal of this study is to improve the understanding of the mixing patterns of density currents. To model the mixing of two interacting water bodies, two-dimensional (2D) and three-dimensional (3D) models have been used. However, due to the high computational cost of using 3D models, it is more efficient to use 2D depth-averaged models, if applicable.

In this study, firstly, an advanced numerical solver for 2D variable density shallow water equations was developed and validated. The improved numerical scheme is flexible and accounts for flooding over irregular bed topography using a triangular grid. Secondly, a numerical study on two-layer stratified flows over an isolated submerged dune was conducted. This part focused on modeling the density currents created when a narrow channel connects two water bodies with different densities and a stratified two-layer flow is subsequently generated. A 3D Large Eddy Simulation (LES) model is developed in OpenFoam, and validated with the experimental data to investigate the flow patterns and entrainment.

In the third part of this study, the interaction between inclined negatively buoyant jets and waves, such as in the case of brine discharges from desalination plants and dense effluents from

wastewater treatment plants, was experimentally investigated. This part was followed by a numerical investigation of wave effects on INBJ in the fourth part and a comparison between different turbulence models as well as experimental results was presented. A brief research history along with the novelty and originality of this research is explained in the following sections.

### 1.2.1. Variable Density Shallow Water Flow Equations on Triangular Grids

Shallow-water equations describe the motion of a thin layer of fluid whose vertical dimension is much smaller than its horizontal one (Figure 1.1). A wide variety of such shallow water flows with a free surface under the influence of gravity exist, includes tides in oceans, flood waves in rivers, and dam break waves (Toro, 2001). Shallow water equations are a set of hyperbolic partial differential equations derived by a vertical integration of Navier-Stokes equations. A key assumption in the derivation of shallow water equations is with regard to pressure distribution. Assuming that the vertical acceleration of the water particles has a negligible effect on the pressure, the pressure can be considered hydrostatic. So, the shallow water equations are a time-dependent, two-dimensional system of non-linear partial differential equations (PDEs) of a hyperbolic type (Eq.1.1). However, such flows are not exactly two-dimensional. For example, the flow must have a three-dimensional structure due to the bed boundary layer and associated bottom friction (Vreugdenhil, 1994). Moreover, density stratification due to differences in temperature or salinity causes variations in the third (vertical) direction.

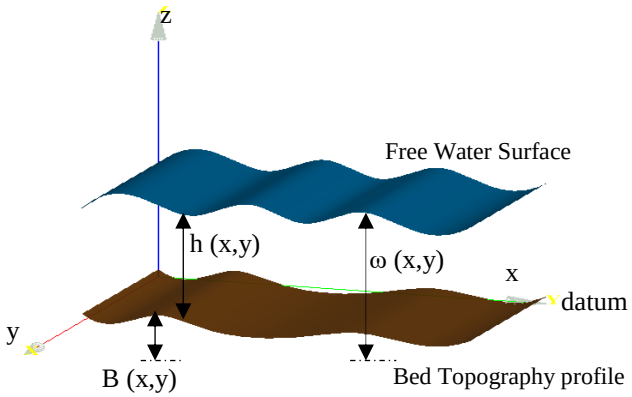


Figure 1-1 Sketch illustrating the definition of the datum, the water depth (h(x,y)), the free water surface elevation (ω (x,y)), and the bed elevation (B (x,y))

Laplace (1775) derived tidal equations, which are a reduced form of shallow water equations, by considering the mass and momentum conservation of water. In the scientific community, shallow water equations are commonly referred to as Saint-Venant (1871) equations, although it appears that Saint–Venant derived only the one-dimensional version (Dronkers, 1964). Boussinesq (1887) and Lamb (1932) derived early versions of shallow water equations (Eq.1.1), and modern derivations of full nonlinear shallow water equations by depth-averaging the Reynolds-averaged mass and momentum conservative equations were proposed by McDowell and O'Connor (1977), Falconer (1993), Liggett (1994), and Dean and Dalrymple (1984), amongst others.

$$\begin{cases} h_t + (hu)_x + (hv)_y = R(x,y,z) \\ (hu)_t + (hu^2 + g/2h^2)_x + (huv)_y = -ghB_x \\ (hv)_t + (huv)_x + (hv^2 + g/2h^2)_y = -ghB_y \end{cases} \tag{1.1}$$

Here, *h(x, y, t)* is the water depth, and *u(x, y, t)* and *v(x, y, t)* are the x-component and y-component of the average velocity respectively, *R(x, y, t)* is the water source term, *B(x, y, t)* is a function describing the bottom topography as shown in Figure 1-1, and g is the gravity constant.
Shallow water equations have numerous applications and have been widely studied, including by Hendershott (1981), George (2008), Toro (2001), and Garvine (1987).

The numerical solution of shallow water equations was one of the early applications of digital computers, and considerable development has taken place since the 1950s. Nowadays, many advanced models are available based on the two-dimensional shallow water equations (SWEs). Solving a shallow water system needs a robust numerical method. The method should preserve the steady-state solutions, as otherwise, the numerical method may lead to significant oscillations.
In a variety of physical problems, there are source terms that are balanced by internal forces, and this balance supports steady state solutions that are stable. Examples include gravity-driven flows like the shallow water flows over a nonuniform ocean bottom. If the solution does not preserve the proper balance between the source terms and internal forces, such as in the case of many classical numerical schemes, they cannot achieve an acceptable level of accuracy. This has been the focus of several research projects, including those by Audusse et al. (2004), Canesttrelli et al. (2010), Bryson et al. (2010), and Bollermann et al. (2013).

Moreover, the numerical method should be positivity-preserving, which means that the water level above the bed should remain positive at all times. This property is crucial when no water is present in parts of the domain or when the depth of the water is very small, as small oscillations may lead to negative depths, eventually resulting in the simulation failing. Several studies have also examined this major property, including Bryson et al. (2011), Kurganov and Petrova (2007), and Chertock et al. (2014).

In this study, a second-order semi-discrete central-upwind scheme is derived which is capable of preserving the "lake at rest" steady state, as well as the positivity of the water depth h. This goal is achieved by extending the scheme from Bryson et al. (2010) to the variable density shallow water equations. Central-upwind schemes are an excellent tool for solving various complex problems in regular domains; however, in practice, one needs to deal with complicated geometries, where the use of triangular grids could be advantageous or even unavoidable. With such a grid, it is much easier to adapt cells to the boundary of the domain and to locally perform any adaption strategy without introducing nonconforming nodes. So, in this study, the variable density shallow water equations are extended for a triangular grid.

Due to the use of the Bousinesq approximation in the formulation suggested by Brice et al. (2010), it is assumed that the density gradients are small. This scheme considers the well-balanced and positivity-preserving characteristics of dense flows. In this regard, the analytical solution is presented over a triangular discretization of the domain by using a higher-order temporal and spatial numerical scheme which is discussed in detail in Chapter 2. The evaluation of the accuracy of the solution along with its different properties was demonstrated for a number of benchmark test cases. Moreover, the ability of the method to solve variable density problems with positivity preserving, and well-balanced properties of the solution are verified.

### 1.2.2. Large eddy simulations of two-layer exchange flows over a bottom sill

The densities of natural water bodies such as oceans, estuaries, and lakes can vary as a result of variations in temperature, salinity, and/or sediment concentrations. Two-layer exchange flows are observed in channels/straits connecting two water bodies with different densities. After leaving the connecting channel, the dense fluid flows along the bottom under the lighter fluid.

Several laboratory studies have been conducted to investigate the hydraulics and behaviour of this type of flow, including Armi (1986), Armi and Farmer (1988), Lawrence (1993), and Morin et al.

(2004). Steady-state solutions for the exchange flow through a connecting channel were developed by Armi (1986) and Lawrence (1990) (Figure 1.2), who studied the hydraulics of two-layer flows and examined the concept of hydraulic controls (also called internal controls). These hydraulic solutions were derived from the conservation of energy and mass in a two-layer fluid. Since the divergence of the volume flux is zero, the difference in velocity between the two layers is constant in the flow direction. The hydraulic equation for the case of a channel with a flat bottom and simple contraction, shown in Figure 1.2, is described in the general form by:

$$\frac{\partial v}{\partial t} + C\frac{\partial v}{\partial x} = D\frac{\partial f}{\partial x} \tag{1.2}$$

where x is the horizontal coordinate and t is the time. If the flow has j layers, then v is a vector with 2j elements, f is a vector with 2 elements, C is a 2j x 2j matrix, and D is 2 x 2j matrix. So, for a two-layer flow with a free surface:

$$C = \begin{bmatrix} u_1 & 0 & g & g \\ 0 & u_2 & (1-\varepsilon)g & g \\ h_1 & 0 & u_1 & 0 \\ 0 & h_2 & 0 & u_2 \end{bmatrix}, v = \begin{bmatrix} u_1 \\ u_2 \\ h_1 \\ h_2 \end{bmatrix}, D = \begin{bmatrix} -g & 0 \\ -g & 0 \\ 0 & Q_1 \\ 0 & Q_2 \end{bmatrix}, f = \begin{bmatrix} h_s \\ b^{-1} \end{bmatrix} \tag{1.3}$$

where $u_n$, $h_n$, $\rho_n$, and $Q_n$, are the velocity, thickness, density, and volumetric flow rate of layer n respectively, as indicated in Figure 1.2, and g is the gravitational acceleration. Subscript 1 refers to the upper layer, and subscript 2 refers to the lower layer, and the variations in the bottom elevation and channel width are $h_s(x)$ and b(x) respectively. The relative density difference is given by $\varepsilon = (\rho_2-\rho_1)/\rho_2$. If $\varepsilon < 1$, the flow is said to be of a Boussinesq type. For the pressure to be hydrostatic, the variations in channel width and depth must be gradual.

This solution is only acceptable if the mixing rate is small, since it has been assumed that there are no diffusion or viscosity effects between the two fluids, which is not realistic. According to the numerical studies by Winters and Seim (2000), considering the diffusion and vertical mixing between the layers is crucial.

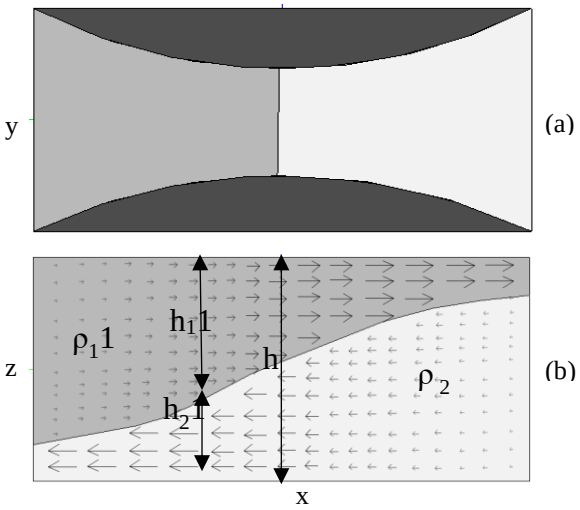


Figure 1-2 Hydraulic solution for exchange flow through a contracting channel studied in Lawrence (1990): (a) channel in plan view; (b) velocity vectors and interface position in elevation view

Lawrence (1993) investigated a steady two-layer flow over an isolated two-dimensional obstacle experimentally and theoretically. Considering the non-hydrostatic pressure distribution, Zhu and Lawrence (2000, 2001) then extended the two-layer hydraulic theory. The new set of equations derived by them was in agreement with the laboratory measurements by Lawrence (1993).

An important aspect of the exchange flows is that interfacial instabilities can develop at the interface between the two layers. These interfacial instabilities play a crucial role in the evolution of density-stratified flows, as they can cause significant entrainment between the fluids and affect the circulation and water quality of both water bodies. As mentioned earlier, several studies reported that shear instabilities at the interface of exchange flows, such as Kelvin-Helmholtz (KH) billows, are largely responsible for vertical mixing (Fernando, 1991; Pratt, 1987).

Studying two-layer exchange flows over a smooth bottom sill experimentally, Morin et al. (2004) observed that there are large periodic fluctuations in the measurements of the flow rate, which were due to the generation of KH instabilities. Fouli (2006) continued to study the growth and development of interfacial KH instabilities in a two-layer exchange flow over a sill. Measurements of KH Instabilities initial growth rate and the wavelength were also obtained in his study.

In comparison with the experimental studies on the internal hydraulics theory and the interactions between the geometry of the bottom and the flow patterns and development of a shear interface, the number of numerical simulations is much smaller.

The first numerical study that considered the propagation of exchange flows over a sloping topography was done by Ozgokmen et al. (2004). Using a parallel high-order spectral-element Navier–Stokes solver, they carried out 2D and 3D simulations of an overflow and then compared the results. It was shown that in the 2D simulations, the propagation speed was approximately 20% slower than that of the 3D experiments, the head growth rate was 3 times as large, and the entrainment parameter is up to 2 times larger than those in the 3D experiments. The differences between the 2D and 3D simulations are entirely due to internal factors associated with the truncation of the Navier–Stokes equations for a 2D approximation.

Their investigation was extended by Ozgomen and Fisher (2008) for the case of a current with a specific density propagating into a temperature-stratified ambient fluid. Their study focused on temporal changes in the structure, entrainment, and front propagation speed of the current.

Ottolenghi et al. (2014) showed that the thickness of the current head and magnitude of flow reversal is affected by slope angle. They also conducted a large-eddy simulation (LES) to investigate entrainment in lock exchange gravity currents (Ottolenghi et al. 2016), and it was observed that ambient fluid entrainment into the dense layer is reduced by increasing both the initial lock aspect ratio (height to length ratio) of the dense fluid and the bottom slope.

A numerical-experimental study on two-layer stratified flows over an isolated dune and an array of submerged dunes was conducted by Anta et al. (2016), who used the PIV and LIF techniques to measure velocity and density fields in a laboratory flume. Then, the experiments were reproduced using a 3D-RANS model in ANSYS CFX. The model was able to predict the global behaviour of exchange flows, since the time-averaged velocity and concentration profiles were properly reproduced. However, variables such as the shear layer thickness and the Richardson number, as well as the entrainment rate, were not accurately predicted. Compared to the Reynolds-averaged Navier-Stokes (RANS) equations, an LES can be expected to obtain more accurate results for the mixing behavior. RANS equations describe flows in a statistical sense, typically leading to time-averaged pressure and velocity fields, which is the reason that they are not able to distinguish between periodic large-scale and turbulent small-scale features of a flow field. This leads to an inadequate description of unsteady phenomena when the flow field is governed by both large-scale and small-scale features, such as in the case of a flow over an obstacle. An LES, on the other hand, operates with unsteady fields of physical values, while the governing equations are

Navier-Stokes equations, but contrary to the RANS method, spatial filtering is applied and the turbulent stresses are divided into resolved and modelled stresses. It should be mentioned that the main disadvantage of an LES is the high computational costs resulting from the fine grids, in addition to the fine time steps used for prediction of the instabilities.

Nourazar and Safavi (2017) carried out a two-dimensional LES simulation on a constant flow density current flowing on an inverse slope. The results of the simulation showed that as the inverse slope of the inclined surface increases, the mixing in the body of the dense fluid with the ambient fluid increases at the beginning of the slope because of vortices generated by the flow reversal, whereas mixing in the head of the density current generally decreases.

In the current study, 3D Large Eddy Simulations are employed to investigate the flow structure and evolution of a bottom-propagating gravity current in a rectangular horizontal plane channel containing a dune on the channel bottom. The dynamic Smagorinsky sub-grid-scale model is used to improve the mixing accuracy of the flow field. As mentioned earlier, Ozgokmen et al.'s (2004) investigations proved that there are some differences between 2D and 3D simulations, which arise because of internal factors associated with the truncation of Navier-Stokes equations for a 2D approximation. The differences become more prominent in cases in which the topographic slope varies in the span-wise direction and there is an obstacle. Moreover, for the sake of comparison, a RANS numerical simulation is also performed in this study. The results of both numerical simulations are then compared with measured values in a series of experiments which were carried out at the R+D Centre of Technological Innovation in the Building and Civil Engineering (CITEEC) department of the University of A Coruña (Spain).

### 1.2.3. Effects of Waves on Mixing Processes

With the extensive development of desalination and power plants and petrochemical plants and refineries in recent years, it is necessary to evaluate their environmental impacts. Desalination plants remove the dissolved minerals from coastal water bodies and produce effluents with different densities than the ambient water, which can lead to major problems in the ecosystem. If the effluent has a lower density than that of the ambient water body, the effluent will rise, and the jet is called positively buoyant, while if the effluent has a higher density than that of the ambient water body, the effluent tends to sink and is called a negatively buoyant jet (Figure 1.3)

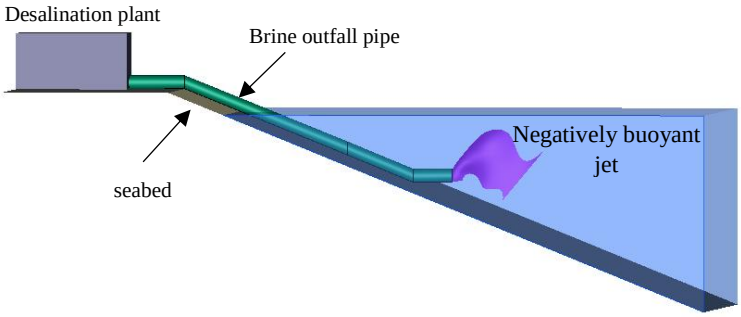


Figure 1-3 Dispersion of the effluent from a negatively buoyant jet

The mixing process of these flows with the ambient water is of high importance due to the impact on the natural habitat of marine species. The subject of submerged negatively buoyant discharges has received a great deal of attention over the past few decades, and has been the focus of several studies via experimental tests as well as robust 3D numerical models including Zeitoun et al. (1970), Roberts and Tom (1987), Oliver et al. (2013), Lai and Lee (2012), etc. According to Bleninger et al. (2009), the characteristics and behavior of an effluent after release depend on the dimensions and orientation of the discharge structure, the physical and chemical properties of the effluent, the characteristics of the ambient water, and the physical and hydrological condition of the ambient water. When a jet is discharged into coastal waters, due to the existence of waves and currents, more complex mixing processes may occur, and thus significantly affect the jet dilution processes compared to the case when the jet is discharged into a stagnant ambient environment. According to Chin (1987), the surface dilution, S, of a submerged buoyant jet in an unstratified stagnant environment can be written in the form below:

$$S = f_1(D, U_0, g_0, H, \theta_1, \theta_2, A, T, g) \tag{1.4}$$

where D is the diameter of the jet, $U_0$ is the jet velocity, and $g_0$ is the effective gravity defined by:

$$g_0 = \frac{\Delta\rho_0}{\rho_0} g \tag{1.5}$$

H is the depth of the discharge, $\theta_1$ is the discharge angle relative to the horizontal plane, $\theta_2$ is the discharge angle relative to the direction of wave propagation, A is the wave amplitude, T is the wave period, $\rho_0$ is the initial density of the effluent, and g is the acceleration due to gravity. It is assumed that the discharge is turbulent, and therefore viscous forces are not significant. It should be noted that, in turbulent plumes, the Reynolds number continually increases along the axis of the plume, and a turbulent discharge produces a turbulent plume.

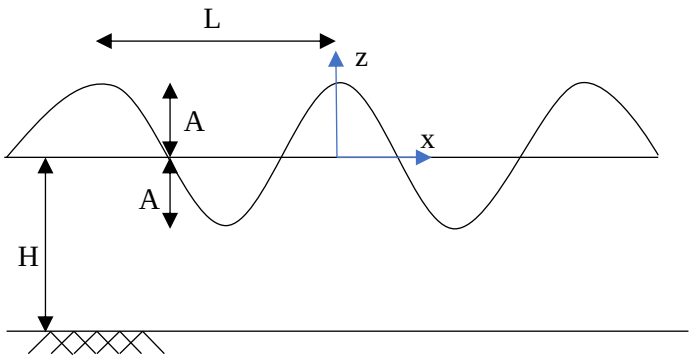


Figure 1-4 Wave parameters

Eq. (1.4) can also be formulated in terms of the discharge momentum flux, M, buoyancy flux, B, and volume flux, Q, as below:

$$S = f_2(M_0,\ B_0, Q_0, H, \theta_1, \theta_2, A, T, g) \tag{1.6}$$

where

$$Q_0 = \frac{U_0 \pi D^2}{4} \tag{1.7}$$

$$M_0 = \frac{{U_0}^2 \pi D^2}{4} \tag{1.8}$$

$$B_0 = Q_0 g \tag{1.9}$$

As shown in Figure (1.5), Chin (1987) also classified the extent of the influences of a surface wave on a water column by using the depth-to-wavelength ratio H/L. This figure shows that, for values of H/L < 0.05, the wave affects the entire depth uniformly. For 0.05 < H/L < 0.5, which is the typical case in the ocean environment, the wave effects on the entire depth are nonuniform, and therefore it is expected that the influence of waves on a rising plume increases as the plume rises. And finally, for H/L > 0.5, the wave affects only part of the depth.

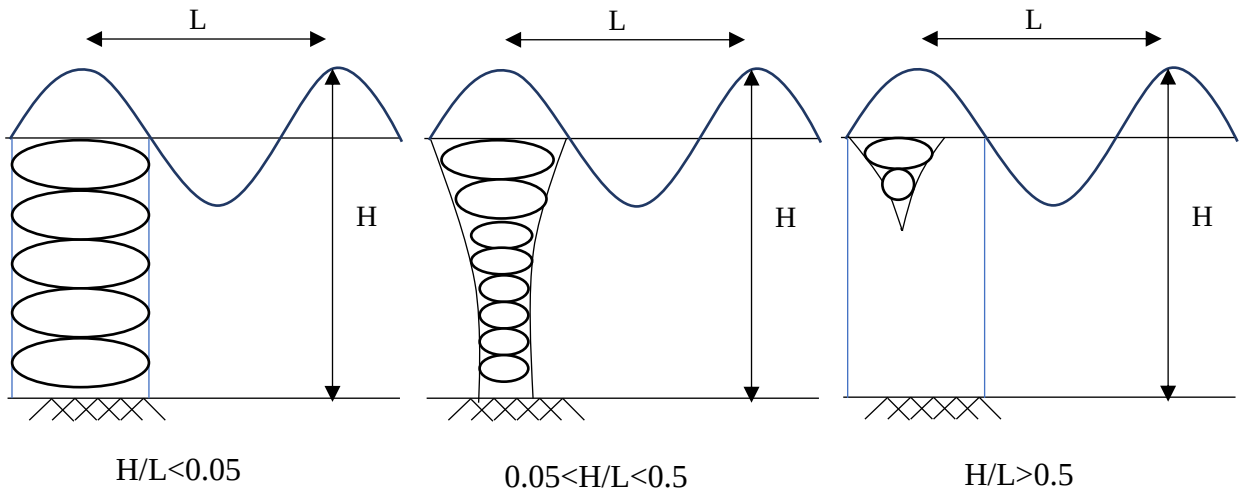


Figure 1-5 Extents of wave effects on water particles

Chin (1987) also conducted an experimental investigation considering the influence of surface waves on jets. Dilution was determined by measuring the conductivity where the plume surfaces and comparing this value with the conductivities of known dilutions, and the results of the experimental investigation showed higher surface dilution of a jet in a wave environment compared to that of a jet in a stagnant ambient environment.

Koole and Swan (1994) considered the dispersion of a 2-D non-buoyant jet discharged into an ambient environment with gravity waves, and the results suggested that oscillatory wave motion has a significant effect upon both mean velocity profiles and the magnitude of turbulent fluctuations. It was also shown that the zone of flow establishment is shorter, and that forced entrainment increased in wave-induced mixing. Tam and Li (2008) reported that, in wavy environment, the centreline of the velocity shows a rapid decrease, while waves enhance jet width and turbulence.

Chyan and Hwung (1993) used a LIF-LDV system, which is a laser Doppler velocimeter modified by laser-induced fluorescence technique, to simultaneously measure two-dimensional jet velocity field and tracer concentration. They spotted three different regions, starting from the simple jet origin. The first region is the jet deflection region (JDR), where the jet is dominated by its initial momentum and preserves its shape, and the wave also forces the jet to oscillate almost like a rigid body. The reason for this is that the transversal dimension of the jet is quite small close to the jet origin compared to the wavelength, and the variation in wave horizontal velocity is not large. The second region was termed the transition region (TR), while the third one was called the developed

jet region (DJR). In the DJR, Chyan and Hwung (1993) as well as Chin (1987) observed a periodic deflection in vertical and horizontal simple jets, and suggested that the observed higher dilution is due to this deflection.

The interaction between wave motion and jets has been largely investigated and discussed, including by Ryu et al. (2005), who measured the velocities of a neutrally buoyant turbulent round jet discharged horizontally into a wavy ambient environment by using particle image velocimetry (PIV). They found that the jet centerline velocity decays rapidly and the jet width increases as the height of the incident wave increases. Also, Hsiao et al. (2011) investigated the mean flow and turbulence properties of a neutrally buoyant turbulent round jet discharged into a wave field, and showed that the mean jet width, turbulence intensity, and Reynolds stress increased significantly when the jet was under the effects of waves.

However, these studies did not consider the buoyancy effect. Most studies on buoyant jets have focused on jets that are discharged vertically (e.g., List, 1982; Wang and Law, 2002) and horizontally (e.g., Lee and Neville-Jones, 1987; Shao and Law, 2010) into a stagnant environment. All the mentioned studies focused either on neutrally buoyant jets in a wave environment or on buoyant jets in a stagnant environment or uniform flow, and few studies have been conducted on buoyant jets in a wave environment, including (e.g., Lin et al., 2013). Extending the experiments on neutrally buoyant jets in waves by Hsiao et al. (2011), Lin et al. (2013) included both positively and negatively buoyant jets in one wave condition in order to investigate the buoyancy effects on a turbulent round jet in wavy environment, and used PIV to measure the evolution of buoyant jet-wave interactions. In summary, their results showed that the buoyancy effect has a considerably smaller influence than the wave dispersion effect on the enhancement of jet diffusion.

To the best of the author's knowledge, the interaction between inclined negatively buoyant jets and waves, under different wave conditions has never been investigated before. Therefore, in this part of the study, a series of experiments has been conducted in a wave flume with a wavemaker, reproducing scaled-down wave data from the buoy at Cabo de Palos, Alicante, Spain. The range of data used was chosen to simulate some typical Mediterranean wave climates with respect to the kinematic similarity. Particle Image Velocimetry (PIV) and the full-field Laser Induced Fluorescence (LIF) technique were used to investigate both the velocity fields and also investigate the diluting effect of surface waves on buoyant plumes.

### 1.2.4. Numerical Simulation of the Effects of Waves on Mixing Processes of Negatively Buoyant Jets

Although the most reliable information about the mixing behaviour of buoyant jets can be obtained by measurements, experimental investigations using full-scale equipment are often expensive, and using scaled models and conditions and extrapolating their results to full scale is not free from error. Therefore, an alternative is to use numerical modeling for the prediction of concentration/temperature transfer and mixing processes, and so conservation equations for concentration, momentum, and temperature for incompressible flows are described below.

**The continuity equation:**

The continuity equation states that the rate at which mass enters a fluid element (Figure 1-6) is equal to the rate at which mass leaves the system plus the accumulation of mass within the system (Malalasekera and Versteeg, 1995).

$$\frac{dm}{dt} = 0 \tag{1.10}$$

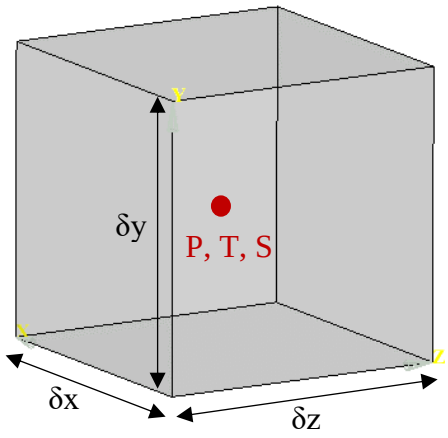


Figure 1-6 Fluid element for conservation law

Then, the continuity equation is written as:

$$\nabla(\rho\vec{U}) = 0 \tag{1.11}$$

$$\frac{\partial}{\partial x}(\rho u) + \frac{\partial}{\partial y}(\rho v) + \frac{\partial}{\partial z}(\rho w) = 0 \tag{1.12}$$

where $\rho\vec{U} = (u, v, w)$ (u and v are the mean velocity components in the x and y directions, respectively). The Navier-Stokes equations describe conservation of mass and momentum. For the purpose of this thesis, we limited the attention to incompressible fluids, which means that the fluid density is independent of pressure (P).

The momentum equation:

The momentum equation is defined as: the rate of increase of momentum of a fluid particle equals the sum of forces on the fluid particle. The momentum equations for a three-dimensional system may be written as follows:

$$\frac{\partial u}{\partial t} + u\frac{\partial u}{\partial x} + v\frac{\partial u}{\partial y} + w\frac{\partial u}{\partial z} = -\frac{1}{\rho}\frac{\partial P}{\partial x} + \frac{\partial}{\partial x}\left(\vartheta_{eff}\left(\frac{\partial u}{\partial x}\right)\right) + \frac{\partial}{\partial y}\left(\vartheta_{eff}\left(\frac{\partial u}{\partial y}\right)\right) + \frac{\partial}{\partial z}\left(\vartheta_{eff}\left(\frac{\partial u}{\partial z}\right)\right) \quad (1.13)$$

$$\frac{\partial v}{\partial t} + u\frac{\partial v}{\partial x} + v\frac{\partial v}{\partial y} + w\frac{\partial v}{\partial z} = -\frac{1}{\rho}\frac{\partial P}{\partial x} + \frac{\partial}{\partial x}\left(\vartheta_{eff}\left(\frac{\partial v}{\partial x}\right)\right) + \frac{\partial}{\partial y}\left(\vartheta_{eff}\left(\frac{\partial v}{\partial y}\right)\right) + \frac{\partial}{\partial z}\left(\vartheta_{eff}\left(\frac{\partial v}{\partial z}\right)\right) - g\frac{(\rho - \rho_0)}{\rho} \quad (1.14)$$

$$\frac{\partial w}{\partial t} + u\frac{\partial w}{\partial x} + v\frac{\partial w}{\partial y} + w\frac{\partial w}{\partial z} = -\frac{1}{\rho}\frac{\partial P}{\partial x} + \frac{\partial}{\partial x}\left(\vartheta_{eff}\left(\frac{\partial w}{\partial x}\right)\right) + \frac{\partial}{\partial y}\left(\vartheta_{eff}\left(\frac{\partial w}{\partial y}\right)\right) + \frac{\partial}{\partial z}\left(\vartheta_{eff}\left(\frac{\partial w}{\partial z}\right)\right) \quad (1.15)$$

where u, v, and w are the mean velocity components in the x, y, and z directions, respectively, t is the time, P is the fluid pressure, $\upsilon_{eff}$ represents the effective kinematic viscosity ($\upsilon_{eff}=\upsilon_t+\upsilon$), $\upsilon_t$ is the turbulent kinematic viscosity, g is the gravity acceleration, ρ is the fluid density, and $\rho_0$ is the reference fluid density.

The Concentration/Temperature Equation

The Advection-Diffusion equation is solved for both transport of concentration and temperature as follows:

$$\frac{\partial \mathrm{T}}{\partial t} + u\frac{\partial \mathrm{T}}{\partial x} + v\frac{\partial \mathrm{T}}{\partial y} + w\frac{\partial \mathrm{T}}{\partial z} = k_{eff}\left(\frac{\partial^2 T}{\partial x^2} + \frac{\partial^2 T}{\partial y^2} + \frac{\partial^2 T}{\partial z^2}\right) \quad (1.16)$$

$$k_{eff} = \frac{\vartheta_t}{Pr_t} + \frac{\vartheta}{Pr} \quad (1.17)$$

where T is the fluid temperature, $k_{eff}$ is the heat transfer coefficient, Pr is the Prandtl number, and $Pr_t$ is the turbulent Prandtl number.

Concentration transport equation is written as:

$$\frac{\partial C}{\partial t} + u\,\frac{\partial C}{\partial x} + v\,\frac{\partial C}{\partial y} + w\,\frac{\partial C}{\partial z} = D\left(\frac{\partial^2 C}{\partial x^2} + \frac{\partial^2 C}{\partial y^2} + \frac{\partial^2 C}{\partial z^2}\right) \tag{1.17}$$

where C is the fluid concentration (salinity, S), and D is the isotropic diffusion coefficient.
The next step is choosing a suitable discretization method, which is approximating the set of differential equations by a system of algebraic equations for the variables at a number of discrete points in space and time. The most important discretization methods are: the Finite Difference Method (FDM), the Finite Volume Method (FVM), and the Finite Element Method (FEM).
As mentioned, the subject of submerged negatively buoyant discharges has received a great deal of attention over the past few decades, and experimental studies have been actively followed in this field. However, numerical studies have rarely been done for inclined dense jets and therefore need further pursuit.
Vafeiadou et al. (2005) employed a 3-D numerical model named CFX-5 to simulate the hydrodynamic and mixing characteristics of negatively buoyant jets issuing upwards at various angles, and reproducing experiments done by Roberts et al. (1997), a grid refinement was used near the nozzle and the bottom of the tank, as well as a shear stress transport turbulence closure scheme. The numerical results were in agreement with the laboratory experiments, as they both showed that the initial terminal rise height increased with increasing Froude numbers. However, their numerical model seems to slightly underestimate the rise height and considerably underestimate the distance to the impact point as observed by Roberts et al. (1997). Elhaggag et al. (2011) conducted both experimental and numerical investigations of dense brine jets for disposal areas of limited extent, performing a number of numerical simulations using the Fluent CFD package and comparing the results with experimental measurements. They tried various diameters of ports and concertation of effluent salinities in stagnant water, and the numerical model showed good performance in terms of terminal rise height and concentration profile.
Gildeh et al. (2014), performed a numerical study on the near-field flow and mixing characteristics of thermal and saline wall jets released from submerged outfall into stagnant ambient water, and also compared the performance of different Reynolds-averaged Navier-Stokes (RANS) turbulence models, and the results were compared to both available experimental and numerical data. It was found that two models perform best among the seven models chosen in this paper.

Alfaifi et al. (2018) evaluated the effect of receiving water conditions on offset buoyant jet behavior both experimentally and numerically, performing several experiments on the discharge of thermal and nonthermal horizontal buoyant offset jets into stagnant ambient water. The experimental results were then compared to the predictions of three Reynolds-averaged Navier-Stokes (RANS) turbulence models. Out of these models, the best prediction of the centerline jet trajectory was found to be obtained from the realizable k-ε model.

Since to the best knowledge of the authors, the effects of waves on INBJs have never been numerically investigated, this study presents the results of the numerical modelling of the effects of waves on inclined dense jets. Negatively buoyant jets with an angle of 45° have been studied using the open-source CFD code OpenFOAM (OPEN Field Operation and Manipulation) (OpenFOAM user and programmer guides, 2011), which is based on FVM and has been modified to incorporate the effects of buoyancy and salinity transport. Four turbulence models, including the RNG k-ε, realizable k-ε, nonlinear k-ε, and LRR models, have been tested. The wave characteristics were chosen as similar to the experimental study in Part Three. The results are then compared with the experimental measured values, and the formulae obtained in the previous section have been verified.

### 1.3.Novelty and Contributions of the Study:

Several novel elements are proposed and investigated in this study:

- The solution for variable density shallow water equations is applied to a triangular grid element mesh, and a new discretization of the source terms for a well-balanced property is proposed. The proposed central upwind scheme preserves the positivity of the flow in depth and density. A Eulerian approach, which is computationally less expensive than the interface-tracking technique, was employed in this study. The accuracy of the suggested method and its different properties were demonstrated for a number of well-known benchmark test cases. The proposed scheme is the first well balanced, positivity-preserving scheme on a triangular mesh in the literature in the context of variable density flows.

- A numerical simulation of the mixing processes in two-layer flows occurring over an isolated dune was carried out. The Large Eddy Simulation (LES) approach was employed

to obtain accurate results for the mixing behavior and reproduce the interfacial fluctuations. The results of the numerical model were compared and validated with the results of experiments performed by the author at the University of A Coruña, Spain using PIV-LIF techniques. A numerical RANS simulation was also done and included for comparison in order to demonstrate the superiority of LES.

- The interaction between wave motion and an inclined negatively buoyant jet has been investigated through a series of physical experiments. The experiments were performed in a stagnant environment as well as in wave-current environments, and the results of these tests were compared. A combination of the Particle Image Velocimetry (PIV) technique and the full-field Laser Induced Fluorescence (LIF) technique was employed to reveal the structure of the mixing patterns and their statistical properties, and to also derive the instantaneous velocity vector map. Empirical formulas for predicting jet terminal rise height, jet centerline trajectory, the minimum dilution at centerline peak and return point, are proposed for wave-only and wave-current conditions. These can be used in environmental impact assessment studies of outfalls in industry and to optimize the location and configuration of marine outfalls.
- The interaction between wave motion and an inclined negatively buoyant jet has been numerically investigated. Four turbulence models including RNG $k$-$\varepsilon$, realizable $k$-$\varepsilon$; Nonlinear $k$-$\varepsilon$; and LRR have been tested. The performance of each turbulence model is investigated in revealing mixing behaviour and different statistical properties. The results are then compared to the measured values in experimental study and empirical formulas obtained from experiments are verified.

### 1.4.Thesis Outline

The thesis is organized as a sequence of technical papers, and as such it is divided into five chapters. An extension of a well-balanced central upwind scheme for variable density shallow water flow equations on triangular grids is presented in detail in Chapter 2. This chapter includes an extensive literature review and describes the application of the numerical model, as well as the governing equations and discretizations of the source terms required to reach the well-balanced property. To validate the different aspects of the proposed solution, numerical examples are also provided. This chapter was published in the Computers and Fluids Journal, 156 (2017) 4 41–4 48,

and also published and presented at the International Symposium on Outfall Systems (ISOS), Organized by the IAHR-IWA Joint Committee on Marine Outfall Systems, 2016.

The large eddy simulations of two-layer exchange flows over a bottom sill are presented in Chapter 3. An introduction to the LES approach and the mesh-generating method is summarized in the beginning of this chapter, followed by a detailed description of the experimental setup and the PIV-LIF data processing techniques. A RANS numerical simulation has also been done to prove the necessity of using LES to reproduce the KH instabilities.

The results of the numerical simulation, including the mean velocity and density profiles, interfacial instabilities, Bulk Richardson number, and entrainment rate, are presented in Chapter 3 and the data from the experimental study are included for comparison. This chapter is submitted to the Journal of Marine Science and Technology.

The results of the laboratory experiments on the interactions of a negatively buoyant jet with regular waves using the PIV-LIF technique are presented in Chapter 4. An extensive literature review, the complete experimental plan, and the device calibration are described in this chapter. The results of this chapter have been submitted to the Canadian Journal of Civil Engineering (cjce-2018-0606). The results were also presented at the 8th International Symposium on Environmental Hydraulics (ISEH, 2018). Moreover, a comparison between numerical and experimental results are submitted to the IAHR World Congress, 2019.

The results of the numerical simulations of the experiments conducted in Chapter 4 are presented in Chapter 5. An extensive literature review, boundary conditions and computational setup for different turbulence models are described in this chapter. The results of the numerical simulations, including jet trajectory, terminal rise height, minimum dilution at centreline peak and return point, as well as cross-sectional velocity profiles for each turbulence model are presented in Chapter 5. A comparison between numerical and experimental results are included to show the performance of each model. The results of this chapter have been submitted to the Environmental Fluid Mechanics.

Lastly, Chapter 6 presents the conclusions from the different chapters and suggestions for future studies.

# 2. Extension of a Well-balanced Central Upwind Scheme for Variable Density Shallow Water Flow Equations on Triangular Grids [1]


## Abstract

In this paper, the central upwind scheme with triangular discretization of the domain is extended and applied to variable density shallow water system of equations. In this scheme, the well-balanced and positivity preserving properties are maintained such that the large oscillations and noises are avoided in the solution. Furthermore, time-history of flow surface always remains non-negative throughout the simulations. Various properties of the scheme are validated using several benchmark data. Also, the accuracy and efficiency of the methodology are tested by comparing the results of the model to other complex scheme for some test cases. The method ensures high computational efficiency while maintaining the accuracy of the results and preserves two types of "lake at rest" steady states, and is oscillation free across the small density change.



*Keywords*: shallow water equations; variable density; well-balanced central upwind scheme; two-dimensional depth-averaged model


## 2.1. Introduction and literature review

Environmental free surface shallow water flow has numerous applications for the transport debris and suspended sediment especially under slope conditions. When such flows enter larger rivers or other types of water bodies such as lakes, the significant difference between the densities of the two systems need to be accounted for in order to ensure accurate simulation results. As such, domestic and industrial effluents from outfall structures often have a different density than that of the ambient water body, something which leads to various flow and mixing characteristics of the discharge. An example of industrial effluent is the Ras Laffan Industrial City (RLIC) outfall in Qatar, with a coastline of 563 km length. Most of its required water is supplied from desalination


[1] This chapter has been published as Sepideh Khorshid, Abdolmajid Mohammadian, Ioan Nistor "Extension of a well-balanced central upwind scheme for variable density shallow water flow equations on triangular grids", **Computers and Fluids** Journal, 156 (2017) 441–448. http://dx.doi.org/10.1016/j.compfluid.2017.08.005

plants (Darwish and Mohtar 2013), so the pollution of water which arises from these industrial activities has always been a concern for Qatar environmental authorities.

To model the mixing of the two interacting water bodies, three-dimensional models such as OpenFOAM, Delft3D and MIKE-3 have been increasingly used. However, due to their high computational costs, if scientifically justifiable, it is more efficient to use two-dimensional depth-averaged models because of their simplicity in implementation and application, especially in the initial stages of the design (Hsieh and Yang, 2003). Therefore, in many cases if the ambient stream can be approximated to a shallow stream, the use of shallow water equations can lead to some of the most performant tools in modeling mixing problems. To use the traditional shallow water equations in modeling mixing, it is necessary to further modify them such as to include the option of density change, which has been the focus of many previous researches using shallow water equations.

Shallow-water equations describe a thin layer of fluid in which vertical dimension is much smaller than the typical horizontal scale and it has two major general characteristics. Firstly, they closely follow the earth surface, so they are subjected to negligible acceleration in vertical direction, so conservation of mass implies that the vertical velocity of the fluid is very small (Falconer,1993). Secondly, it can be shown from the momentum equation that vertical pressure gradient is approximately hydrostatic. Assuming hydrostatic distribution of pressure allows a considerable simplification in mathematical solution of these equations.

However, shallow-water equations are not exactly two-dimensional. Flow must have three-dimensional structure due to the existence of bottom friction and density stratification. (Vreugdenhil, 1994). But, for many practical applications, these three-dimensional effects can be neglected and using a 2-d depth-averaged form is sufficient and gives the same information at lower cost. Two-dimensional calculations require considerably less computer resources.

Shallow water flows have been widely studied. The early version of SWE has been derived by Boussinesq (1887) and Lamb (1932). The numerous examples illustrate how wide the application of numerical solver of the SWE is, including tidal flows (Hendershott, 1981), tidal mixing (Ridderinkhof et al., 1990), storm surges (Dube et al., 1985), river flows (Ogink, 1986), dam break waves (Alcrudo and García-Navarro, 1993), coastal flows (Wind and Vreugdenhil, 1986), lake

flows (Platzman, 1972), wave propagation (LeVeque, 1997), flows over variable topography (George, 2008) and internal flows (Garvine, 1987).

Abbott (1979) and Weiyan (1992) discussed numerical aspect of the shallow water type equations and provided a systematic account of the principles of computational hydraulics and their application to free surface flows. Those studies did not consider the cases with abrupt change in underwater topography, and the possibility of mixing of flows with different densities. Sleight et al. (1998) refined the method to be able to handle complex flow domains focusing only on the conservative form of the shallow water equations.

According to Toro (2001) despite making simplifying assumption in driving non-linear shallow water theory, computation of numerical solution of the equations remains a challenging task. The main challenge is due to this fact that the inviscid shallow water equations admit solutions that include discontinuities such as shocks, contact discontinuities, also other discontinuous waves such as vortices and shear waves. Shock waves are discontinuous solutions of hyperbolic conservation laws which obey some mathematical conditions. A lot of efforts have been made to compute shock waves correctly, because a numerical misrepresentation can significantly affect the simulation and lead to meaningless numerical results. It is recognised that to propagate a shock at correct speed, conservative numerical method must be used (Lax and Wendroff, 1960). Shock-capturing is one of the approaches to compute the solutions containing discontinuities, in which, a single numerical scheme is used for the complete domain, so shock waves and other discontinuities emerge as part of the complete solution. Toro (1999) classifies shock capturing scheme into classical symmetrical methods and high resolution upwind (modern) methods. In the presence of shock waves in both schemes, a certain amount of numerical dissipation is required to avoid the numerical oscillations.

Classical symmetrical methods including the MacCormack (1969) method and Lax–Wendroff method (1960), do not consider any information about the wave propagation in the discretization. Moreover, the numerical dissipation terms are usually linear, therefore, it can only provide accurate results in the case of smooth and weak-shock solutions, however, the problem with this scheme is that when strong shock waves are present in the solutions, oscillations can arise near the discontinuities.

On the other hand, Upwind (modern) schemes try to discretize hyperbolic partial differential equations by using differencing biased in the direction determined by the sign of the characteristic speeds. Using nonlinear numerical dissipation, this scheme adjusts the amount of dissipation in any cell of the mesh, in accordance with the gradients in the solution. Therefore, the ability of the scheme for simulating the problems containing strong shock waves is proven (Cockburn and Shu, 1994).

Higher order Total Variation Diminishing (TVD) schemes proposed by Harten (1983), Flux-Corrected Transport scheme by Boris and Book (1976), Monotonic Upstream-centered Schemes for Conservation Laws (MUSCL) based on the Godunov approach by Van Leer (1979) are the examples of modern shock-capturing schemes. Shock-capturing method of the Gondunov type can resolve strong shear waves, bores, and contact discontinuities. Van leer (1979) extended the Godunov method to second order accuracy. His works brought this fact back that although the first-order methods are too inaccurate, however, all scheme of accuracy greater than one will produce unreal oscillations across discontinuities. The fundamental works of Harten (1983), Roe (1981) and Osher and Sethian (1988) have led to Total Diminishing Variation (TVD) upwind and central methods, which are oscillation-free near shock waves while remaining second-order accuracy in smooth parts of the flow (Toro,1999). In recent years, high-order accurate numerical schemes (with higher than second order accuracy), have attracted attentions with the aim of minimizing computational time (Xing and Shu, 2014).

As mentioned before, to use the traditional shallow water equations in modeling mixing, it is necessary to further modify them such as to include the option of density change. For simplicity, many researchers treated debris flows as motion of a continuum and used different rheological models to be able to use the constant density equations (Jin and Fread, 1997; Laigle and Coussot, 1997; O'Brien et al. 1993).

Brice et al. (2010) treated dissolved salt in water as a variable in the momentum conservation by applying the Boussinesq approximation to preserve the density effects in the hydrostatic pressure term. The suggested formulation allowed a robust simulation of the horizontal flow dynamics; while preserving the efficiency of a characteristic method.

Solving the shallow water system is a challenging task, which needs a robust numerical method. The method should be well-balanced (Bermundez and Vazquez, 1994), which means that it should

exactly preserve the steady-state solutions. If the method does not accurately respect the balance, the numerical method may lead to significant oscillations, even overshadowing the main stream (Bryson et al. 2010, Chertock et al. 2015). This has been the focus of several studies (e.g. Audusse et al., 2004; Perthame and Simeoni, 2001; Canesttrelli et al. 2010; Noelle et al. 2006; Russo and Khe, 2009; Liang and Marche 2009; Bryson et al., 2010; Bollermann et al., 2013, Shirkhani et al., 2016). Moreover, the numerical method should be positivity preserving, which means that in order to evaluate the eigenvalues of the system, the water level above the bed should remain positive at all times. This property is crucial where in parts of the analytical domain no water is present, or when the depth of water is very small, and small oscillations may lead to negative depths, eventually resulting in the simulation to fail. This major property has been studied in various studies (Bryson et al. 2011; Kurganov and Petrova, 2007; Perthame and Simeoni, 2001; Bollermann et al. 2013; Gallardo et al. 2007; Xing et al. 2010). Chertock et al. (2014) modified the Saint-Venant system of shallow water equations considering the water temperature fluctuations. This scheme is also well-balanced and positivity preserving, and does not develop false pressure oscillations near temperature gradients.

In this study, the central upwind scheme developed in Bryson et al. (2010) is applied and extended to the variable density shallow water equations following the work of Brice et al. (2010). Due to the use of the Bousinesq approximation in the formulation suggested by Brice et al. (2010), it is assumed that the density gradients are small. Therefore, the methodology used here is more efficient compared to the similar works by other investigators, when the concentration of the sediment in suspension is not very high. This scheme considers the well-balanced and positivity-preserving characteristics of the dense flows. In this regard, the analytical solution is presented over a triangular discretization of the domain, using a higher order temporal and spatial numerical scheme which is discussed in detail.

Following this introduction, section 2 of the paper describes the application of the numerical model, as well as discretization of the source terms required to reach the well-balanced property. Numerical examples are further presented in Section 3 in order to validate different aspects of the proposed solution. Some concluding remarks complete this study.

## 2.2. Governing Equations

In the current study, the two-dimensional (2D) Saint-Venant system of shallow water equations as presented below are used.

$$\boldsymbol{U}_t + [\boldsymbol{F}(U)]_x + [\boldsymbol{G}(\boldsymbol{U})]_y = \boldsymbol{S}(\boldsymbol{U}) \tag{2.1}$$

in which, vectors $\boldsymbol{U}$, $\boldsymbol{F}$, $\boldsymbol{G}$, and $\boldsymbol{H}$ are defined as

$$\boldsymbol{U} = \begin{pmatrix} h \\ uh \\ vh \\ \rho h \end{pmatrix}, \quad \boldsymbol{F}(\boldsymbol{U}) = \begin{pmatrix} uh \\ u^2h + \frac{g}{2\rho_0}\rho h^2 \\ uvh \\ \rho uh \end{pmatrix}, \quad \boldsymbol{G}(\boldsymbol{U}) = \begin{pmatrix} vh \\ uvh \\ v^2h + \frac{g}{2\rho_0}\rho h^2 \\ \rho vh \end{pmatrix},$$

$$\boldsymbol{S}(\boldsymbol{U}) = \begin{pmatrix} 0 \\ -\rho g h B_x - \tau_{b,x} \\ -\rho g h B_y - \tau_{b,y} \\ 0 \end{pmatrix} \tag{2.2}$$

where, $h$ is the water depth above the bed elevation $B$, $u$ a

nd $v$ are the depth-averaged velocities in x- and y-direction, respectively, $\rho$ is the average density of the fluid, $g$ is the acceleration of gravity, $\rho_0$ is the reference freshwater density and $\tau_{b,x}$ and $\tau_{b,y}$ are the bed shear stress values in x- and y- direction, respectively. Indices of *x*, *y*, and *t* represent the first derivatives of the parameters with respect to the spatial 2D and time coordinates, respectively.

One of the objectives of this study is to extend the well-balanced property for the variable density shallow water equations. Therefore, one can first rewrite the system in an equivalent form in terms of $\omega \coloneqq h + B, q \coloneqq uh, p \coloneqq vh, r \coloneqq \rho h$ and neglecting the effects of the bottom friction terms $(\tau_{bx}, \tau_{by})$ as

$$\omega_t + q_x + p_y = 0$$

$$q_t + \left[\frac{q^2}{\omega - B} + \frac{gr}{2\rho_0}(\omega - B)\right]_x + \left[\frac{pq}{(\omega - B)}\right]_y = -rgB_x/\rho_0$$

$$p_t + \left[\frac{pq}{(\omega - B)}\right]_x + \left[\frac{p^2}{\omega - B} + \frac{gr}{2\rho_0}(\omega - B)\right]_y = -rgB_y/\rho_0$$

$$r_t + \left[\frac{rq}{(\omega - B)}\right]_x + \left[\frac{rp}{(\omega - B)}\right]_y = 0 \tag{2.3}$$

Kurganov and Petrova (2005) introduced a new central-upwind scheme on general triangular grids to solve the two-dimensional conservation laws. Unlike Godunov-type schemes, this can be applied to complex geometries while maintaining its simplicity and robustness. In the present study, the triangular domain of $\tau := \bigcup_j T_j$ ($T_j$ being the triangular cells of size $|T_j|$) is used. This discretization of this domain is shown in Figure. 2.1, where $\vec{n}_{jk} := (\cos(\theta_{jk}), \sin(\theta_{jk}))$ is the outer unit vector, normal to the corresponding sides of $T_j$ with the length $l_{jk}$ ($k$ = 1,2,3). $x_j$,and $y_j$ represent the coordinates of the mass center of $T_j$, while $M_{jk}$ = $(x_{jk},y_{jk})$ is the midpoint of the $k$-th side of the $T_j$ triangle. In this study, the authors applied the central upwind scheme proposed by Kurganov and Petrova to variable density shallow water equations written as

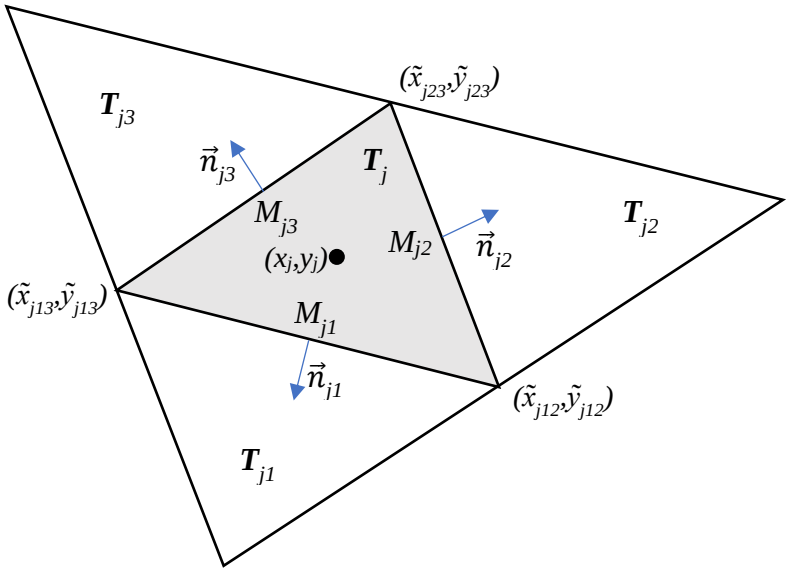


Figure 2-1 Triangular cell used in the proposed model

$$\frac{d\bar{\boldsymbol{U}}_j}{dt} = -\frac{1}{|T_j|}\sum_{k=1}^{3}\frac{l_{jk}\cos(\theta_{jk})}{a_{jk}^{in}+a_{jk}^{out}}\left[a_{jk}^{in}\boldsymbol{F}\left(\boldsymbol{U}_{jk}(M_{jk}),\boldsymbol{B}(M_{jk})\right)+a_{jk}^{out}\mathbf{F}\left(\mathbf{U}_j(M_{jk}),\mathbf{B}(M_{jk})\right)\right]$$
$$-\frac{1}{|T_j|}\sum_{K=1}^{3}\frac{l_{jk}\sin(\theta_{jk})}{a_{jk}^{in}+a_{jk}^{out}}\left[a_{jk}^{in}\boldsymbol{G}\left(\boldsymbol{U}_{jk}(M_{jk}),\boldsymbol{B}(M_{jk})\right)\right.$$
$$\left.+a_{jk}^{out}\boldsymbol{G}\left(\boldsymbol{U}_j(M_{jk}),\boldsymbol{B}(M_{jk})\right)\right]+$$
$$\frac{1}{|T_j|}\sum_{K=1}^{3}l_{jk}\frac{a_{jk}^{in}a_{jk}^{out}}{a_{jk}^{in}+a_{jk}^{out}}\left[\boldsymbol{U}_{jk}(M_{jk})-\boldsymbol{U}_j(M_{jk})\right]+\bar{\boldsymbol{S}}_j \qquad (2.4)$$

where, $\boldsymbol{U}_j(M_{jk})$ and $\boldsymbol{U}_{jk}(M_{jk})$ are the vectors at $M_{jk}$ of the piecewise linear reconstruction of $\boldsymbol{U}$ at time *t* defined as:

$$\widetilde{\boldsymbol{U}}(x,y) := \overline{\boldsymbol{U}}_j + (\boldsymbol{U}_x)_j(x-x_j) + (\boldsymbol{U}_y)_j(y-y_j), \qquad (x,y) \in T_j \tag{2.5}$$

$$\begin{aligned} \boldsymbol{U}_j(M_{jk}) &:= \lim_{(x,y)\to M_{jk};(x,y)\in T_j} \widetilde{\boldsymbol{U}}(x,y) \\ \boldsymbol{U}_{jk}(M_{jk}) &:= \lim_{(x,y)\to M_{jk};(x,y)\in T_{jk}} \widetilde{\boldsymbol{U}}(x,y) \end{aligned} \tag{2.6}$$

Also, $\overline{\boldsymbol{U}}_j$ is the cell-averaged value of the solution vector. The directional local speeds ${a_{jk}}^{in}$in and ${a_{jk}}^{out}$ are defined by:

$$\begin{aligned} {a_{jk}}^{\text{in}}(M_{jk}) &= -\min\{\lambda_1[V_{jk}(\boldsymbol{U}_j(M_{jk}))], \lambda_1[V_{jk}(\boldsymbol{U}_{jk}(M_{jk}))], 0\} \\ {a_{jk}}^{\text{out}}(M_{jk}) &= \max\{\lambda_3[V_{jk}(\boldsymbol{U}_j(M_{jk}))], \lambda_3[V_{jk}(\boldsymbol{U}_{jk}(M_{jk}))], 0\} \end{aligned} \tag{2.7}$$

where, $\lambda_1[V_{jk}] \le \lambda_2[V_{jk}] \le \lambda_3[V_{jk}]$ are the eigenvalues of the matrix of matrix $V_{jk}$ which is defined as $V_{jk} = \cos(\theta_{jk})\frac{\partial \boldsymbol{F}}{\partial \boldsymbol{U}} + \sin(\theta_{jk})\frac{\partial \boldsymbol{G}}{\partial \boldsymbol{U}}$.

In this study, a strong stability preserving (SSP) Runge–Kutta (RK) time discretization method is used because of its increased stability and higher temporal accuracy. The most commonly used SSP RK method, which is employed in this study, is the third order accurate SSP RK (3,3), widely known as the Shu–Osher method (Shu, 1988).

In addition, to decrease the oscillations caused by probable phase errors, a third-order spatial discretization with slope limiter function is also applied in the solution. In this regard, the methodology suggested by Jawahar and Kamath (2000) is implemented. In order to find the numerical derivatives $(\widehat{U}_x)_i$ and $(\widehat{U}_y)_i$ in each cell, first the non-limited gradients, $(\nabla \boldsymbol{U})_j$ are computed by finding the x- and y-derivatives of the planes passing through the points $(x_{j1}, y_{j1}, \boldsymbol{U}_{j1})$, $(x_{j2}, y_{j2}, \boldsymbol{U}_{j2})$ and $(x_{j3}, y_{j3}, \boldsymbol{U}_{j3})$ as shown in Figure 2.2.

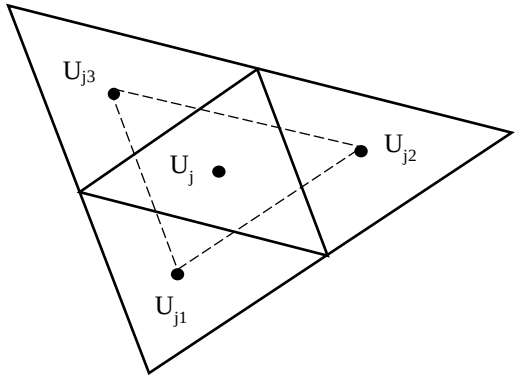


Figure 2-2 Scheme used for calculating non-limited derivatives

The derivatives are calculated as:

$$(U_x)_j = \frac{(y_{j3}-y_{j1})(U_{j2}-U_{j1})-(y_{j2}-y_{j1})(U_{j3}-U_{j1})}{(y_{j3}-y_{j1})(x_{j2}-x_{j1})-(y_{j2}-y_{j1})(x_{j3}-x_{j1})}$$
$$(U_y)_j = \frac{(x_{j2}-x_{j1})(U_{j3}-U_{j1})-(x_{j3}-x_{j1})(U_{j2}-U_{j1})}{(x_{j2}-x_{j1})(y_{j3}-y_{j1})-(x_{j3}-x_{j1})(y_{j2}-y_{j1})} \quad (2.8)$$

Then, following the approach suggested by Pan and Cheng (1993), the limited numerical gradient $(\nabla \boldsymbol{U}_b)_i$ can be obtained from the weighted average of three non-limited gradients as follows.

$$(\nabla \widehat{U})_i = \Delta_{i1}(\nabla \widehat{U})_{i1} + \Delta_{i2}(\nabla \widehat{U})_{i2} + \Delta_{i3}(\nabla \widehat{U})_{i3} \quad (2.9)$$

where, $\Delta_{i1}$, $\Delta_{i2}$ and $\Delta_{i3}$ are the weights, and $(\nabla \boldsymbol{U})_{i1}$, $(\nabla \boldsymbol{U})_{i2}$ and $(\nabla \boldsymbol{U})_{i3}$ are the three non-limited gradients defined by Fraccarollo and Armanini (1998), for $j = i_1$, $i_2$ and $i_3$, respectively. The weights can be calculated as:

$$\Delta_{i1} = \frac{\|(\nabla U)_{i2}\|^2 \|(\nabla U)_{i3}\|^2 + \varepsilon}{\|(\nabla U)_{i1}\|^4 + \|(\nabla U)_{i2}\|^4 + \|(\nabla U)_{i3}\|^4 + 3\varepsilon}$$
$$\Delta_{i2} = \frac{\|(\nabla U)_{i1}\|^2 \|(\nabla U)_{i3}\|^2 + \varepsilon}{\|(\nabla U)_{i1}\|^4 + \|(\nabla U)_{i2}\|^4 + \|(\nabla U)_{i3}\|^4 + 3\varepsilon}$$
$$\Delta_{i3} = \frac{\|(\nabla U)_{i1}\|^2 \|(\nabla U)_{i2}\|^2 + \varepsilon}{\|(\nabla U)_{i1}\|^4 + \|(\nabla U)_{i2}\|^4 + \|(\nabla U)_{i3}\|^4 + 3\varepsilon} \quad (2.10)$$

where, the parameter $\varepsilon$ is an infinitesimal positive number, i.e. $10^{-20}$, assumed, so that division by zero is prevented.

### 2.2.1. Well-Balanced Discretization of the source term

In order to maintain the well-balance property of the solution, it is necessary for the source term to balance the numerical fluxes exactly, such that the right-hand side of Equation (2.4) becomes

zero, when experiencing the so-called "lake at rest" situation ($h + B = \text{const.}, u \equiv v \equiv 0, \rho \equiv \text{const.}$). Therefore, the source term should satisfy the following two conditions:

$$-\frac{g}{|T_j|}\sum_{K=1}^{3} l_{jk}\cos(\theta_{jk})\frac{\left(C - B(M_{jk})\right)\ r_{jk}}{2\rho_0} + \overline{\boldsymbol{S}}_j^{(2)} = 0$$

$$-\frac{g}{|T_j|}\sum_{K=1}^{3} l_{jk}\sin(\theta_{jk})\frac{\left(C - B(M_{jk})\right)\ r_{jk}}{2\rho_0} + \overline{\boldsymbol{S}}_j^{(3)} = 0 \qquad (2.11)$$

where, $\overline{\boldsymbol{S}}_j = (0, \overline{\boldsymbol{S}}_j^{(2)}, \overline{\boldsymbol{S}}_j^{(3)})$, and

$$\overline{\boldsymbol{S}}_j^{(2)} \approx -\frac{g}{|T_j|\rho_0}\int_{T_j} r(x,y)\, B_x(x,y)\ dx\, dy$$

$$\overline{\boldsymbol{S}}_j^{(3)} \approx -\frac{g}{|T_j|\rho_0}\int_{T_j} r(x,y)\, B_y(x,y)\, dx\, dy \qquad (2.12)$$

To derive the desired well-balanced quadrature for the integrals in (2.12), we first apply the Green's formula ($\int_{T_j} \text{div}\,\vec{\mathrm{G}}\, dx\, dy = \int_{\partial T_j} \vec{\mathrm{G}}.\vec{n}\, ds$) to the vector field $\vec{\mathrm{G}} = \left[r(x,y)\left(\omega(x,y) - B(x,y)\right), 0\right]$, and obtain:

$$\int_{T_j} (\omega(x,y) - B(x,y))\, r_x(x,y)\, dx\, dy$$

$$-\int_{T_j} B_x(x,y)\, r(x,y)\, dx\, dy + \int_{T_j} \omega_x(x,y)\, r(x,y)\, dx\, dy$$

$$= \sum_{\mathrm{K}=1}^{3} \int_{\partial T_j} r(x,y)\left(\omega(x,y) - B(x,y)\right) cos(\theta_{jk})\ ds \qquad (2.13)$$

Considering the definition $r(x,y) := \rho(x,y)h(x,y)$,

$$r_x(x,y) := \rho_x(x,y)h(x,y) + \rho(x,y)h_x(x,y) \qquad (2.14)$$

Substituting the above equation in (15) leads to:

$$-\int_{T_j} B_x(x,y)\, r(x,y)\, dx\, dy$$

$$= \sum_{K=1}^{3} \int_{\partial T_j} r(x,y)\big(\omega(x,y) - B(x,y)\big)\, cos\big(\theta_{jk}\big)\; ds$$

$$-\int_{T_j} \big(\omega(x,y) - B(x,y)\big)[\rho_x(x,y)h(x,y) + \rho(x,y)h_x(x,y)]\; dx\, dy$$

$$-\int_{T_j} \omega_x(x,y)\, r(x,y)\, dx\, dy \qquad (2.15)$$

Note that $h(x,y) = \big(\omega(x,y) - B(x,y)\big)$, therefore, $h_x(x,y) = \big(\omega_x(x,y) - B_x(x,y)\big)$ is substituted in (2.15) as follows:

$$-\int_{T_j} B_x(x,y)\, r(x,y)\, dx\, dy$$

$$= \sum_{\mathrm{K}=1}^{3} \int_{\partial T_j} r(x,y)\big(\omega(x,y) - B(x,y)\big)\, cos\big(\theta_{jk}\big)\; ds$$

$$-\int_{T_j} \big(\omega(x,y) - B(x,y)\big)\big[\rho_x(x,y)\big(\omega(x,y) - B(x,y)\big)$$

$$+ \rho(x,y)\big(\omega_x(x,y) - B_x(x,y)\big)\big]\; dx\, dy$$

$$-\int_{T_j} \omega_x(x,y)\, r(x,y)\, dx\, dy \qquad (2.16)$$

Expanding the equations and noting that $r(x,y) = \rho(x,y)\big(\omega(x,y) - B(x,y)\big)$, one obtains:

$$-\int_{T_j} B_x(x,y)\, r(x,y)\, dx\, dy$$

$$= \sum_{\mathrm{K}=1}^{3} \int_{\partial T_j} r(x,y)\big(\omega(x,y) - B(x,y)\big)\, cos\big(\theta_{jk}\big)\; ds$$

$$- \rho_x(x,y)\big(\omega(x,y) - B(x,y)\big)^2 - \int_{T_j} \omega_x(x,y)\, r(x,y)\, dx\, dy$$

$$+ \int_{T_j} B_x(x,y)\, r(x,y)\, dx\, dy - \int_{T_j} \omega_x(x,y)\, r(x,y)\, dx\, dy \qquad (2.17)$$

Now, simplifying both sides of the equation leads to:

$$-2\int_{T_j} B_x(x,y)\, r(x,y)\, dx\, dy$$

$$= \sum_{K=1}^{3} \int_{\partial T_j} r(x,y)\big(\omega(x,y) - B(x,y)\big)\, cos\big(\theta_{jk}\big)\; ds$$

$$- \rho_x(x,y)\big(\omega(x,y) - B(x,y)\big)^2 - 2\int_{T_j} \omega_x(x,y)\, r(x,y)\, dx\, dy \qquad (2.18)$$

After applying the midpoint rule to the equation (2.18), and replacing B with its continuous piecewise linear interpolant, the following equation can be derived.

$$-\frac{g}{|T_j|\rho_0}\int_{T_j} r\, B_x\; dx\, dy$$

$$\approx \frac{g}{2|T_j|\rho_0}\sum_{K=1}^{3} l_{jk}\; cos\big(\theta_{jk}\big)\frac{\big[(\rho h)_{jk}(M_{jk}) + (\rho h)_j(M_{jk}))\big]}{2}(\omega_j\big(M_{jk}\big) - B_{jk})$$

$$-\frac{g}{\rho_0}\bar{r}_j\omega_x - \frac{g}{2}\frac{\rho_x}{\rho_0}\left(\bar{\omega}_j - \bar{B}_j\right)^2 \qquad (2.19)$$

Likewise for the y momentum source term,

$$-\frac{g}{|T_j|\rho_0}\int_{T_j} r\,B_y\;dx\,dy$$

$$\approx \frac{g}{2|T_j|\rho_0}\sum_{\mathrm{K}=1}^{3} l_{jk}\sin(\theta_{jk})\frac{\left[(\rho h)_{jk}(M_{jk})+(\rho h)_j(M_{jk})\right]}{2}(\omega_j(M_{jk})-B_{jk})$$

$$-\frac{g}{\rho_0}\bar{r}_j\omega_y-\frac{g}{2}\frac{\rho_y}{\rho_0}\left(\bar{\omega}_j-\bar{B}_j\right)^2 \qquad (2.20)$$

Finally, the discretization of the source term can be expressed as

$$\bar{\boldsymbol{S}}_j^{(2)} \approx \frac{g}{2|T_j|\rho_0}\sum_{\mathrm{K}=1}^{3} l_{jk}\;cos(\theta_{jk})\frac{\left[(\rho h)_{jk}(M_{jk})+(\rho h)_j(M_{jk})\right]}{2}(\omega_j(M_{jk})-B_{jk})-\frac{g}{\rho_0}\bar{r}_j\omega_x$$

$$-\frac{g}{2}\frac{\rho_x}{\rho_0}\left(\bar{\omega}_j-\bar{B}_j\right)^2$$

$$\bar{\boldsymbol{S}}_j^{(3)} \approx \frac{g}{2|T_j|\rho_0}\sum_{K=1}^{3} l_{jk}\sin(\theta_{jk})\frac{\left[(\rho h)_{jk}(M_{jk})+(\rho h)_j(M_{jk})\right]}{2}(\omega_j(M_{jk})-B_{jk})-\frac{g}{\rho_0}\bar{r}_j\omega_y$$

$$-\frac{g}{2}\frac{\rho_y}{\rho_0}\left(\bar{\omega}_j-\bar{B}_j\right)^2 \qquad (2.21)$$

Replacing the new discretizations (2.21) in (2.4), since $\omega_x \equiv \omega_y \equiv 0$ for $\omega \equiv$ const., and $\rho_x \equiv \rho_y \equiv 0$ for $\rho \equiv$ const., the new discretizations in (2.21) satisfy (2.4) when $u \equiv v \equiv 0$. Therefore, $\frac{\mathrm{d}\bar{U}_\mathrm{j}}{\mathrm{d}t} = 0$, implying that the lake at rest remains unchanged and the system is well balanced.

### 2.2.2. Positivity preserving

In order to ensure the positivity of the stream depth, a reconstruction of the depth is required so that at all times $h_j(M_{jk}) \geq 0$. In this regard, in the cells that $\bar{\omega}_j < B_{jk}$ for at least one *k*, the cell-averaged $\bar{\omega}_j$ should be reconstructed ($\widetilde{\omega}$) such that it always exceeds the bed topography of the nodes $B_{jk}$ (*k*= 1, 2, 3). Herein, this is performed based on the methodology described by Bryson et al. (2010). After conducting this reconstruction in the necessary cells, the directional velocities and the density are calculated as in Chertock et al. (2013).

$$u=\frac{\sqrt{2}h(hu)}{\sqrt{h^4+\max(h^4,\varepsilon)}},\qquad v=\frac{\sqrt{2}h(hv)}{\sqrt{h^4+\max(h^4,\varepsilon)}},\qquad \rho=\frac{\sqrt{2}h(h\rho)}{\sqrt{h^4+\max(h^4,\varepsilon)}} \qquad (2.22)$$

where, $\varepsilon$ is the tolerance taken as $\max|T_j|^2$. The directional velocities and the density calculated above are then replaced into the fluxes as shown in Equation 23.

$$\boldsymbol{F}(\boldsymbol{U},B) \coloneqq \left(q, q.u + \frac{gr}{2\rho_0}(\omega - B), p.v, r.u\right)^{\mathrm{T}}$$
$$\boldsymbol{G}(\boldsymbol{U},B) \coloneqq \left(p, p.u, p.v + \frac{gr}{2\rho_0}(\omega - B), r.v\right)^{\mathrm{T}} \tag{2.23}$$

Finally, the local one-sided propagation speeds can be calculated as:

$$a_{jk}{}^{out}(M_{jk}) = \max\left\{u_j^{\theta}(M_{jk}) + \sqrt{\frac{gr_j(M_{jk})}{\rho_0}}, u_{jk}^{\theta}(M_{jk}) + \sqrt{\frac{gr_{jk}(M_{jk})}{\rho_0}}, 0\right\}$$
$$a_{jk}{}^{in}(M_{jk}) = -\min\left\{u_j^{\theta}(M_{jk}) - \sqrt{\frac{gr_j(M_{jk})}{\rho_0}}, u_{jk}^{\theta}(M_{jk}) - \sqrt{\frac{gr_{jk}(M_{jk})}{\rho_0}}, 0\right\} \tag{2.24}$$

where, $u_j^{\theta}(M_{jk})$ and $u_{jk}^{\theta}(M_{jk})$ are the normal velocities at $M_{jk}$, defined as

$$u_j^{\theta}(M_{jk}) \coloneqq \cos(\theta_{jk})\, u_j(M_{jk}) + \sin(\theta_{jk})\, v_j(M_{jk})$$
$$u_{jk}^{\theta}(M_{jk}) \coloneqq \cos(\theta_{jk})\, u_{jk}(M_{jk}) + \sin(\theta_{jk})\, v_{jk}(M_{jk}) \tag{2.25}$$

An important step is to show that the well-balanced central-upwind scheme also preserves the positivity of the water depth. The reader is referred to Bryson et al. (2010), where it is demonstrated that the following CFL-type condition guarantees positivity of the depth:

$$\Delta t < \frac{1}{6}\underbrace{\min}_{jk}\left[\frac{r_{jk}}{\max(a_{jk}^{in}, a_{jk}^{out})}\right] \tag{2.26}$$

Another desired property of the numerical model is that the positivity will be preserved for density ($\bar{\rho}_j^{n+1}$) as well. Based on the fact that $\bar{h}_j^{n+1} \geq 0$ is guaranteed by the corrected reconstruction, in order to prove that $\bar{\rho}_j^{n+1} \geq 0$, one only needs to ensure that $\overline{(h\rho)}_j^{n+1} \geq 0$. Using the forward Euler temporal discretization and writing the fourth component in equation (4) one obtains:

$$\overline{(h\rho)}_j^{n+1} = \overline{(h\rho)}_j^n - \frac{\Delta t}{|T_j|}\sum_{k=1}^{3}\frac{l_{jk}\cos(\theta_{jk})}{a_{jk}^{in}+a_{jk}^{out}}\left[a_{jk}^{in}(hu)_{jk}(M_{jk})\rho_{jk}(M_{jk}) + a_{jk}^{out}(hu)_j(M_{jk})\rho_j(M_{jk})\right]$$
$$-\frac{\Delta t}{|T_j|}\sum_{k=1}^{3}\frac{l_{jk}\sin(\theta_{jk})}{a_{jk}^{in}+a_{jk}^{out}}\left[a_{jk}^{in}(hv)_{jk}(M_{jk})\rho_{jk}(M_{jk}) + a_{jk}^{out}(hv)_j(M_{jk})\rho_j(M_{jk})\right]$$
$$+\frac{\Delta t}{|T_j|}\sum_{k=1}^{3} l_{jk}\frac{a_{jk}^{in}a_{jk}^{out}}{a_{jk}^{in}+a_{jk}^{out}}\left[h_{jk}(M_{jk})\rho_{jk}(M_{jk}) - h_j(M_{jk})\rho_j(M_{jk})\right] \qquad (2.27)$$

Based on the fact that $\overline{(h\rho)}_j^n = \frac{1}{3}\sum_{k=1}^{3}(h\rho)_j(M_{jk})$, the equation above can be reformulated to:

$$\overline{(h\rho)}_j^{n+1} = \frac{\Delta t}{|T_j|}\sum_{k=1}^{3} h_{jk}(M_{jk})\rho_{jk}(M_{jk})\frac{l_{jk}a_{jk}^{in}}{a_{jk}^{in}+a_{jk}^{out}}\left[a_{jk}^{out} - u_{jk}^{\theta}(M_{jk})\right]$$
$$+\sum_{k=1}^{3} h_{jk}(M_{jk})\rho_j(M_{jk})\left(\frac{1}{3} - \frac{\Delta t}{|T_j|}.\frac{l_{jk}a_{jk}^{out}}{a_{jk}^{in}+a_{jk}^{out}}\left[a_{jk}^{in} + u_j^{\theta}(M_{jk})\right]\right) \qquad (2.28)$$

The sum of the last two terms on the RHS of (2.28) needs to be nonnegative to guarantee that $\overline{(h\rho)}_j^{n+1} \geq 0$. This gives:

$$\Delta t < \frac{1}{6}\underbrace{\min}_{jk}\left[\frac{r_{jk}}{\max(a_{jk}^{in}, a_{jk}^{out})}\right] \qquad (2.29)$$

Finally, to guarantee the positivity preserving property of the numerical scheme while maintaining the numerical stability, Δt should satisfy the restrictions (2.26) and (2.29) for each time step. It should be noted that the theorem discussed above is valid when used in a high-order SSP solver, since the solver can be assumed as a combination of a number of forward Euler steps.

### 2.2.3. Calculation of derivatives

As shown in the equations presented before, throughout different parts of this method, spatial derivatives of different variables should be properly estimated in the triangular cell. Therefore, to calculate the derivatives of a scalar variable, $\psi$, on a triangular cell, $j$, as shown in Figure 2.3, the following equations, based on the scalar values calculated in right and left hand sides (Mohammadian and Le Roux, 2006), are used.

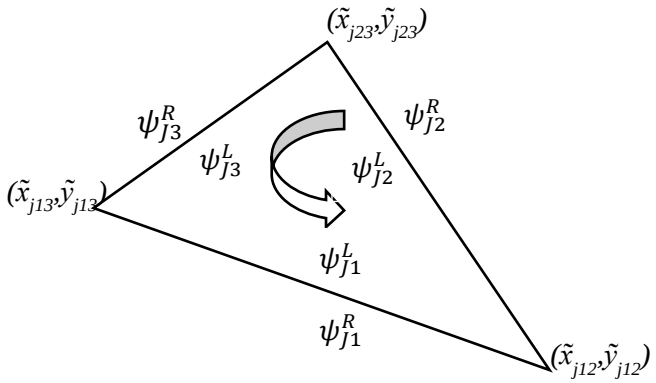


Figure 2-3 Notations used in calculating the spatial derivatives

$$\left(\partial\psi/\partial x\right)_j = \frac{1}{|T_j|}\int_{T_j}\frac{\partial\psi}{\partial x}dxdy \approx \frac{\psi_{j1}\Delta y_{j1} + \psi_{j2}\Delta y_{j2} + \psi_{j3}\Delta y_{j3}}{A_i}$$

$$\left(\partial\psi/\partial y\right)_j = \frac{1}{|T_j|}\int_{T_j}\frac{\partial\psi}{\partial y}dxdy \approx \frac{\psi_{j1}\Delta x_{j1} + \psi_{j2}\Delta x_{j2} + \psi_{j3}\Delta x_{j3}}{A_i} \qquad (2.30)$$

where,

$$\begin{aligned}
&\Delta y_{j1} = y_{j3} - y_{j2}, \quad &&\Delta x_{j1} = x_{j3} - x_{j2}, \quad &&\psi_{j1} = (\psi_{j1}^{L} + \psi_{j1}^{R})/2\\
&\Delta y_{j2} = y_{j1} - y_{j3}, \quad &&\Delta x_{j2} = x_{j1} - x_{j3}, \quad &&\psi_{j2} = (\psi_{j2}^{L} + \psi_{j2}^{R})/2\\
&\Delta y_{j3} = y_{j2} - y_{j1}, \quad &&\Delta x_{j3} = x_{j2} - x_{j1}, \quad &&\psi_{j3} = (\psi_{j3}^{L} + \psi_{j3}^{R})/2
\end{aligned} \qquad (2.31)$$

## 2.3. Numerical Examples

Various aspects of the numerical method explained above are further tested and verified in this section. The accuracy of the method is tested for several benchmarks and compared to the available solutions in the literature. Also in order to justify and highlight the well-balanced property of the solution, the results of a well-balanced and non-well-balanced solutions for small perturbations are compared for the last two test cases.

### 2.3.1. Flow over a hump (obstacle)

In order to verify the accuracy of the solution, this numerical example is adopted from Bryson et al. (2010). The scheme is applied to the system described in Equation (2.32), with gravitational constant $g$ = 1, and the following initial values and bottom topography:

$$\omega(x,y,0) = 1, \qquad u(x,y,0) = 0.3, \qquad B(x,y) = 0.5\exp(-25(x-1)^2 - 50(y-0.5)^2) \tag{2.32}$$

The simulation time-step was set to 0.001 sec. The computational domain is $[0,2] \times [0,1]$, with a total number of triangular elements of $4 \times 200 \times 200$ as shown in Figure2.4(a). The elliptical topography of the hump is shown in Figure 2.4(b).

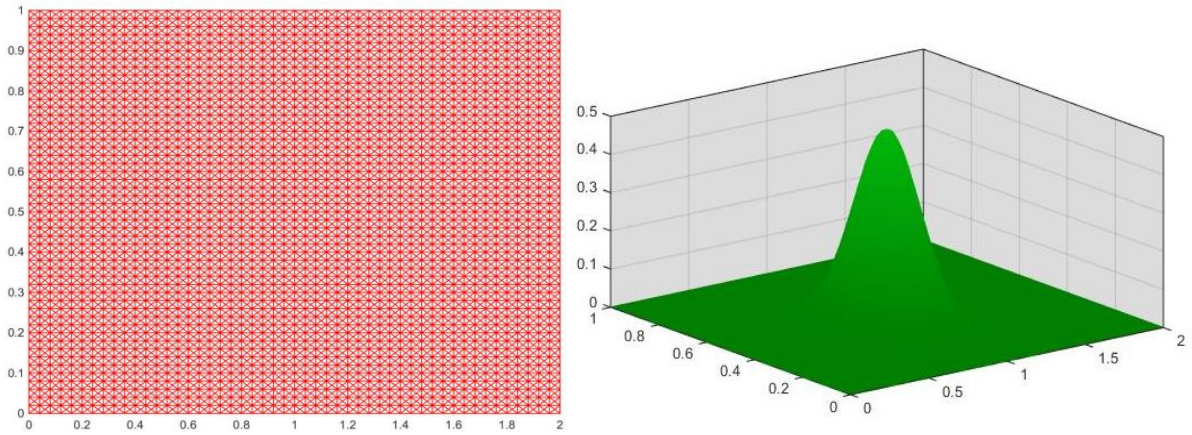


(a) (b)

Figure 2-4(a) Grid, and (b) bed topography used for benchmark 1

The solution reached a steady-state at the time $t$ = 0.07 sec, which is exactly identical with that in the reference solution of Bryson et al. (2010).

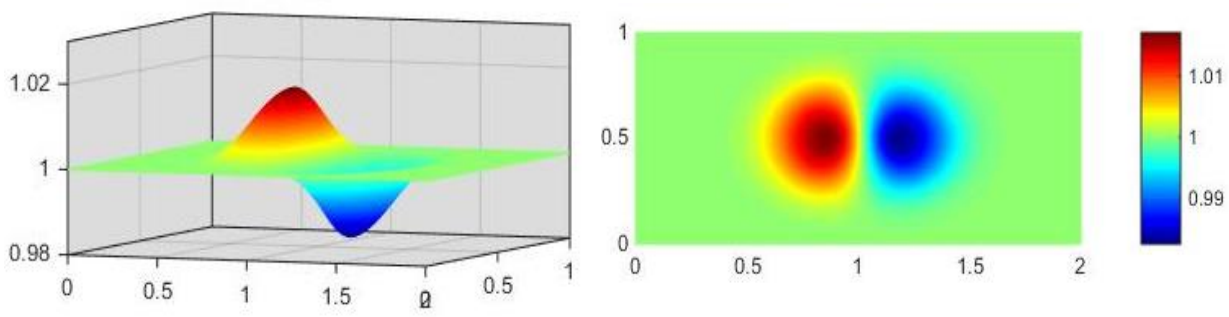


(a) (b)

Figure 2-5 Water surface level for benchmark 1, at t=0.07 s: (a) 3-D view, (b) top plot

### 2.3.2. Partial dam break with constant and variable density

As discussed in Brice et al. (2010), the partial dam break test has been a standard test for examining the accuracy of shock capturing methods for the shallow water solutions. Here, this test is divided into two sub-cases for examining the accuracy of the current solution for constant and varying density problems. The geometry of the cases is identical and consists of a 200×200 m grid discretized into a 40×40×4 triangular mesh. The middle part of the dam is removed instantaneously to examine the free flow of the water from the upstream as shown in Figure 6(b). The boundary conditions used in the analysis are rigid, and the friction of the fluid with the bed is neglected.

*2.3.2.1. Constant density case*

For the first case, the density of the water on both sides of the dam is assumed to be 1000 kg/m$^3$, and the depth of the water in the upstream and downstream domains are 10 and 5 m, respectively. The results of the analysis after 7.3 sec are captured in order to be verified with the solution provided by Brice et al. (2010). The water surface shown in Figure 2.6(a) is almost identical to the solution in Brice et al. (2010). Also, the velocity vectors in the domain are shown in Figure 2.6(b).

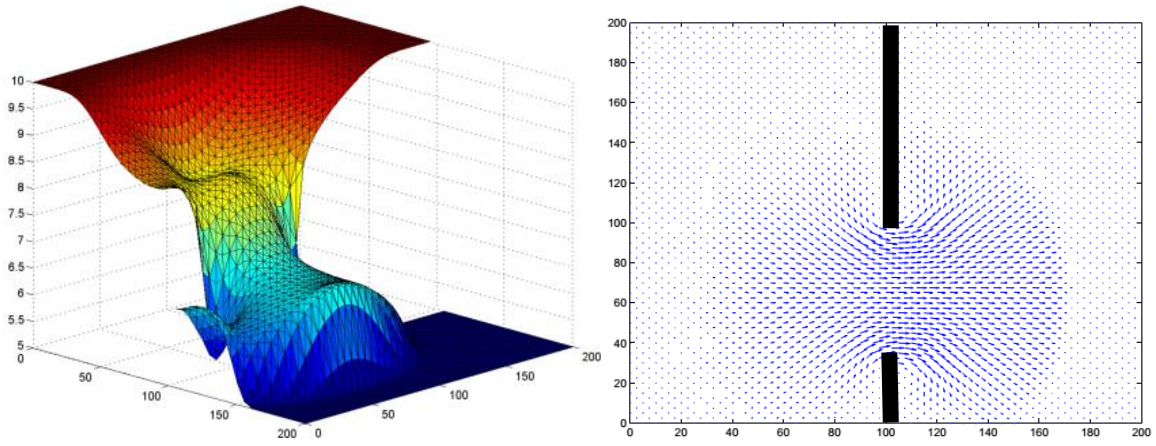


(a) (b)

Figure 2-6(a) Water surface elevation, and (b) water velocity vectors at 7.3 sec after the start of the analysis

*2.3.2.2. Variable density case*

For the second test, the authors used a variable density dam break problem. The density of the water in the upstream domain and the downstream one is selected to be 1200 and 1000 kg/m$^3$,

respectively. The results indicate that the flow direction is from the fluid with higher density towards the fluid with smaller density, due to the hydrostatic pressure difference at the interface of the two fluids. Therefore, due to conservation of mass principle, the surface of the lower density fluid rises, as shown in Figure 2.7(a). In Figure 2.7(b), the distribution of the density in the interface of the fluids is presented: the results demonstrate that the smooth solution and the symmetry are preserved.

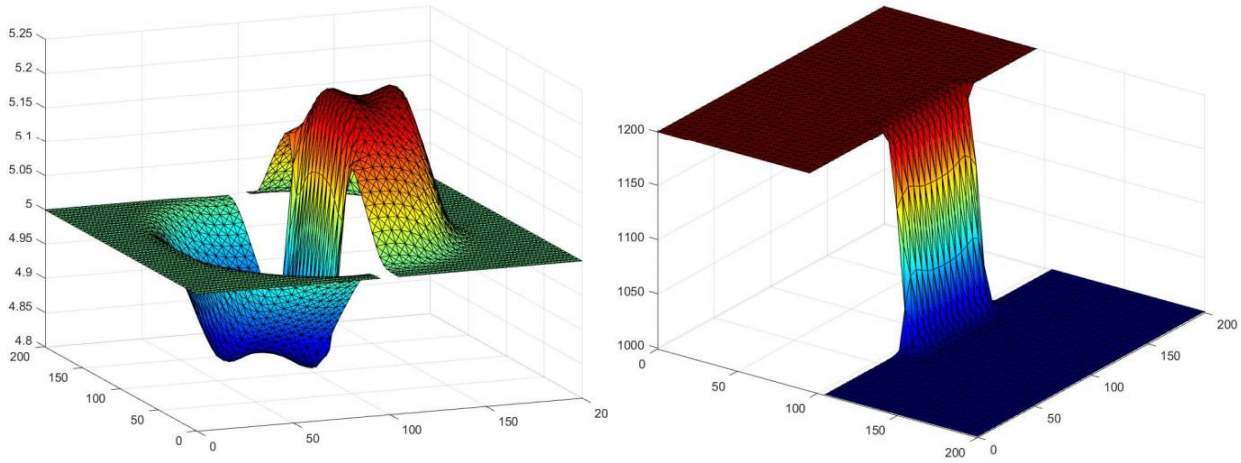


(a) (b)

Figure 2-7(a) Water surface elevation, and (b) density distribution 5.2 sec after the dam break initiation

### 2.3.3. Variable density circular dam break

Circular dam break has been examined by many researchers including Alcrudo and García-Navarro (1993) and Toro (2001). The test consists of an idealised circular dam with infinitely thin circular wall of radius $r_c$= 1.5 m around the dam which is centred at $x_c$= 15 m and $y_c$= 15 m in a square basin (30 m x 30 m) with horizontal bed (symmetric problem). Throughout the domain, the velocities are zero ($u$ = $v$ = 0); and initial water depth is:

$$h\,(x,y) = \begin{cases} h_{dam} = 2\,m & if\ (x-x_c)^2 + (y-y_c)^2 \le r^2 \\ h_{domain} = 1\,m & if\ (x-x_c)^2 + (y-y_c)^2 > r^2 \end{cases} \quad (2.33)$$

The initial values used for this test case are the following: the acceleration due to gravity is g = 9.81 m/s$^2$; to see the differences between constant density and variable density, the density of the liquid inside of the wall are 1000 and 200 kg/m$^3$ respectively; the density of the liquid outside of

the wall is 1000 kg/m$^3$; the spatial steps are dx = 0.1 m and dy = 0.1 m; the time step is dt = 0.002 s; The thin wall around the dam collapses at t = 0. After the collapse of the cylindrical wall at t = 0 (s), the system tends toward an equilibrium steady state condition when a hydrostatic pressure thrust balance is achieved.

In the first case with $\rho_{in}$=1000 kg/m$^3$, the ratio of the hydrostatic pressure thrusts is equal to unity. As it is shown in Figure 2.8, after the cylindrical thin wall is removed and the system is set free, gravity and density differences between the liquids (inside and outside the wall) cause a circular bore to propagate outwards (towards the boundaries of the computational domain). In the other case $\rho_{in}$=200 kg/m$^3$, the initial hydrostatic pressure thrust inside the circular dam is less than that outside the dam, which means that the process will be reverse of that in the other case, since the ratio of the hydrostatic pressure thrusts is greater now 0.8, which is less than unity. Figure 2.9 and Figure 2.10 show the predicted free surface elevation and the depth averaged velocity profiles in the *x*-direction along the centreline of the domain at t=0.55 respectively.

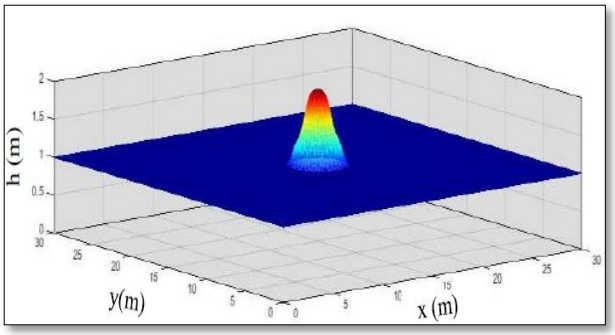


t=0.17 (s)

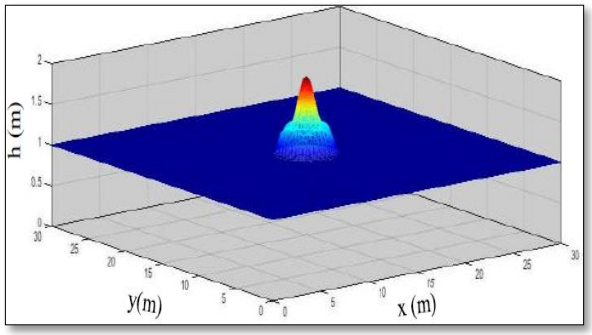


t=0.35 (s)

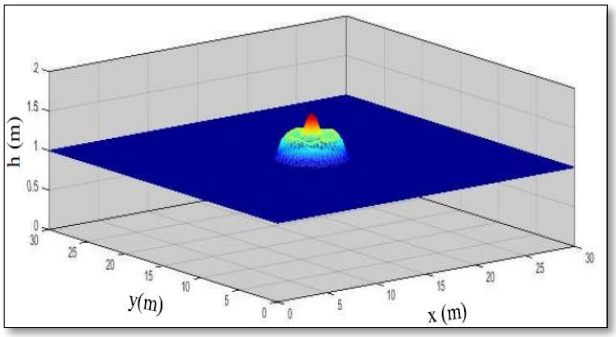


t=0.55 (s)

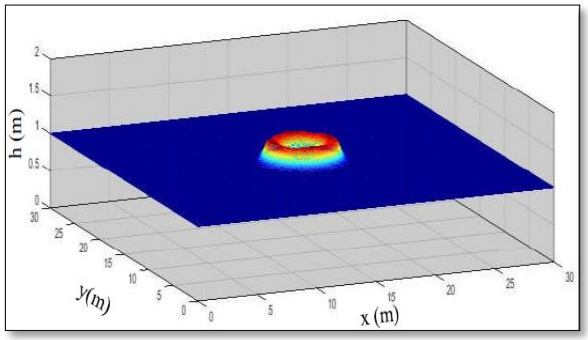


t=1 (s)

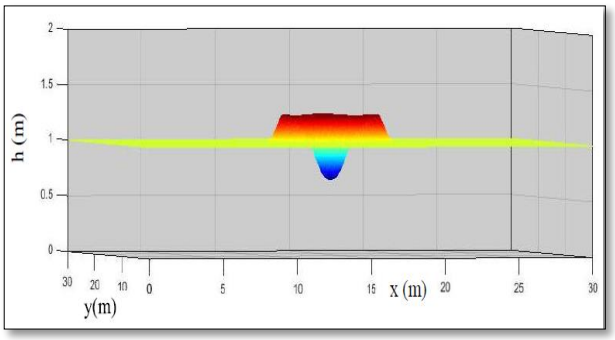


t=1.25 (s)

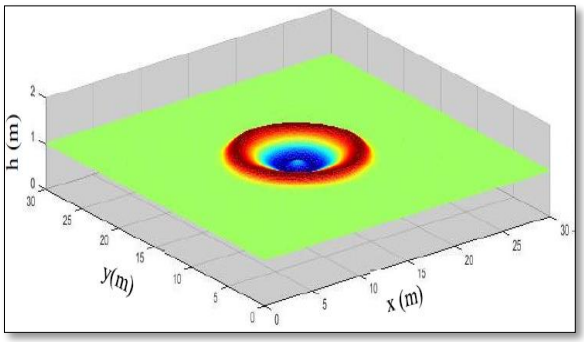


t=1.7 (s)

*Figure 2-8 Variable density circular dam break, $\rho$in $R= 1000\ kg/m^3$, Free surface elevation visualisations at different times.*

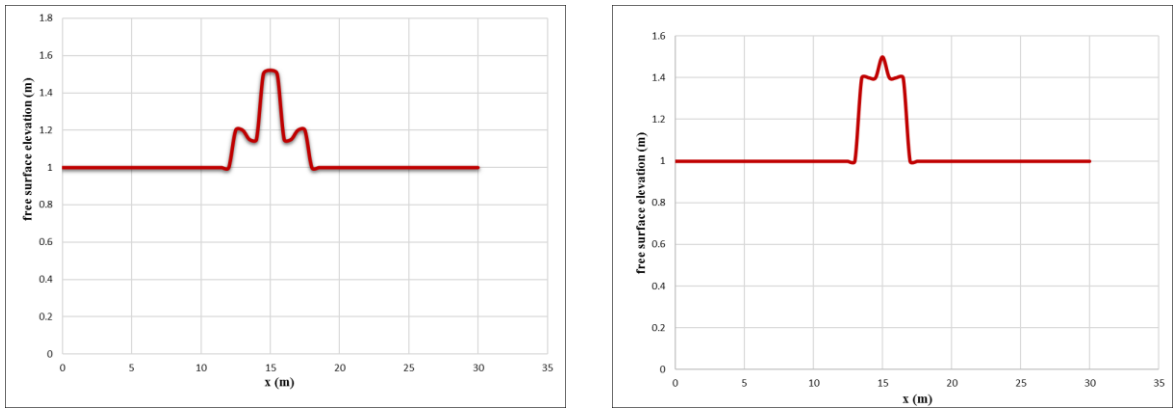


(a) (b)

Figure 2-9 Variable density circular dam break, Predicted free surface elevation at t=0.55(a)ρin R= 1000 kg/m$^3$, (b) ρin R= 200 kg/m$^3$

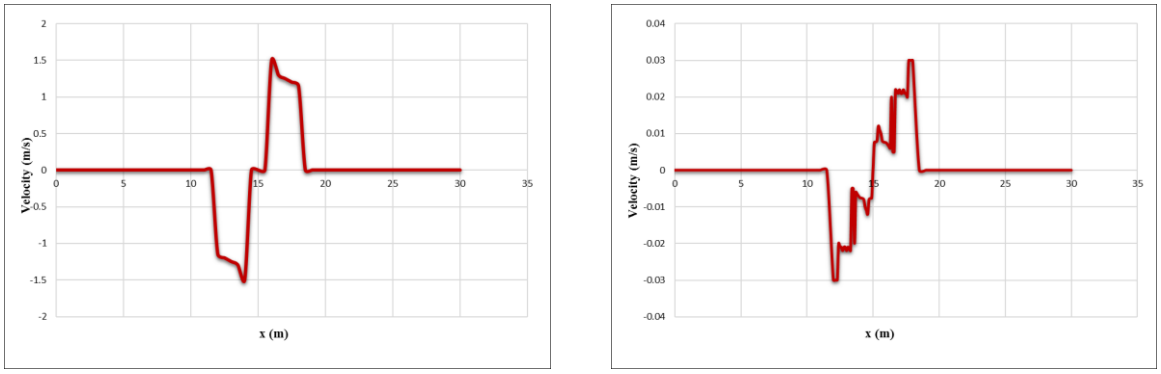


(a) (b)

Figure 2-10 Variable density circular dam break, Predicted depth-averaged velocity in x direction at t=0.55. (a)ρin R= 1000 kg/m$^3$, (b) ρin R= 200 kg/m$^3$

### 2.3.4. Dam break over dry bed problem

This dam break test, designed by Toro (2001), is widely used for validation of the numerical model for wet and dry flows over a horizontal bed. The channel is 50 m long. The initial conditions considered are 1 m water depth for $x < 20$ m and dry bed for $x > 20$ m, as shown in Figure 2.11(a). Extrapolation boundary conditions are applied at the ends of the domain. The time step is 0.001 s. Figures 2.11 (b) and (c) show the flow state at time $t = 4$ s. According to (Toro 2001), the difficulty

is to propagate the wet and dry front at the correct flow velocity, also to avoid spurious oscillations in the velocity profile. The present results are very similar to the reference solution (Toro 2001).

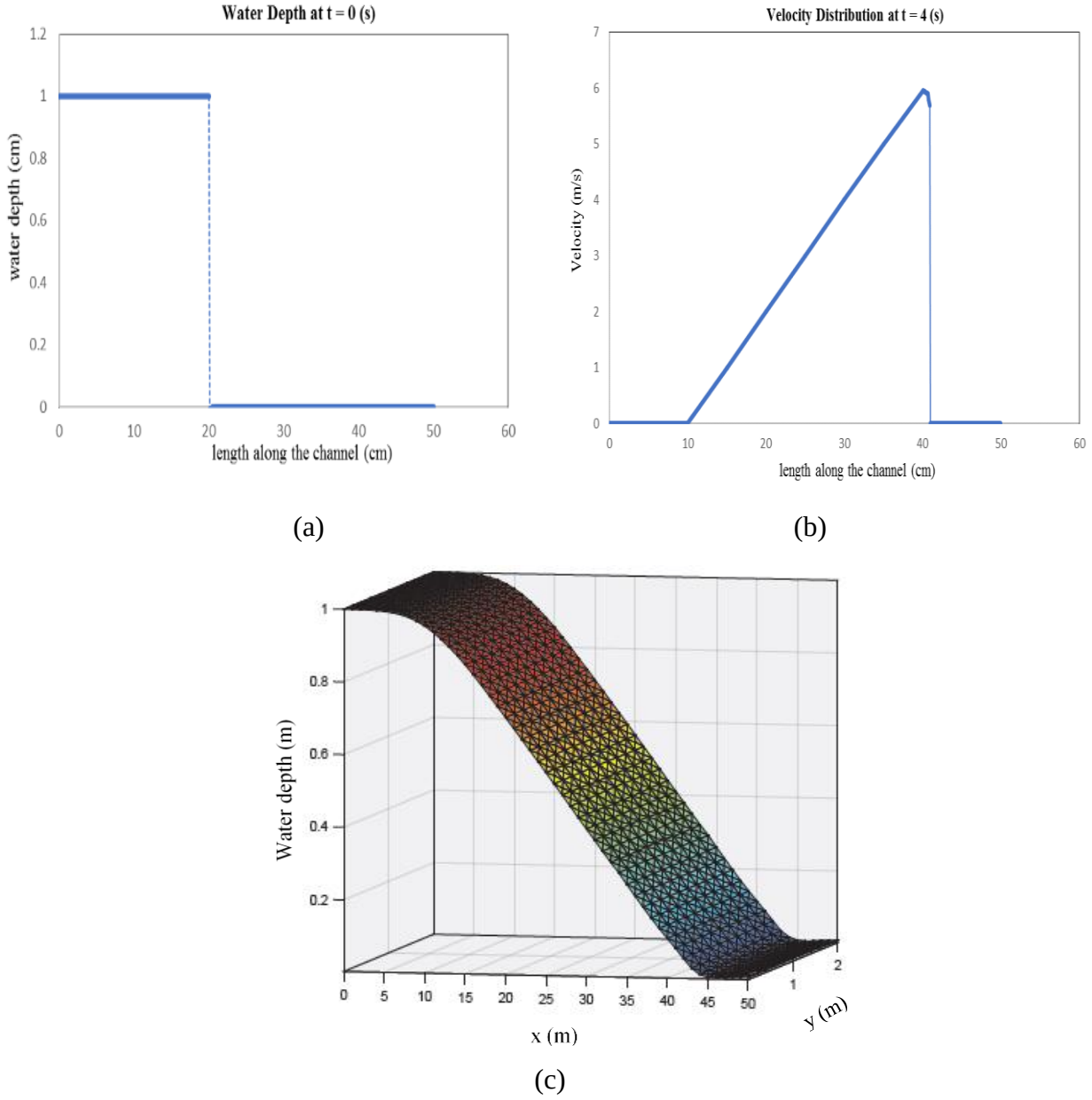


Figure 2-11 Dry bed test case (a) initial depth profile, (b) velocity distribution at t= 4 (s), and (c) depth profile at t= 4 (s)

### 2.3.5. Small perturbation in a steady-state solution

This test case has been chosen to verify the well-balanced property of the proposed central-upwind scheme. The results are compared with non-well-balanced method to confirm the importance and

advantage of using a well-balanced scheme. The computational domain is [0, 2] × [0, 1] discretized into 4×200×200 triangles and the time step is $\Delta t$ = 0.001 sec. The bed topography is given as (2.34) as shown in Figure 2.12 (a).

$$B(x,y) = 0.8\exp[-5(x-0.9)^2 - 50(y-0.5)^2] \qquad (2.34)$$

Initially the water surface and the density are constant everywhere over the entire domain except for $0.05 < x < 0.15$, where a different density (see Figure 2.12 (b)) and water surface are used and which is described by the following.

$$\omega(x,y,0) = \begin{cases} 1.001, & 0.15 < x < 0.20 \\ 1, & otherwise \end{cases} \qquad \mathrm{u(x,y,0)} \equiv \mathrm{v(x,y,0)} \equiv 0$$

$$\rho(x,y,0) = \begin{cases} 1007, & 0.15 < x < 0.20 \\ 997, & otherwise \end{cases} \qquad (2.35)$$

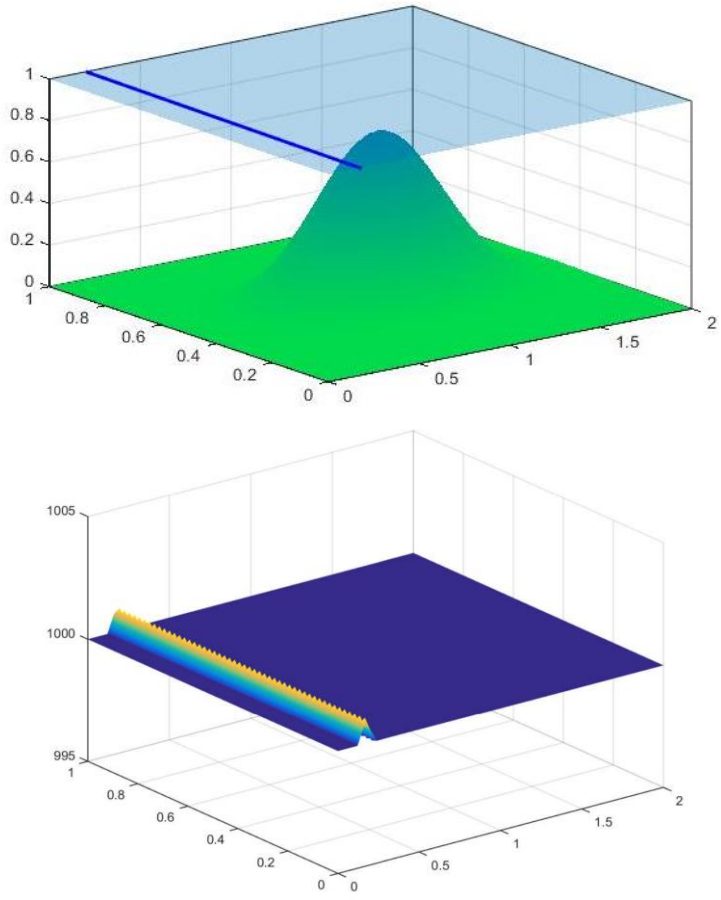


(a)

(b)

Figure 2-12(a) Topology, and (b) density perturbation in benchmark 5

A perturbation in density and water depth is imposed, in order to see the waves, it can cause. The water surface elevation, $\omega$, at various times is shown in Figure 2.13. The solution computed using the non-well-balanced scheme has significantly more oscillations and contains waves which sometimes have the same magnitude as the waves generated by the perturbation. Therefore, this test demonstrates the advantage of using the proposed well-balanced scheme.

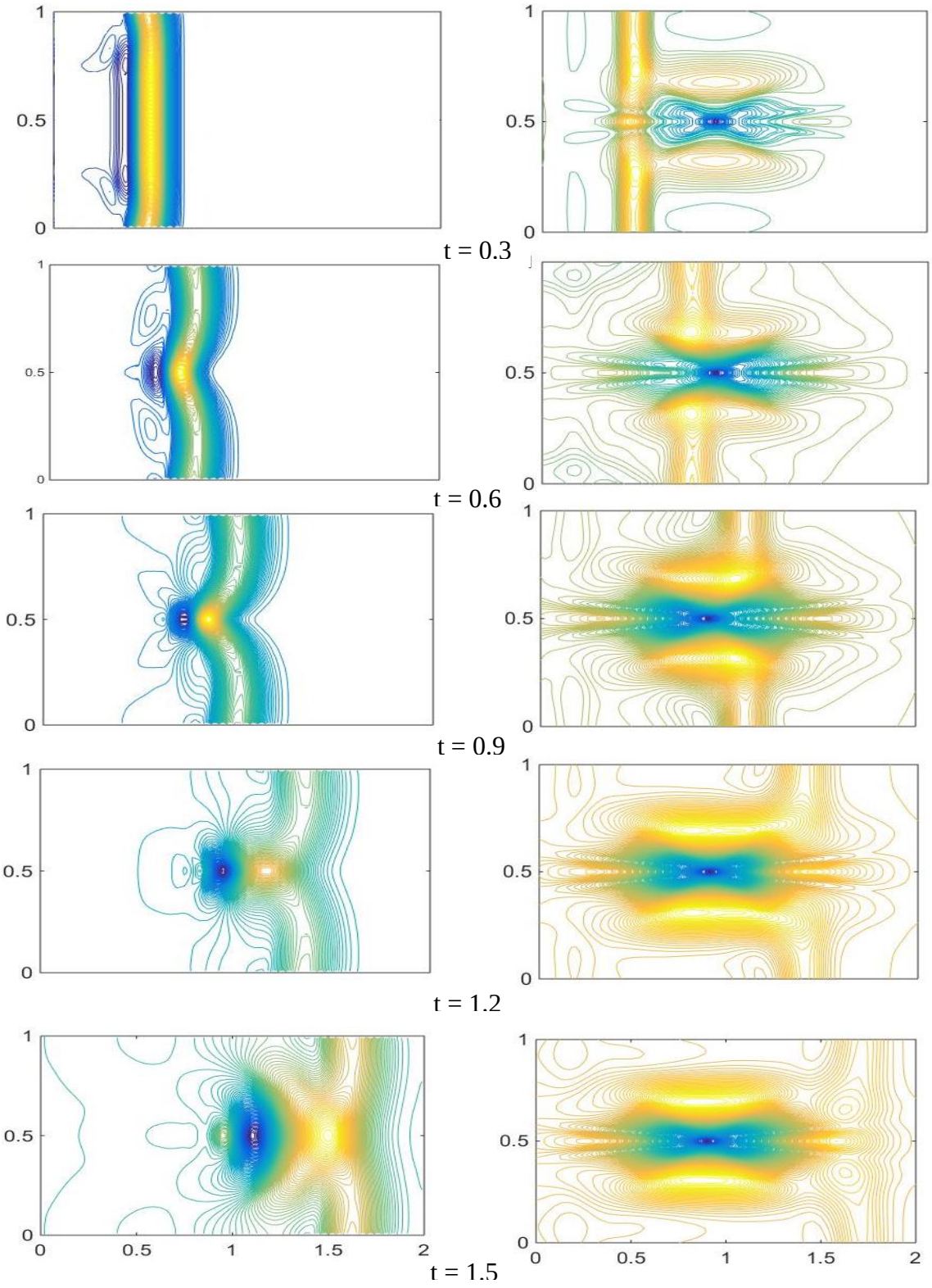


Figure 2-13 Time history of the water surface elevation computed using the well-balanced (left column) and non-well-balanced (right column) central upwind scheme.

### 2.3.6. Side-channel problem with flow over two islands

The inflow of a tributary branch carrying a different density from the main flow, which can be the case of a river confluence, represents a typical surface discharge. Examples of such discharges are common in nature in addition to hydraulic, environmental and industrial applications. An important example of this type of discharge is wastewater discharge into the main flows following treatment in special facilities.

Based on the examples mentioned above, this test is designed so that the domain consists of two tributaries with different density, moving over a floodplain while exhibits two humps (obstacles). The author chose this test to further demonstrate the advantage of using the well-balanced scheme against a non-well-balanced one.

The computational domain is a 75×30 m river reach, which has been discretized into 150×60×4 cells. The main flow has the *x-velocity of 0 m/sec*, while the secondary branch inflows from a side channel 8 m wide, with y-velocity of 2 m/sec as shown in Figure 2.14 (a). The main river has the initial bed elevation described by (Figure 14, b).

$$B(x,y) = max[0,\quad 0.3\exp(-0.025(x-20)^2 - 0.075(y-15)^2)\,, \\ 0.6\exp(-0.025(x-20)^2 - 0.075(y-15)^2)] \qquad (2.36)$$

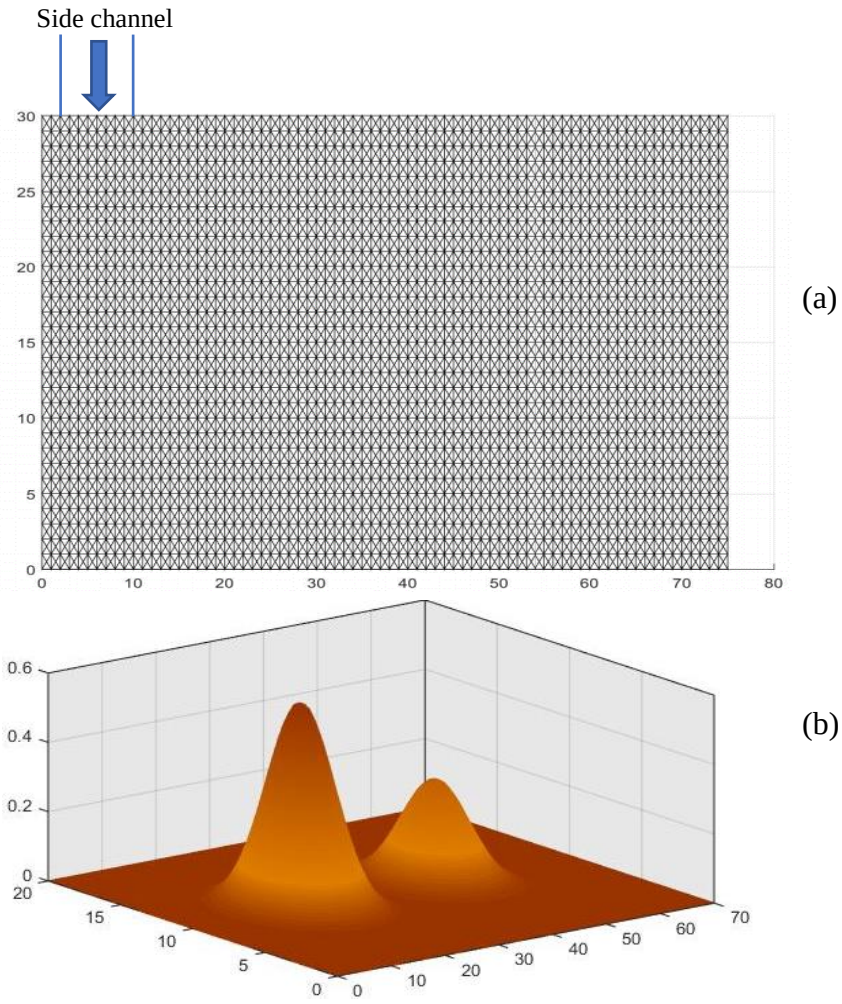


Figure 2-14(a) Plan view, and (b) bed topography in benchmark 6

The initial values used for this test case are as follows: the gravitational acceleration is $g = 9.81\ m^2/s$, the density of the ambient current and effluent are 997 and 1007 kg/m$^3$ respectively, the water surface for the side channel is 1.0001 m and for main domain is 1 m, and the selected time step is $\Delta t$ = 0.001 s.

The results of the simulation in terms of water surface elevation is presented at various times instants in Figure 2.15. The results obtained using the well-balanced and the non-well-balanced solutions are compared. This comparison reinforces the conclusions of the previous test case, as it shows a significant difference between the well-balanced and non-well-balanced schemes: the well-balanced scheme can successfully eliminate oscillations developed in the non-well-balanced method.

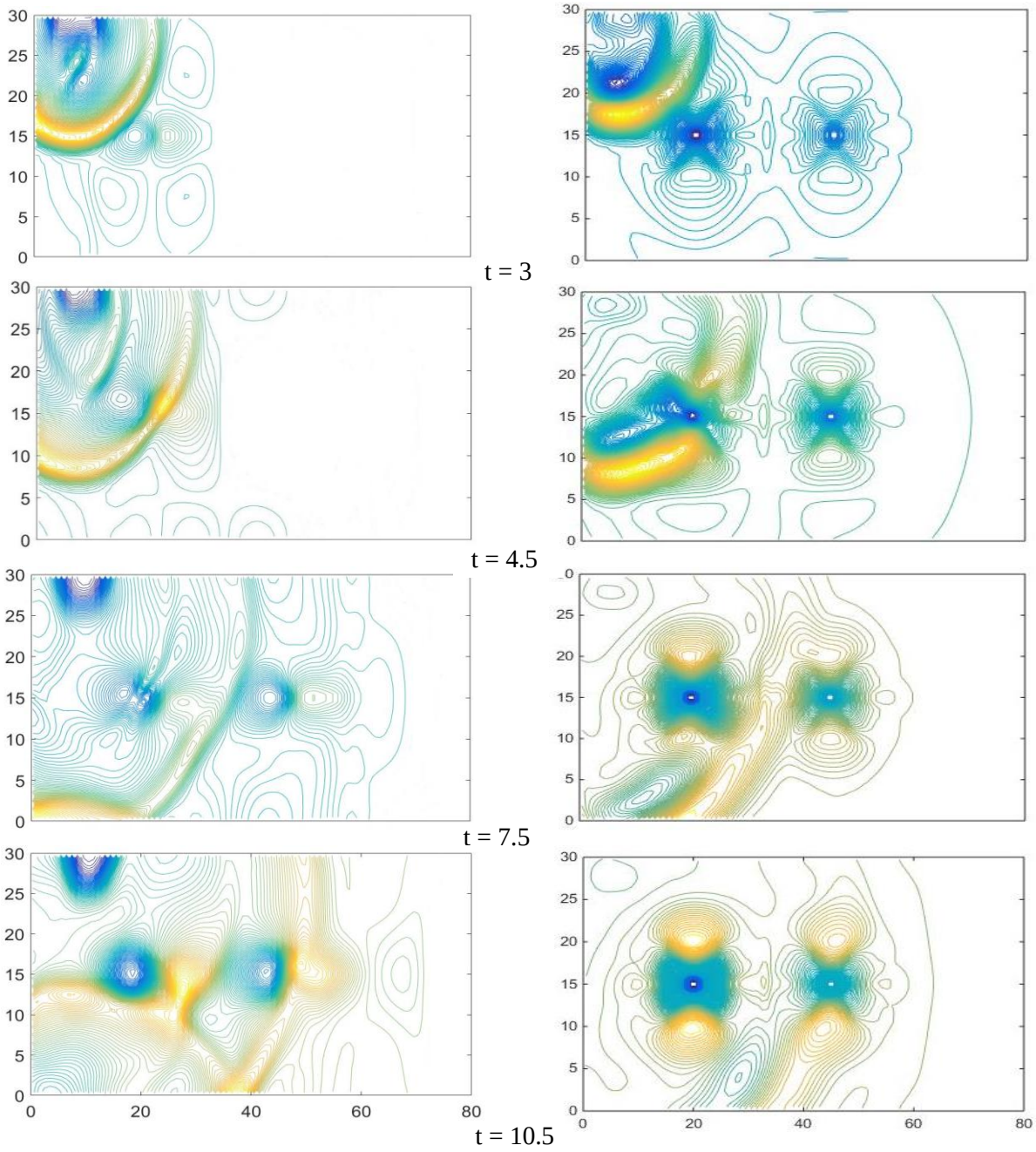


Figure 2-15 Time history of the water elevation in the solution computed by the well-balanced (left column) and non-well-balanced (right column) central upwind scheme in benchmark 6

## 2.4. Conclusions

In this study, application of the central upwind scheme to solve the variable density shallow water equations is presented, where both well-balanced and positivity preserving properties are achieved over an unstructured grid. Using this scheme, the methodology is used on a triangular grid. The

evaluation of the accuracy of the solution, along with its different properties was demonstrated for a number of well-known benchmark test cases. The ability of the method to solve constant density problems was compared with other results available in the literature. Furthermore, numerical experiments highlighted the ability of the scheme to study variable density flows.

The fourth benchmark test case in Section 3.3 validated the positivity preserving property of the scheme in a flow over a dry bed. The fifth benchmark test presented in Section 3.4 verified the well-balanced property of the solution by comparing its results with the results of the highly disturbed and oscillated non-well-balanced-scheme. In the sixth test case detailed in Section 3.5, the scheme was applied to a practical variable density mixing problem as one of the major applications of the shallow-water methodologies.

# 3. Large Eddy Simulations of Two-Layer Exchange Flows over a Bottom Sill [2]


## Abstract

In the present study, a detailed numerical investigation is performed using the Large Eddy Simulation (LES) approach with the Smagorinsky sub-grid-scale (SGS) model to simulate the characteristics of the mixing process of a two-layer flow over a dune. The numerical results include simulations of the mean velocity and density profiles, interfacial instabilities, and estimation of the entrainment rate. Experimental tests were also conducted using the Particle Image Velocimetry (PIV) and Laser Induced Fluorescence (LIF) techniques, and the results used for validation and further comparison with the LES numerical results. A numerical simulation is also done using Reynolds-averaged Navier-Stokes (RANS) equations to evaluate the quality of the predicted results for the RANS and LES methods. Overall, the LES results were able to accurately reproduce the characteristics of the two-layer exchange flows in most aspects. The developed model was also able to reproduce the Kelvin–Helmholtz (KH) instabilities and interfacial waves in two-layer exchange flows.



*Keywords*: Large eddy simulations, two-layer hydraulics, Interfacial waves, Kelvin–Helmholtz (KH) instabilities, PIV-LIF technique.


### 3.1. Literature review and research needs

Studying multi-layer hydraulics is essential for various applications, from the mixing of fluids and flows with different densities and temperatures to deep oceanic currents. When two water bodies with different densities are connected by a narrow channel, a stratified two-layer flow and consequently a shear interface between the two fluids is generated. This phenomenon, which is termed *internal hydraulics*, commonly occurs in estuaries or straits. Typical examples are the exchange of more saline Mediterranean Sea water with the less saline Atlantic Ocean water through the Strait of Gibraltar (Armi and Farmer, 1988) and the summer exchange of warmer, more polluted Hamilton Harbor water of higher density with Lake Ontario water through the Burlington shipping channel (Hamblin and Lawrence, 1990)

[2] Sepideh Khorshid, Abdolmajid Mohammadian, Ioan Nistor, Jose Anta, Enrique Peña González, Manuel Regueiro "Large Eddy Simulations of Two-Layer Exchange Flows over a Bottom Sill", Journal of **Applied Ocean Research**, Under Review.

Stommel and Farmer (1953) first studied two-layer flows in which the interaction of the two layers was considered in the behavior of the flow, while Schijf and Schonfeld (1953) considered the effect of friction on the motion of the two layers. Following the numerical investigation by Houghton and Isaacson (1970), the blocking of a two-layer flow over a mountain ridge for initially uniform flows upstream and downstream was experimentally investigated by Long (1974). Despite the initiation of some research work related to two-layer hydraulics, frameworks to analyze these flows were only later proposed by Armi (1986) and Armi and Farmer (1988); however, their treatments were limited only to cases with a stable interface. Focusing on flow hydraulics, Lawrence (1993) numerically and experimentally studied a steady two-layer flow moving in one direction over a fixed, two-dimensional obstacle.

While earlier research focused more on the hydraulics of the flows, it was later observed that at interfaces of two-layer flows, interfacial instabilities such as Kelvin-Helmholtz (KH) billows can develop. In fact, earlier studies (Pratt, 1987) showed that interactions between baroclinic effects (due to density differences) and related interfacial instabilities can result in certain mixing processes. Previous research on mixing in stratified lakes and oceans has also shown that these hydrodynamic instabilities are largely responsible for the vertical mixing within oceans and lakes (Thorpe, 1985 and Fernando, 1991).

Differentiating various types of shear instabilities is based on the shear layer thickness (also known as vorticity thickness), $\delta = {\Delta U}/{(\partial u/\partial z)_{max}}$, and the density layer thickness $\eta = {\Delta\rho}/{(\partial\rho/\partial z)_{max}}$, where $U$ and $\rho$ are the velocity and density of each layer, respectively, and $\partial$U and $\partial\rho$ are respectively the velocity and density differences between the two layers. In cases when $\eta$ and $\delta$ are close, such as stable stratified shear flows, the primary mode of instability is termed the Kelvin-Helmholtz (K-H) instability, which consists of a series of billows flowing with a phase speed equal to the mean velocity (Turner, 1973).

Using flow visualization and particle image velocimetry, Morin et al. (2004) were able to observe large periodic fluctuations in an experiment on a two-layer exchange over a smooth bottom sill within a maximal exchange period, and showed that these fluctuations in the interface position and the flow rate were caused by KH instabilities and internal seiches.

Based on Haigh & Lawrence (1999), Kelvin-Helmholtz instabilities are only likely to happen when the Bulk Richardson number, $R_i = g'\delta/(\Delta U^2)$ , is within $0.046 < R_i < 0.071$, where $g' = g(\rho_2 -$

$\rho_1)/\rho_2$ is the reduced gravity, and $\rho_1$ and $\rho_2$ are the densities of the upper and lower flow layers respectively.

However, flow behaviors change when steady or unsteady external forces are superimposed on a pure baroclinic flow. Negretti et al. (2007) examined the effects of the barotropic forces produced by pressure differences occurring at the beginning of their experiment on the formation and flow characteristics of large-scale KH instabilities.

Although many experimental investigations have been done on density current flow dynamics on sloping boundaries, fewer numerical studies have dealt with the flows of density currents on slopes. Since computational resources are continuously improving, detailed computational information about the mixing of two-layer flows can be obtained at a fraction of the cost of a physical experiment.

Dade et al. (1994) modeled the two-dimensional propagation of a turbulent density current moving down an inclined surface, while Kneller et al. (1999) obtained the equation for the velocity profile by considering the turbulence and fluid stresses in a two-dimensional density current flow.

Modeling propagation of the gravity currents up a slope using a three-dimensional simulation, Ottolenghi et al. (2014) showed that the thickness of the current head and the magnitude of flow reversal is affected by the slope angle. He also conducted a large-eddy simulation (LES) to investigate entrainment in lock exchange gravity currents (Ottolenghi et al. 2016), and it was observed that ambient fluid entrainment into the dense layer is reduced by increasing both the initial lock aspect ratio (height to length ratio) of the dense fluid and the bottom upslope. Compared to the Reynolds-averaged Navier-Stokes (RANS) equations, the LES method can be expected to obtain more accurate results for the mixing behavior, since it resolves the larger and thus most important turbulent eddies, and models only the small-scale motions. It should be mentioned that the main disadvantage of LES is the high computational cost resulting from the fine grids in addition to the fine time steps used for the direct prediction of the instabilities.

Nourazar and Safavi (2017) carried out a two-dimensional LES simulation and compared their results with previous three-dimensional studies. The results of the simulation showed that as the inverse slope of the inclined surface increases, the mixing in the body of the dense fluid with the ambient fluid increases at the beginning of the slope because of vortices generated by the flow reversal, whereas the mixing in the head of the density current generally decreases.

In present study, a comparative study is conducted on the performance of the LES and RANS methods in predicting complicated three-dimensional flow characteristics in a two-layer flow over a dune, and shows that the LES is highly superior to RANS for this complex flow, and that only the LES results matched well with those of the experiments. This paper aims at performing a further comparative study on LES and RANS computations, focusing on the characteristics of two-layer flows with different densities over an isolated dune, especially with regard to reproducing the interfacial fluctuations originally reported by Negretti et al. (2007). The authors performed the experimental work at the University of A Coruña, Spain, and the resulting data were used to validate the numerical models.

In the following, first, the computational methodology is introduced, and then the numerical results are presented and compared with the experimental ones.

### 3.2. LES methodology

Stratified flows can be modelled using Computational Fluid Dynamics (CFD) techniques. A wide range of diverse numerical methods has been introduced and utilized to simulate stratified flows, including the Reynolds-averaged Navier-Stokes (RANS) method (e.g., Anta et al., 2016), which is the most widely used approximation, as well as the Large-Eddy Simulation (LES) (e.g., Constantinescu, 2014) and Detached-Eddy Simulation (DES) methods.

It is well-known that RANS-based models have limited accuracy for turbulent quantities. To overcome these issues, advanced models such as LES, DES, or hybrid LES/RANS models are now being increasingly applied for such simulations. In contrast to RANS equations, in which all scales are modeled in the same way, in the LES approach, large- and small-size eddies are reproduced based on the local grid spacing. Small scales for flows tend to be more universal and less determined by boundary conditions, and are hence modelled based on assumptions such as the Boussinesq hypothesis. Large scales are affected strongly by boundary conditions and are therefore computed directly by solving the instantaneous Navier–Stokes equations. The LES method resolves the large turbulent motions of a flow and models only the smaller scales, and it is thus able to capture the unsteadiness of a flow. Therefore, in spite of being computationally more expensive than the RANS approach, using the LES is believed to be more suitable for this kind of simulation.

### 3.2.1. Governing Equations

Larger turbulent eddies, which are the most energetic and are responsible for the majority of turbulent transports, are resolved directly in a computational grid in the LES method, whereas eddies smaller than the grid size are assumed to be isotropic and are modeled using a Sub-Grid-Scale (SGS) model. The governing equations for the LES method are obtained by filtering the original Navier-Stokes equations. The filtered continuity, momentum, and concentration transport equations for the Cartesian coordinates for the LES method are as follows (Pope, 2002):

$$\frac{\partial \rho u_j}{\partial x_j} = 0 \tag{3.1}$$

$$\frac{\partial \rho u_i}{\partial t} + \frac{\partial \rho u_i u_j}{\partial x_j} + \frac{\partial p}{\partial x_i} = \rho g_i + \frac{\partial^2}{\partial x_j^2}(\mu u_i) - \frac{\partial \tau_{ij}}{\partial x_j} \tag{3.2}$$

$$\frac{\partial \rho \emptyset}{\partial t} + \frac{\partial (\rho \emptyset u_j)}{\partial x_j} = \frac{\partial^2}{\partial x_j^2}(\Gamma \emptyset) - \frac{\partial Q_j}{\partial x_j} \tag{3.3}$$

where $p$ is the pressure, $u_i$ and $u_j$ are the velocities in the x- and y-directions, respectively, $\rho$ is the fluid density, g is the gravitational acceleration, $\mu$ is the fluid viscosity, $\emptyset$ is the scalar concentration, Γ is the scalar diffusivity, $\tau_{ij}$ are the SGS Reynold stresses, and $Q_j$ is the SGS scalar flux.

Since the LES method does not resolve eddies smaller than the grid size, a sub-grid-scale (SGS) model must be applied through $\tau_{ij} = \overline{u_i u_j} - \overline{u_i}\,\overline{u_j}$. To solve the sub-grid component, $\tau_{ij}$, several models can be used, including the eddy-viscosity model, the Smagorinsky model, and the Wale model.

The Smagorinsky SGS model, the one most commonly used among the existing SGS models, is adapted herein. For the Smagorinsky model, $\nu_t$ is obtained:

$$\nu_t = l^2 \left|\tilde{S}\right| \tag{3.4}$$

where the strain-rate tensor $\left|\tilde{S}\right|$ is calculated as:

$$\left|\tilde{S}\right| = (2\overline{S_{ij}}\,\overline{S_{ij}})^{1/2} \tag{3.5}$$

$$l = C_s\overline{\Delta} \tag{3.6}$$

in which $\overline{\Delta}$ is the LES filter width (defined by the grid spacing) and $C_s$ is the Smagorinsky constant, which can be found by applying the proposed dynamic procedure by Germano et al. (1991) and modified by Lily (1992), as:

$$\mathrm{C}_s = \frac{1}{2}\frac{\langle L_{ij}M_{ij}\rangle}{\langle M_{ij}M_{ij}\rangle} \tag{3.7}$$

$$L_{ij} = \widehat{\tilde{u}_i\tilde{u}_j} - \hat{\tilde{u}}_i\hat{\tilde{u}}_j \tag{3.8}$$

$$M_{ij} = \Delta^2\widehat{|\tilde{S}|\,\tilde{S}_{ij}} - \hat{\Delta}^2|\tilde{S}|\tilde{S}_{ij} \tag{3.9}$$

where the angular brackets indicate a spatial averaging procedure over directions of statistical homogeneity while the overbar indicates the time-averaged variable and the caret indicates the spatially filtered quantities.

Also, in the Smagorinsky model, the SGS stress tensor and the SGS turbulent concentration flux are obtained as follows:

$$\tau_{ij} - \frac{1}{3}\tau_{kk}\delta_{ij} = -2\mu_t\tilde{S}_{ij} \tag{3.10}$$

$$Q_j = -\frac{\mu}{Sc_t}\frac{\partial\tilde{\emptyset}}{\partial x_j} \tag{3.11}$$

where $\tau_{kk}$ is the isotropic part of the SGS stress, which can usually be neglected for incompressible flows, while $Sc_t$ is the SGS turbulent Schmidt number, which is equal to 0.7.

### 3.3. Flow configuration and computational setup

The simulation domain was configured based on a series of flume tests carried out at the R+D Centre of Technological Innovation in the Building and Civil Engineering (CITEEC) department of the University of A Coruña (Spain). The layout of the hydraulic flume is shown in Figure 3.1. A dune configuration was located in the middle of the flume, which had a narrower channel, in order to assess the effects of the barrier on the mixing processes. A wall above the dune crest separates the two flows of different density.

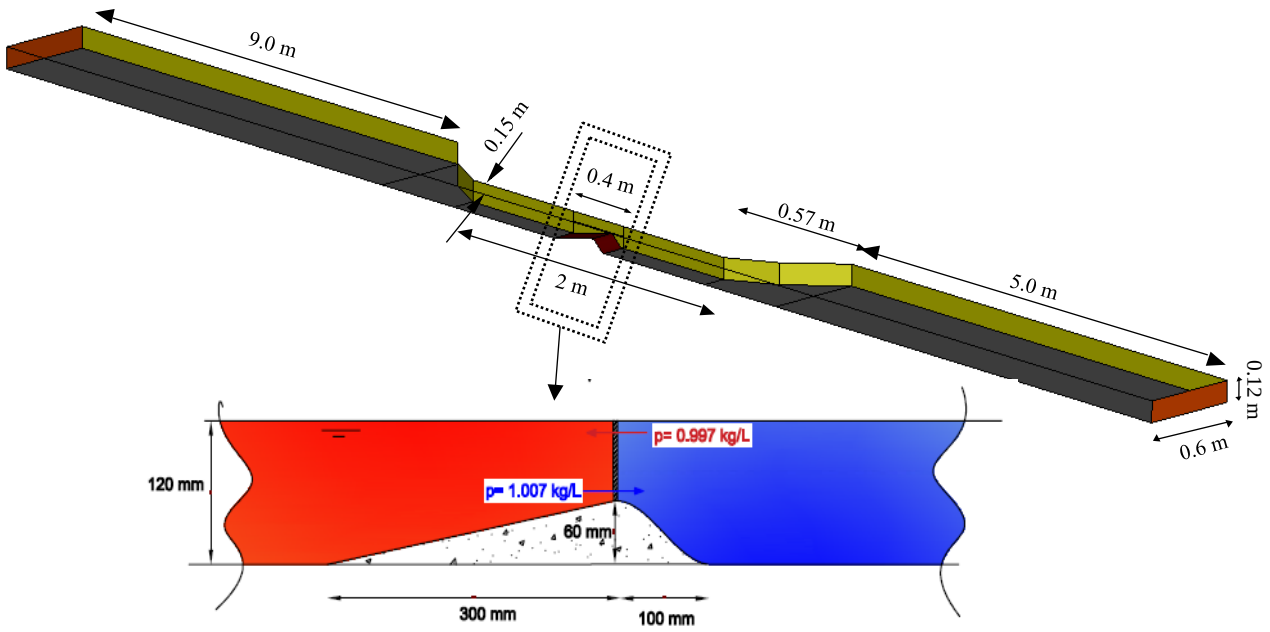


Figure 3-1 Hydraulic flume layout and computational domain used in LES model of flow over a dune

The computational domain was discretized with an unstructured mesh with increasing grid spacing from the center of the dune to the boundaries, as shown in Figure 3.2 The grids were created using the SALOME mesh generator and imported into OpenFOAM. More grid refinement was performed around the dune to show the capability of the model in reproducing shear interfacial instabilities like Kelvin-Helmholtz or barotropic seiches.

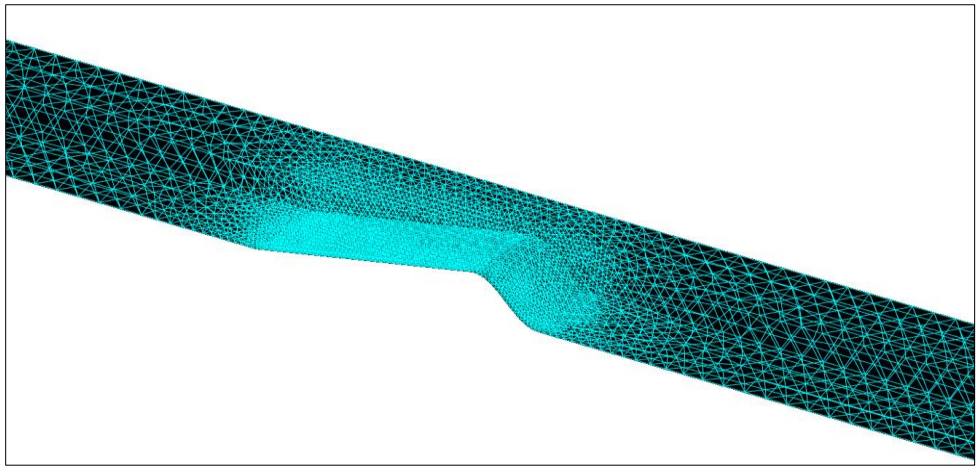

Figure 3-2 The unstructured mesh of the domain of the LES model of flow over a dune

The boundary condition at the top surface was set to free-slip, while a zero-gradient open boundary was used for the outer boundaries. The implementation in OpenFOAM was performed with the turbulent solver InterMixingFoam and Smagorinsky SGS models. The density difference between the two fluids was also defined based on the experimental conditions.

### 3.3.1. Experimental set up

Anta et al. (2011a) carried out a series of experiments for the exchange flow over an isolated dune at the CITEEC Laboratory at the University of A Coruña, Spain. The water depth was 12 cm and the Reynolds number was 13500.

The velocity and density fields were simultaneously measured by means of the Particle Image Velocimetry (PIV) and Laser Induced Fluorescence (LIF) techniques. The flow area of interest was about 0.30 x 0.24 m, and the spatial resolution was 1.7 mm. Details of the filters and quality of the images are shown in Figure 3.3. The sampling frequency was set to 10 Hz. Further details of the experimental setup can be found in Anta el al. [2011a, 2011b]. The results of their experiments were used in this study to verify the numerical simulation.

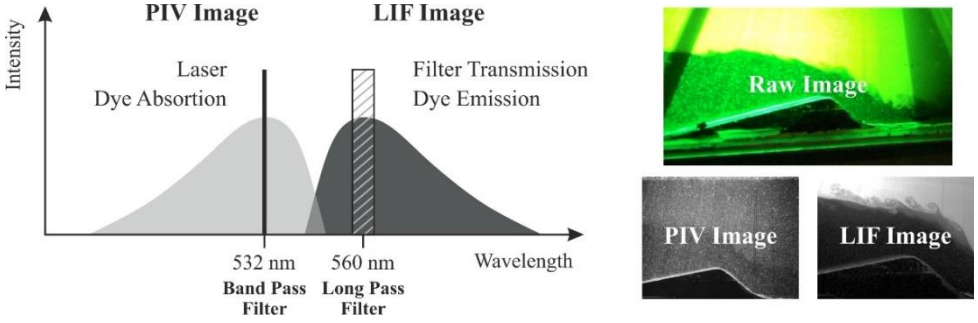


Figure 3-3 (a) Using different filters for PIV and LIF cameras; (b) PIV, LIF and raw images of the experiment

## 3.4.Results and discussion

In this section, the results of the numerical simulation with LES and the experimentally-collected data are compared, including shear interfacial instabilities, net discharge flow, velocity profiles, density profiles, shear layer position and thickness, Bulk Richardson number, and entrainment rate. The results from the numerical simulations are validated with the measured data from the experiments conducted by the authors, once the maximal exchange rate between the two fluids was achieved. This situation occurred at the instance between 150 s and 450 s after the initiation of test. During the maximal exchange rate, flow discharges were almost constant, although

periodic fluctuations due to baroclinic and barotropic waves and instabilities were also observed. The results of the numerical simulation with the RANS model is also presented for shear layer thickness, Bulk Richardson number, and entrainment rates, to be compared with the LES approach.

### 3.4.1. Mean flow velocity and density

This section introduces the visualization of the flow fields over the dune. Figure 3.4 shows the measured and simulated mean velocity fields by LES, with Figure 3.4 (b) showing the LES numerical results for the prediction of the mean velocity distribution contours on the longitudinal (x-z) planes of the dune. As seen from the mean flow distribution, when the flow reaches the dune's summit, it accelerates and continues downstream.

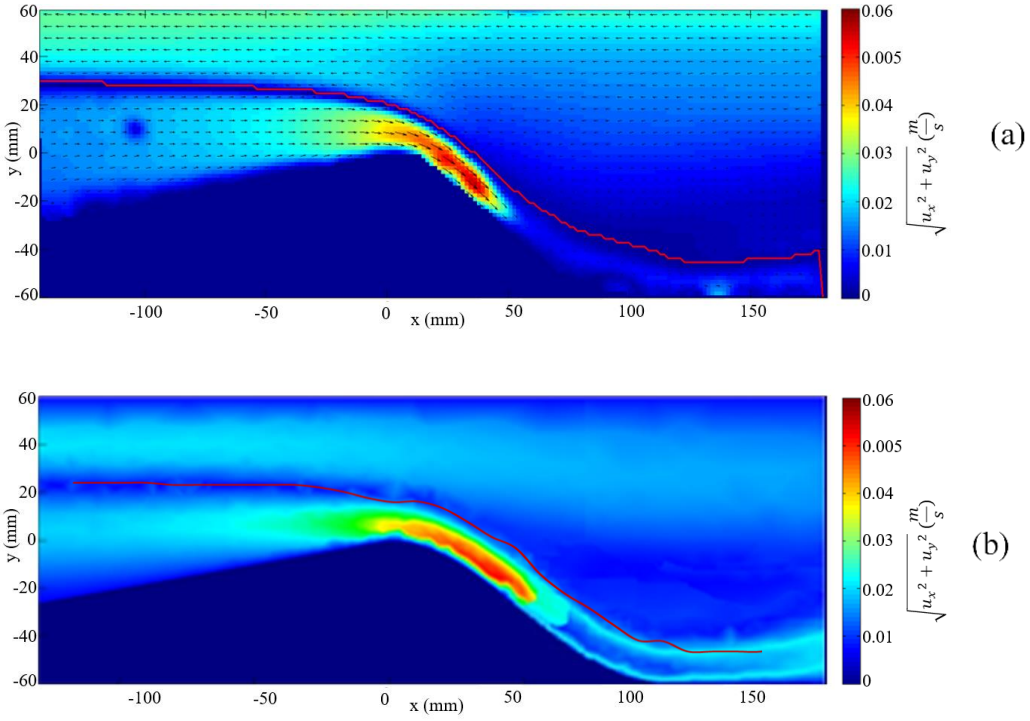


Figure 3-4 Time-averaged mean velocity profile of the flow over the dune: (a) experimental results; (b) LES numerical model prediction (red line is the shear layer position)

The observed vs. predicted velocity values and the regression equations are also plotted in Figure 3.5. The domain is divided into three zones, and for each zone, the $R^2$ and RMSE (Root-mean-square error) is calculated.

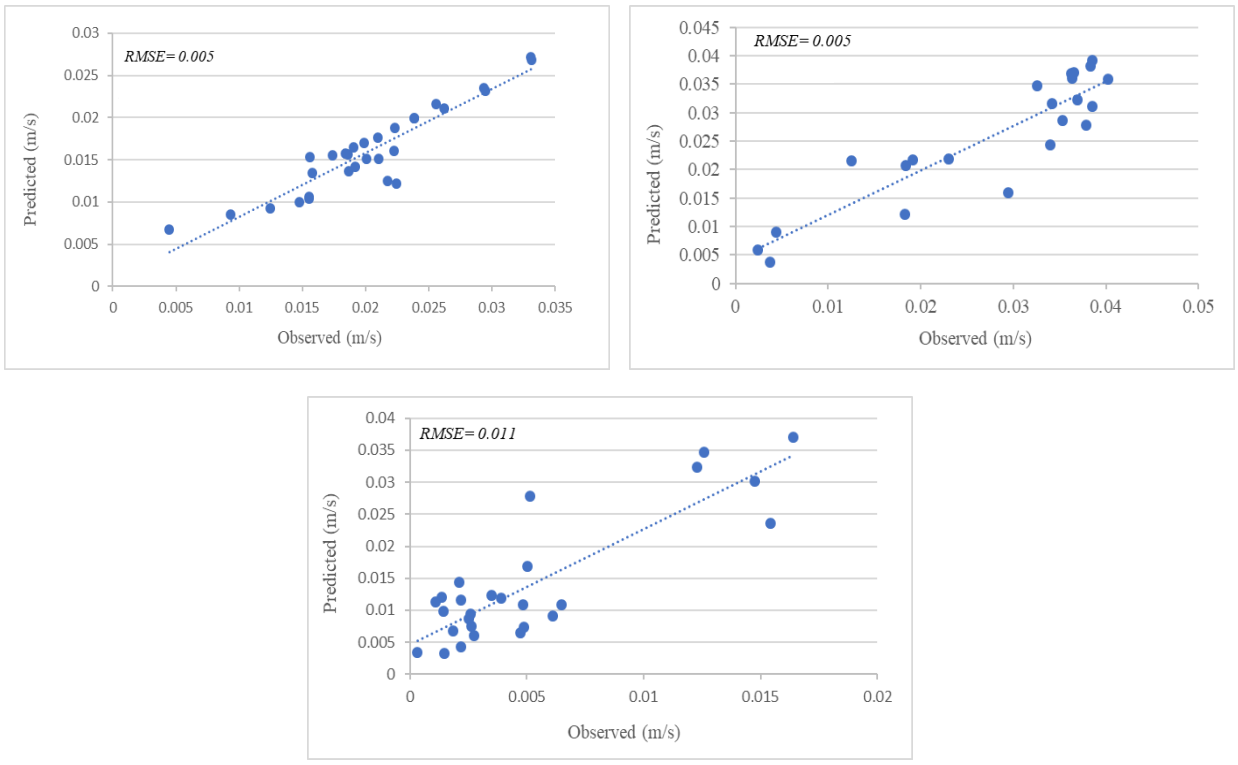


Figure 3-5 LES predicted vs. observed values of the velocity for three different flow regions: (a) for -100<x<0 mm; (b) for 0<x<50 mm; and (c) for 50<x<100 mm

The first and second regions are for -100<x<0 mm and 0<x<50 mm, from -100 mm up to the dune crest and from the dune crest to the location where the KH instabilities start to generate. As shown in Figure 3.5, the RMSE values for these two zones are equal to 0.005 m/s, which shows that the differences between the observed values and the model's predicted ones are small. However, for 50<x<100 mm, the RMSE value increased to 0.011 m/s. This increase in RMSE value is due to the formation and growth of hydrodynamic instabilities at the interface between the two fluids, which leads to the entrainment and mixing in such flows.

Later, it will be shown that in the range 50<x<100 mm, instabilities start to occur and grow, and the measured and modeled values are subjected to fluctuations related to the instabilities. Since this is the most unstable region, more differences are observed in this area between the observed and modeled values. In the following sections, other parameters, including shear layer thickness, Bulk Richardson number, and entrainment rate, are discussed to study these instabilities in more depth.

Downstream of the sill crest, the position of the shear interface indicates the adaptation of the two-layer flows to the dune's shape, as shown in Figure 3.6. The velocity shear interface is defined as

the depth at which the velocity changes direction. The measured and LES modeled results are in good agreement, and the model predictions show a difference with a root-mean-square error (RMSE) of 2.9 mm.

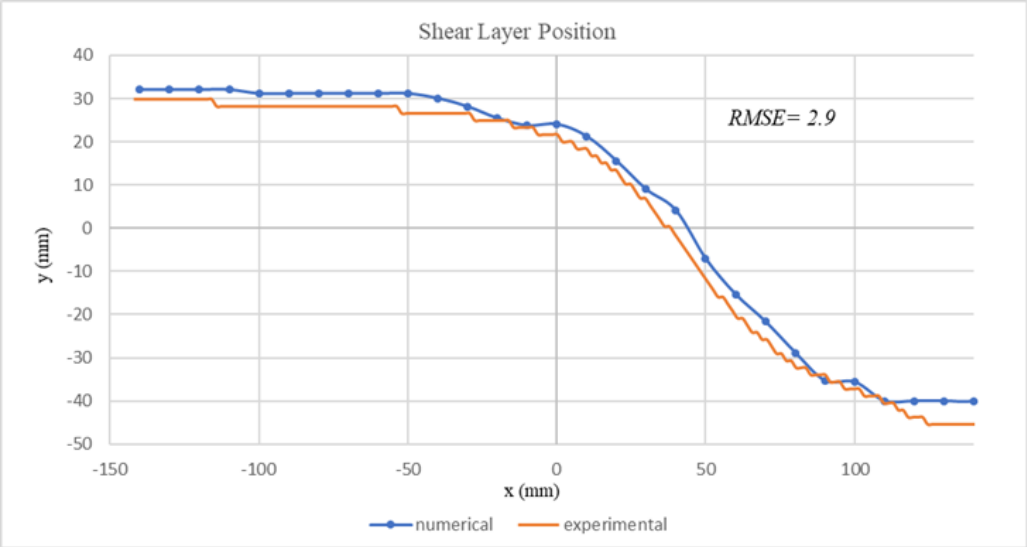


Figure 3-6 Comparison of the LES modelled and measured velocity shear interface positions

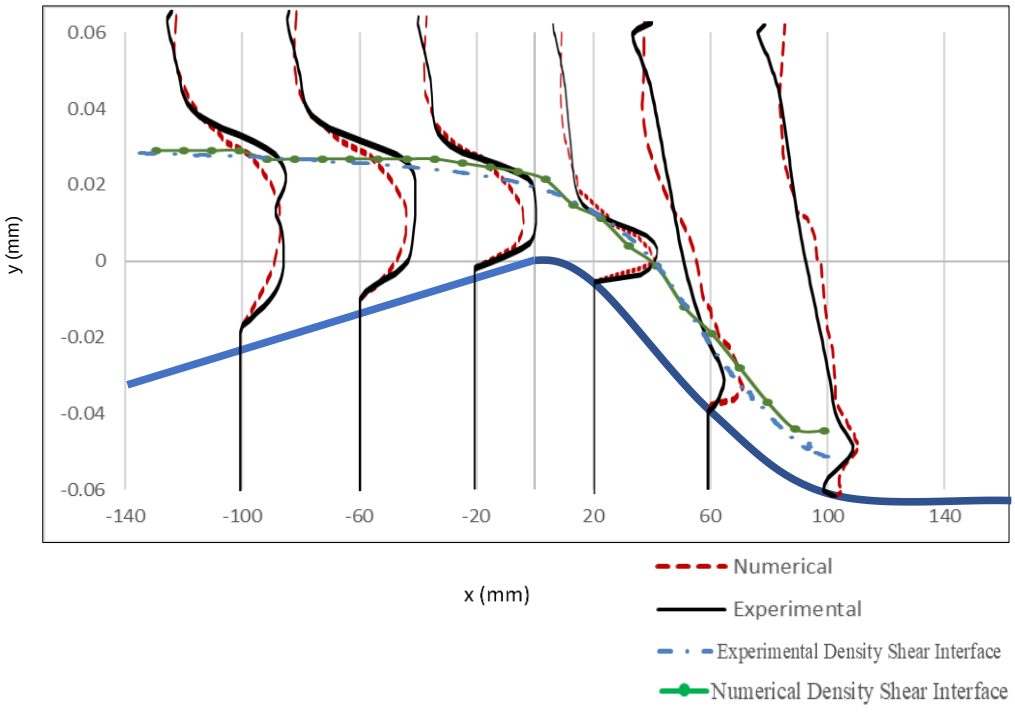


Figure 3-7 Comparison of the LES modelled and measured vertical velocity profiles

The averages of the velocity profiles over the maximal exchange period as well as the density shear interface are plotted in Figure 3.7. The density shear position, $h_{\rho}$, is the depth at which the density profile covers the averaged value between 30% and 70% of the maximum density of each profile, i.e., $h_{\rho}$ = abs ($h_{\rho=0.3}$- $h_{\rho=0.7}$)/2. It was observed that the interface position occurs below the zero-velocity position. This phenomenon was also observed by Morin et al. (2004) and is due to the energy dissipation caused by the enhanced flow entrainment from the upper to the lower layer.

### 3.4.2. Shear interfacial instabilities

Drawing energy from the flow results in the formation of instabilities, which then lose the energy due to the turbulent dissipation and mixing of the stable density gradient. These structures are called shear instabilities. Studies have shown that a shear instability in a stratified fluid is likely to happen when the Richardson number drops below a certain critical value, and the flow may become unstable (Miles,1961).

One of the main objectives of this study is related to the capability of the model to reproduce interfacial shear instabilities such as Kelvin-Helmholtz (KH) or barotropic seiches. When small perturbations draw kinetic energy from the flow in the case of parallel shear flows, these instabilities occur.

Negretti et al. (2007) reported barotropic oscillations while investigating interfacial waves in two-layer exchange flows, and their experiments demonstrated that a baroclinic exchange flow is dominated by barotropic forcing-induced oscillations. These periodic barotropic fluctuations have also been measured and reported in this study.

The flow development at the interface during the maximal exchange period is presented in Figure 3.8 in a series of images. The interface images were captured at a rate of 5 Hz in order to track the temporal development as the waves travelled down the slope. As the lower layer began to accelerate down the sill, the large-scale KH instabilities also started to grow. These large-scale interfacial waves were generated within 50 <x<100 mm. The locations at which the instabilities were about to form were determined from the interface images. As is shown in Figure 3.8, in both the LES numerical and experimental results, the waves became larger in amplitude as they travelled along the interface and reach their maximum size and distortion in shape at the end of

the slope. This pattern was also observed by Fouli and Zhu (2011). Figure 3.8 also shows that RANS was not capable of reproducing instabilities.

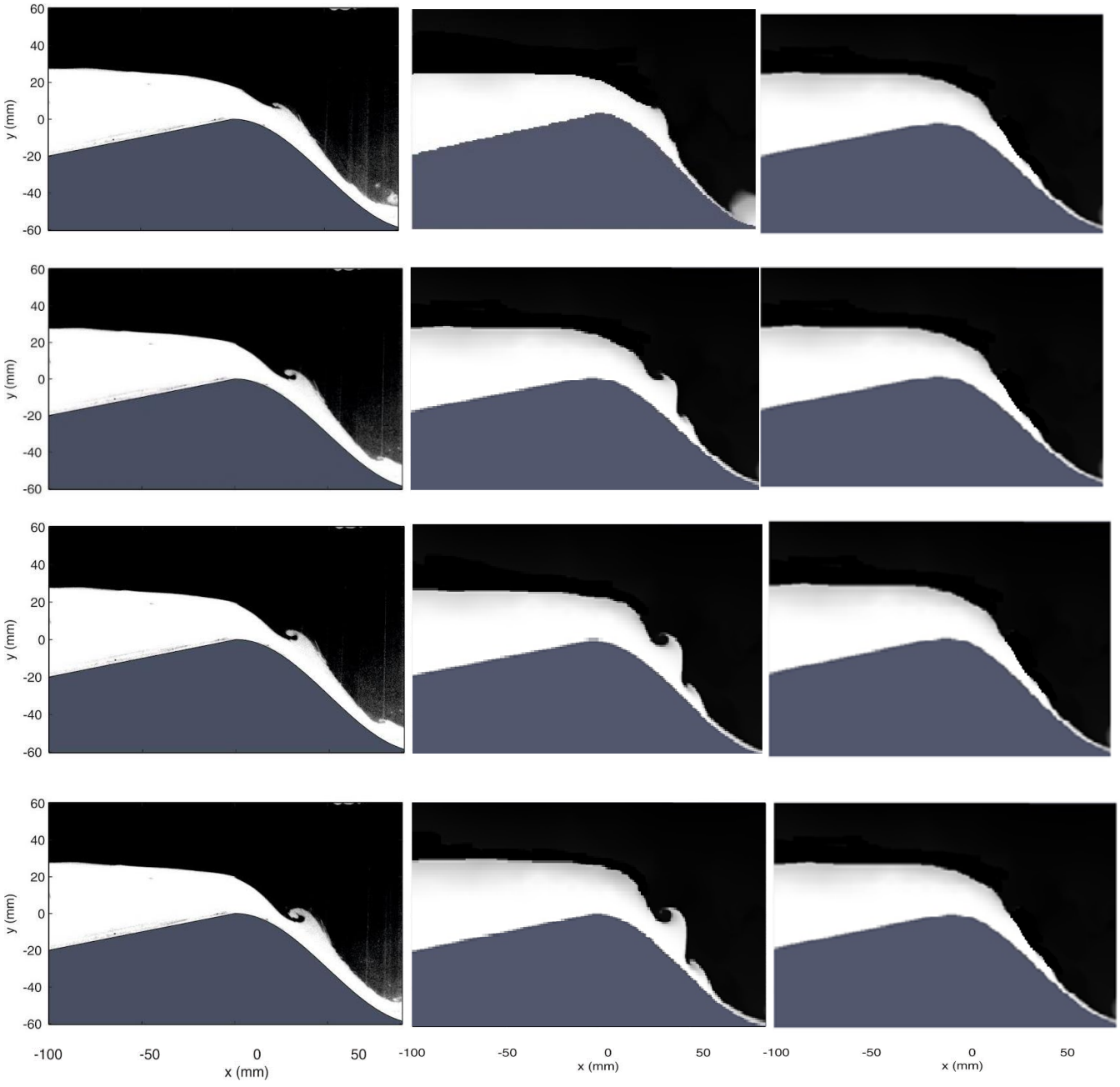

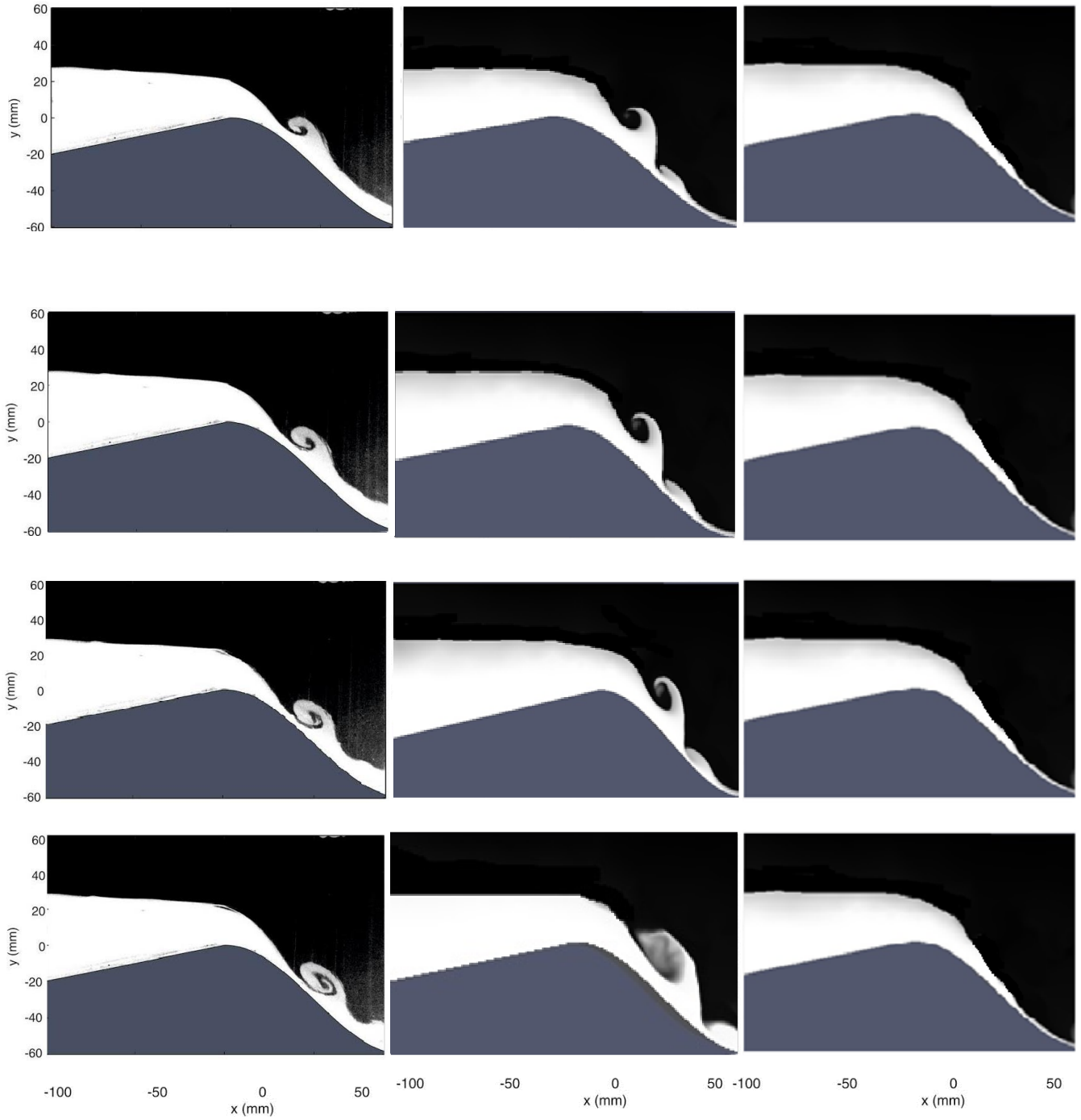


Figure 3-8 Series of instantaneous images of the: (a) measured and (b) LES modeled (c) RANS modeled two-layer flows. The time lag between the images is 0.1 s.

Figure 3.9 shows that the variation in flow rate along the x-coordinate was normalized by the net flow rate over the dune crest, i.e., ( $q_{net} / H\sqrt{g'H}$ , H = 0.12 m, g'= 0.0585 m/s$^2$). A flow is termed a pure baroclinic exchange flow when the net flow across a vertical plane is zero. Based on Negretti et al. (2007), an unsteady barotropic flow component exists with the baroclinic two-layer exchange. This additional component is generated by the differences in the initial hydrostatic pressures against the barrier separating the fluids at the start of the experiment. The initial unbalanced pressure, which is an impulsive barotropic force, produces oscillations of the net flow and of the free surface.

In this study, in both the numerical and the experimental graphs, the net flow rate oscillates around zero, with periodic dampening water oscillations around this value. The oscillations decrease in amplitude over time because of frictional losses.

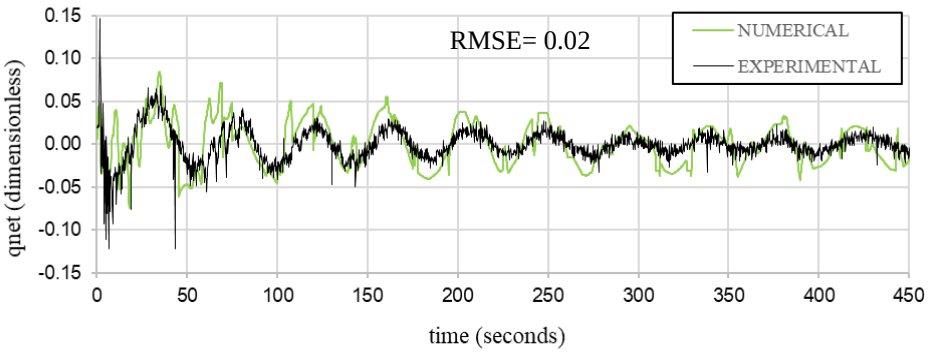


Figure 3-9 Normalized net flow at the dune crest

As is shown in Figure 3.9, in the LES numerical model and the experimental tests, the values of *qnet* are slightly different in amplitude with an RMSE equal to 0.02; the forcing mechanisms of the interface instability generation have the same periods, of 56.25 seconds, which is calculated from spectral analysis of the net flow.

### 3.4.3. Shear layer thickness and Bulk Richardson number

Morin et al.'s (2004) approach is used to define the shear layer thickness, $= \Delta U/(du/dx)_{max}$ , which can be obtained from the vertical variation of the velocity at different points along the *x*-direction. Figure 3.10 shows the time-averaged (over the maximal exchange period) values of the experimentally and numerically obtained results using LES and RANS for shear velocity thickness, where the thickness of $\delta$ increases downslope of the dune crest as a result of interfacial

mixing. In the LES model, $\delta$ ranged from 0.012 mm at the dune crest to 0.047 mm at the end of the dune, while the experimental values varied between 0.01-0.05 mm for the same locations.

As can be seen, the results predicted by the RANS numerical approach are very similar to those from the LES, up to x=50 mm. The largest values of the shear layer thickness and also the highest difference between the measured and modeled values were observed at the location where the instabilities started to form and grow (50 mm <x< 100 mm), which was the most unstable region. As shown in Figure 3.10, the root-mean-square errors (RMSEs) between the LES and RANS approaches with the experimental results are 0.0065 and 0.011 respectively, which shows that the results predicted by the LES in the unstable region are in better agreement with the experimental results compared to those of the RANS method. This proves the ability of the LES method in modeling small-scale turbulent features of a flow field.

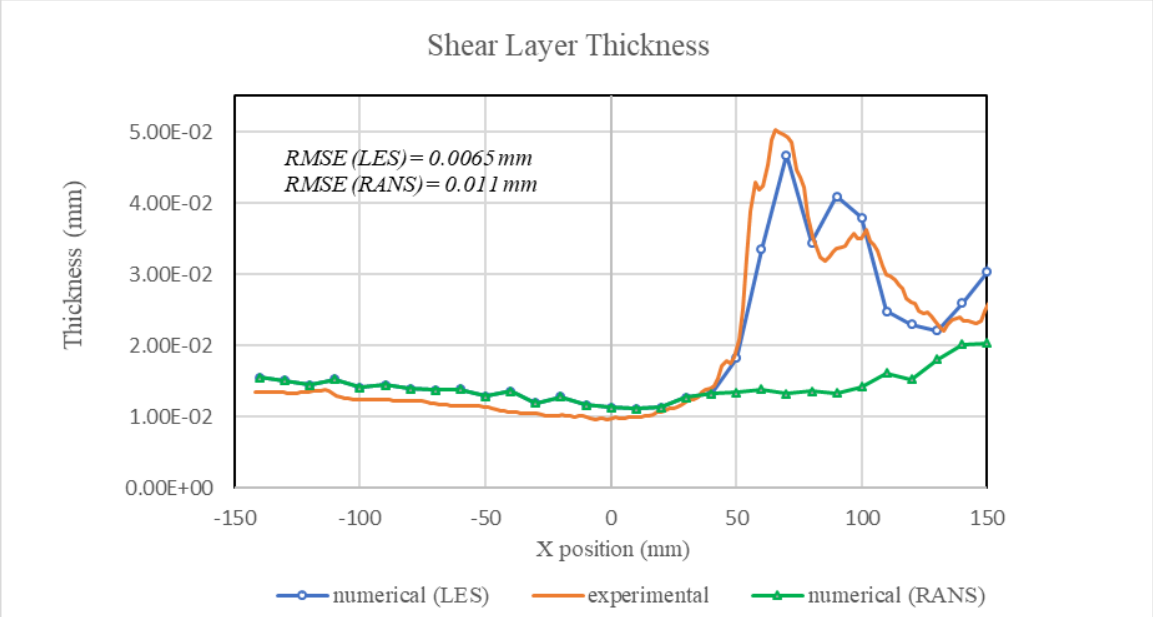


Figure 3-10 Time-averaged thickness of the shear layer obtained from the numerical model results and data measured from experimental tests

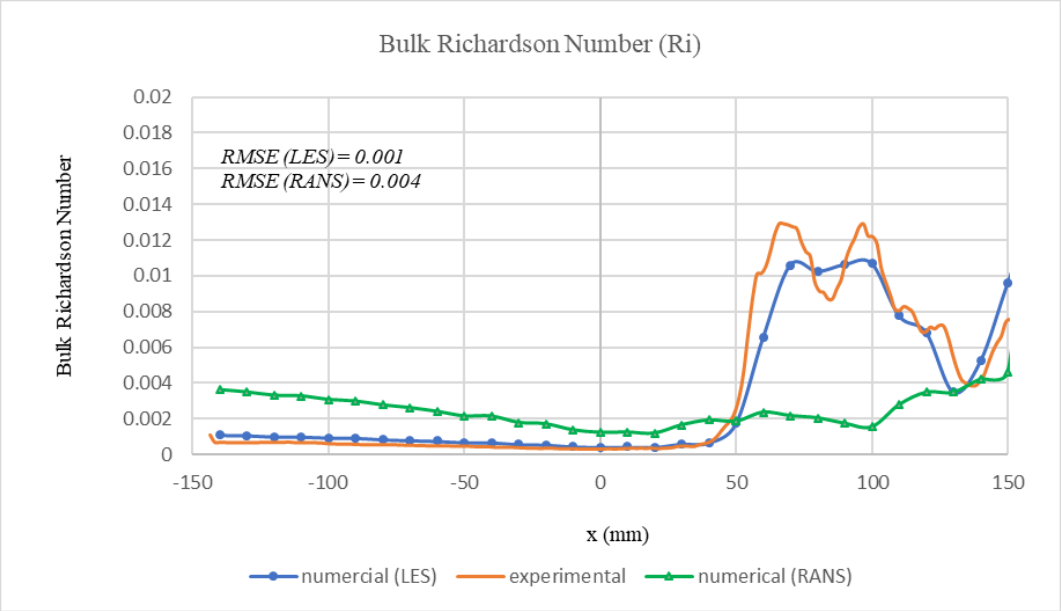


Figure 3-11 Time-averaged Bulk Richardson number obtained from the numerical model results and data measured from experimental tests

Figure 3.11 presents a comparison of the experimental and simulated Bulk Richardson values along the dune, defined as:

$$Ri = g'\delta/\Delta U^2 \tag{3.12}$$

Numerical simulation values of the Bulk Richardson number generated by the LES method range between 0.001 and 0.011. These values are in good agreement with the Ri obtained from the experimental tests, which were between 0.0009 and 0.013 with an RMSE equal to 0.001. In both the LES and experimental results, the Bulk Richardson number showed an increasing trend for $x$>50. The maximum values were obtained downstream of the dune crest, where KH instabilities developed. For this area, the numerical values from the LES method showed a 12% difference from the measured values.

However, as can be seen in Figure 3.11, the RANS method was not able to capture these instabilities, and therefore the results from the RANS method, with an RMSE equal to 0.004, have less agreement with the experimental results, especially for the less stable locations.

### 3.4.4. Entrainment rate

Entrainment rate is another common parameter used to describe the flow exchange between layers, and is defined as (Ellison and Turner 1959):

$$\alpha_e = \frac{1}{V} dq/dx \tag{3.13}$$

where $q$ is the flow rate per unit width in the layer of interest, $V$ is a characteristic velocity of the layer ($V = \int u^2 dz / \int u dz$), and $u$ is the horizontal velocity distribution.

The entrainment coefficients are plotted in Figure 3.12, and show good agreement between the experimental and LES numerical values. In both the numerical and experimental results, the entrainment rate is very small upstream of the crest of the dune, as the internal seiche does not produce flow entrainment. The obtained entrainment rates show that the amount of flow exchanged between the two layers is significantly higher downstream and reaches a maximum of 0.58 and 0.39 respectively for the experimental results and those from the LES values. However, while the RANS those provides good results upstream of the dune, it is not a reliable model approach at locations where significant KH wave activity can be observed. The RMSE is equal to 0.034 and 0.186 for the LES and RANS methods respectively, which demonstrates the advantage of choosing LES to model more complex flows and geometries, such as in this case.

The average difference between the LES results and the experimental values in the area with instabilities (50<x<100) is 20.5%. Then, after instabilities are generated and transported downstream, the flow entrainments start to decrease.

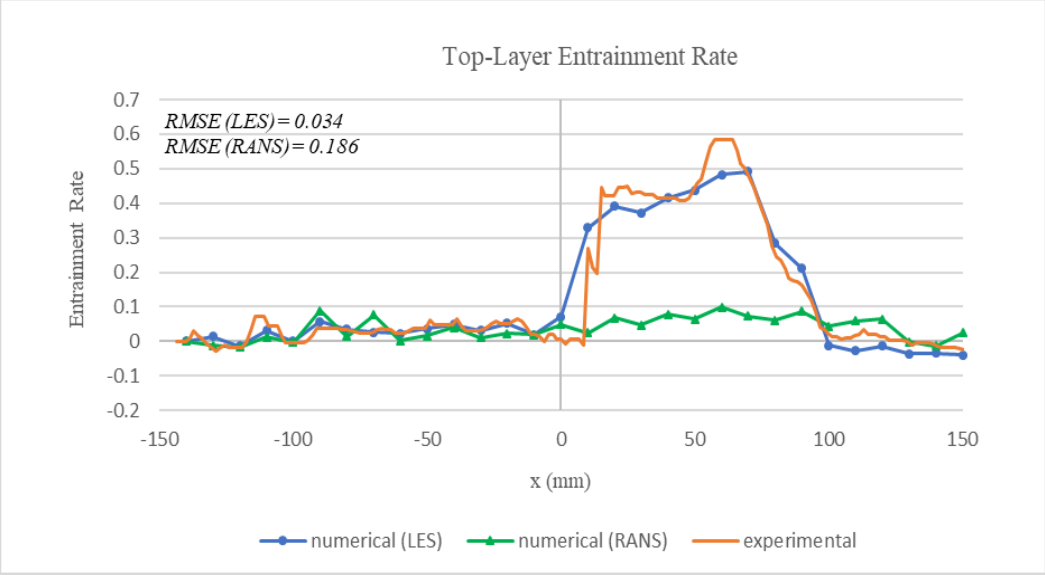


Figure 3-12 Time-averaged entrainment rates obtained from the numerical model results and the experimental tests

### 3.5. Conclusions

In the present study, the mixing process of the two-layer flow over a dune was numerically simulated using the LES method with the Smagorinsky SGS model. The simulation results were compared with the experimental measurements performed by Anta et al. (2011a and 2011b) using PIV-LIF techniques at the University of A Coruna, Spain. Moreover, in order to prove the necessity of using the LES method to model KH instabilities, a RANS simulation was performed and its results were presented. The comparisons covered the velocity distribution, shear layer thickness, Bulk Richardson number, and entrainment rate.

In summary, it has been shown that the RANS approach is able to reproduce good results up to the points where instabilities start to form. However, the RANS method was not able to distinguish between periodic large-scale and turbulent chaotic small-scale features of the flow field considered. This leads to problems when the flow field is governed by both of these phenomena, such as in the present case. Essentially, the RANS approach was not able to reasonably reproduce the unsteady characteristics of the flow field, resulting in an inadequate description of turbulent chaotic unsteady small-scale phenomena between $50<x<100$, where the flow was shown to behave differently with respect to the interfacial wave activity.

The LES method, on the other hand, operates with unsteady fields of physical values, and unlike the RANS approach, spatial filtering is applied. Therefore, compared to the RANS method, the LES predictions showed good agreement with the experimental measurements, as the LES model was able to capture the KH instabilities.

Values for shear layer thickness, Bulk Richardson number, and entrainment rate were calculated and presented in order to better investigate flow instabilities. For shear layer thickness, the RMSEs for the measured and modeled values were 0.0065 and 0.011 in the LES and RANS methods respectively, while similar patterns were observed for the Bulk Richardson numbers and entrainment rates, with a lower RMSE for the results in the LES predictions.

Analysis of the net flow on top of the dune also showed that with the mesh sizes used, the forcing mechanisms of interface instability generation have the same periods, while the amplitudes of the net $q$ values are slightly different, with higher values in the LES model.

# 4. Experimental Study on the Effects of Waves on Mixing Processes[3]


## Abstract

This paper presents the results of an experimental program, on inclined negatively buoyant jets released in a receiving water body in the presence of only waves, as well as with superposed waves and current conditions. The measurements were performed using a combination of Particle Image Velocimetry (PIV) and Laser Induced Fluorescence (LIF) techniques, to measure the time-histories of the velocity and concentration fields. The wave and current characteristics were chosen to simulate a typical effluent discharge into the coastal waters of the Spanish Mediterranean Sea. The same experiments were also performed in a stagnant water body to compare the results with the ones conducted with waves and wave-current conditions. Analyzing the jet behaviour, the influence of the wave motion on the inclined negatively buoyant jet geometry resulted in the jet rotation and increase in the jet width. This can lead to a decrease of the maximum height and a higher dilution under wave conditions. The empirical formulas proposed in this study will provide novel insights into the design of outfalls in coastal waters.



*Keywords*: Wave effect, Inclined negatively buoyant jet, PIV-LIF technique, Wave-Current ambient


## 4.1. Introduction

Submarine outfall discharges from industrial processes or municipal wastewater treatment plants are categorized, based on their density, into two major types. One type is characterized by an effluent which has a density lower than that of the ambient water body and is hence defined as a (positively) buoyant jet that causes the effluent to rise. The second type showcases an effluent with a density higher than that of the ambient water body. In this later case, the discharged effluent tends to eventually sink as a negatively buoyant jet. Negatively/positively buoyant jets exist or occur in various civil and environmental engineering projects: outflows of desalination plants,

[3] Sepideh Khorshid, Abdolmajid Mohammadian, Ioan Nistor "Experimental Study on the Effects of Waves on Mixing Processes", **Canadian Journal of Civil Engineering**, Under Review.

discharges of cooling water from nuclear power plants, mixing chambers, etc. Inclined Negatively Buoyant Jets (INBJs), are the focus of this study, and are negatively buoyant jets released at an angle between 0° and 90° to the horizon. Exclusive examples of such phenomenon are in brine discharges from desalination plants, dense effluents from wastewater treatment plants, etc. These types of jests have been studied during the last decades by several researchers, including Zeitoun et al., (1970), Roberts and Tom, (1987), Oliver et al., (2013), Lai and Lee (2012), Kheirkhah et al., (2015), etc.

Another important influencer of the jet behavior is the state of the fluid it is discharged into. When the jet is discharged into a stagnant water body, the initial dilution of the jet is primarily controlled by the shear entrainment which is induced by the jet's initial momentum and/or the buoyancy forces. However, when the jet is discharged into coastal waters, due to the presence of waves and currents, more complex mixing processes can occur and significantly affect the jet dilution processes. Since this case is happening in most coastal regions, it is necessary to understand the initial dilution under such conditions in order to have a more accurate assessment of their environmental impact on the surrounding waters.

Chin (1987) experimentally studied the effects of waves on a turbulent round jet characteristic and noticed that in such conditions, the dilution of the jet was significantly higher than that of the one occurring in a stagnant ambient. Chyan and Hwung (1993) investigated the flow field of a momentum jet into a wave environment to study physical mechanisms that increase the dilution rate. Their measurements showed dramatic variations not only in the longitudinal distribution of the mean jet axis, but also in the cross-sectional profiles. Koole and Swan (1994) studied the dispersion of a non-buoyant jet beneath a series of progressive gravity waves and showed that the zone of flow establishment is shorter in the presence of waves, and that the rate of entrainment increased in wave-induced mixing conditions. Tam and Li (2008) carried out an experimental study of a vertical jet discharged under random waves and showed that in the presence of waves, the centerline of the jet velocity shows a rapid decrease, while the waves enhance the jet's width and turbulence. When the jet is affected by waves, its mean kinetic energy decreases, while its turbulent kinetic energy and dilution capacity increase.

Several experimental or numerical studies have been carried out to investigate the jet behavior under stagnant, current-only or under wave-only environments. Only few studies on the jet dilution

in coexisting wave and current conditions (wave-current), which is the motivation of the current work, have been performed. Abdel-Rahman and Eleshaky (2003) performed a series of experiments on the behavior of a plane jet vertically discharged in downward direction into a flume under combined waves and current. However, they were unable to measure the concentration field; as such, without recording the effects of waves on the jet initial dilution, it was shown that the oscillatory motion associated with the wave had a noticeable effect on both the mean and turbulent velocity fields.

Wang et al (2015) conducted a series of physical experiments on the initial dilution of a vertical non-buoyant round jet in the wave-current environment. Using a camcorder and a peristaltic suction pumping system, they were able to record the dilution processes and concentration fields. They proved that the jet width in the co-existing of wave and current environment increases more significantly than that does in the current only environment. They also suggested some empirical formulas to generalize the experiment findings.

While the above-mentioned experimental measurements mostly focused on the effect of waves on the flow characteristics of non-buoyant jets, only in few cases buoyant jets were studied and, therefore, the effects of surface waves on buoyant plumes are less understood. One of the studies that has been carried out on the wave effects on positively buoyant plume, is the study by Shuto (1974). Using point measuring technique (samples were taken near the water surface and their salinity and concentration of chromium were measured), Shuto only investigated the surface dilution. Sharp et al. (2014) also studied effect of surface waves on a positively buoyant plume discharging from multiport diffuser and concentration was measured using a Laser Induced Fluorescence (LIF) technique. The average increase in dilution of the plume due to wave effects was found to be similar to the increase in surface dilution previously reported by other researchers. The greatest increase in dilution was found to be in the region near to the diffuser and before individual plumes had merged. Another study was carried out by Ferrari and Querzoli (2015) on the effects of waves with different characteristics on negatively buoyant jets using LIF technique. Analyzing the global phenomena, it was shown that the INBJs preserve their identity close to the origin, whilst further from their origin, they are split into two separate branches that, eventually, fuse together before sinking to the bottom

To the best knowledge of the authors, the effect of waves on negatively buoyant plume and also in wave-current ambient environment has not been investigated before using both LIF and PIV

techniques. In order to quantitatively investigate the effect of the wave on the initial dilution of the jet discharge, the authors carried out a series of experiments on inclined negatively buoyant jets in a wavy environment and wave-current environment. Also, for comparison, a series of experiments were carried out on the jet in the stagnant water and current-only conditions. The use of Particle Image Velocimetry (PIV) and Laser Induced Fluorescence (LIF) techniques, allowed to not only investigate the velocity fields, but also accurately investigate the diluting effect of surface waves on buoyant plumes. The investigation led to development of novel empirical formulae that can be used for design of outfalls of negatively buoyant jets in wave-current environment.

This manuscript is organized as follows: Section 2 describes the experimental plan and methodology, as well as the discharge properties and wave parameters. In Section 3, the experimental results, including the jet developments and trajectories, terminal rise heights, centerline peaks, mean concentration fields of the jets, and minimum dilution at centerline peaks are presented and discussed. Additionally, based on the dimensional analysis, and based on the analyzed experimental data, several empirical formulae are derived. Finally, the conclusions of this study are presented.

### 4.2. Experiments plan and methodology

The physical experiments were carried out in a wave-current flume in CITEEC-UDC, the Water and Environmental Engineering Group (GEAMA) at the University of Coruña, Spain. The sketch of experimental setup is shown in Figure 4.1. The wave-current flume has dimensions of 20 m long, 0.6 m wide, and 0.8 m deep. A computer-controlled wave maker is located at one end of the flume, and an artificial slope (beach) is located at the other end with the purpose to absorb and dissipate the incident wave energy. Wave probes were used to measure the amplitude, or height, of the passing waves. The standard calibration procedures used for tuning a wave generation system are based upon empirically determining the wavemaker response function, specifically the characteristic of the generated waves as a function of input frequency and amplitude. Calibrations were carried out for regular unidirectional waves. The calibration was performed using three gauges inside the water.

The jet is discharged rightwards, the same direction as the wave propagation. The jet generation system consists of a 50 L storage tank, a peristaltic pump which fills a constant head tank placed

2 m above the jet nozzle level. An ultrasonic flowmeter and set of valves are used to monitor the discharge of the round jet nozzle. By adjusting the valve, jets with different initial velocities could be generated. The jet nozzle, with a diameter of 3 mm, was located 10 cm vertically above simulated sea bottom. An elevated perspex platform of 12 m and 0.5 m wide was installed 5 cm above the flume floor to simulate the sea bed. This configuration avoids the reflection of the brine plume with the flume walls.

As previously mentioned, Particle Image Velocimetry (PIV) technique and a Laser Induced Fluorescence (LIF) technique were used to investigate the velocity and concentration fields, and the diluting effect of surface waves on buoyant plumes. The effluent was seeded with 50 mm polyamide seeding particles and Rhodamine 6G fluorescent dye. The relative density between the effluent and the ambient water was 2.136.

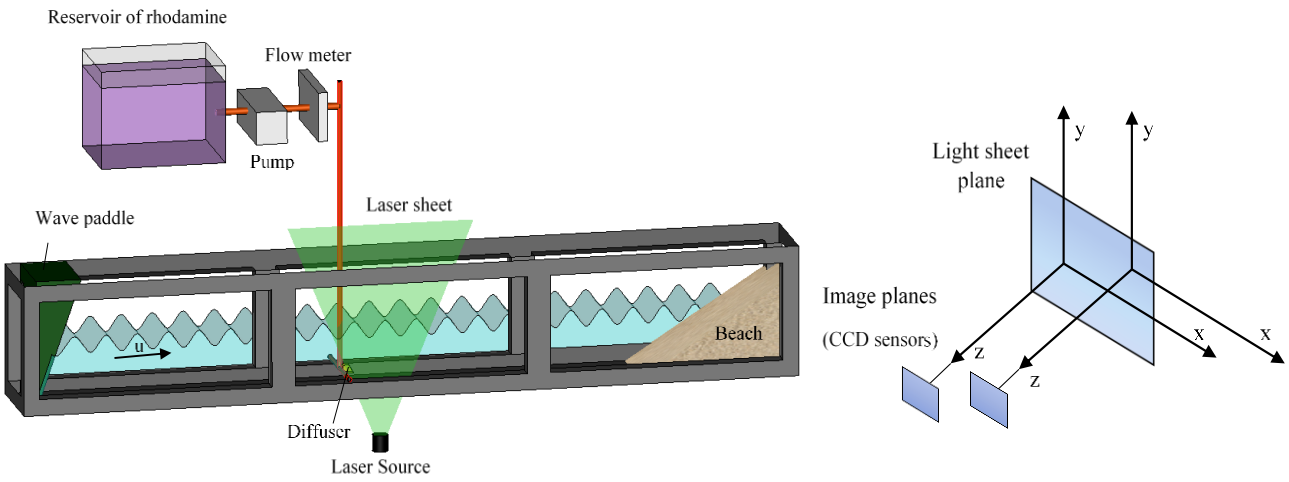


*Figure 4-1*. Experimental set up for PIV-LIF study of buoyant plume under the combined effects of waves and current

The laser set up used for this experiment is shown in Figure 4.1. The laser source is placed below the tank, to avoid reflection when waves are generated during the experiment. In these experiments, two CCD cameras and two independent coordinate systems are used in front of the light sheet and the target plane is parallel to the image plane as shown in Figure 4.1. The laser source produces 532-nm light at 5 Hz, which is recorded by PIV camera. Rhodamine 6G dye light has a 560 nm wave-length and was recorded with the LIF camera equipped with an appropriate

high-pass filter. The field of view in the experiments was 200 mm x 400 mm. All steps for PIV calibration including defining coordinate system, grid reconstruction and Calculation of the mapping function were carried out. The intensity of light emitted from a dyed region of flow is proportional to the intensity of excitation energy and to the concentration of dye. If the excitation energy is locally uniform, then the emitted light intensity will be linearly related to the dye concentration. Then, with a simple calibration, the emitted light intensity can be directly converted to dye concentration. For this purpose, a calibration tank is used with a dark uniform background. Then different Rhodamine concentrations were injected to the tank with water and the intensity was recorded by Davis software. Subsequently, a graph is generated to use for post processing the data.

This whole system has been successfully applied in previous near and far field desalination brine spills without waves (Costa 2016), hipodense spills (Mera, 2010) and stratified flows (Anta et al. 2016).

### 4.2.1. Discharge properties

The behavior of a discharge emerging from a diffuser can be classified using two dimensionless flow characteristics: the Reynolds and the Froude numbers. In order for the flow to be fully turbulent, as it normally occurs in the case of a real diffuser, and be also independent from initial condition, the Reynolds number for the discharge should be greater than 4000 (Isaacson et al., 1983). Moreover, the Froude number, which is defined as the ratio between the inertia and buoyant forces and determines how soon the discharge evolves from a jet to a plume, was chosen to be 34 which was achievable in the adopted experimental set up.

Inclined negatively buoyant jet, which is a mixture of water, salt (to increase the jet's density), and rhodamine (for visualization by laser), was released into the ambient water body in the flume with 35 cm water level at two angles of 45 and 60 degrees.

### 4.2.2. Wave parameters

Wave parameters were chosen to simulate some scaled-down typical Mediterranean wave conditions, with respect to the kinematic similarity. Thus, the first step was to define the geometrical scale of the model, $k_L$, as:

$$k_L = \frac{1}{40} \tag{4.1}$$

Then, based on similitude relationships, one obtains

$$A_{Model} = A_{protype} \sqrt{k_L} \tag{4.2}$$

$$T_{Model} = T_{protype} \, . \, k_L \tag{4.3}$$

where *T* is the wave period, *A* is the wave amplitude, *N* is the number of waves and *L* is the wave length.

The field wave data used in this modelling exercise were obtained from the wave buoy located off Cabo de Palos (Lat: 37.654 N, Long: -0.638 E) placed in the water with the depth of 65 m (offshore the Port of Alicante), recorded by the Oceanographic Data Bank- Spanish Port Authority- between 1985 and 2012. The ratio of the water depth d to the wave length L was in the intermediate-depth water regime (d/L = 0.25, 0.18, and 0.14). The periods chosen were also the most probable wave periods for medium regime according to the Oceanographic Data Bank, Ports of Spain, for the wave buoy of Cabo de Palos, Alicante.

Moreover, in order to allow for a comparison with the same jets released in wave-current environment, each test was also performed with stagnant water case. The parameters of the experimental program are shown in Table 4.1.

**Table 4-1.** Parameters of the experimental program

| Exp. no. | | Jet angle Θ | Δρ/ρ0 % | Discharge velocity U0 (m/s) | Water depth h (m) | Ambient water body velocity Ur (m/s) | Wave height H (cm) | Wave period T (s) |
|---|---|---|---|---|---|---|---|---|
| Stagnant-Environment | S-01 | 45 | 2.136 | 0.85 | 0.35 | 0 | 0 | 0 |
| | S-02 | 60 | 2.136 | 0.85 | 0.35 | 0 | 0 | 0 |
| Wave-Environment | W-01 | 45 | 2.136 | 0.85 | 0.35 | 0 | 1.9 | 0.9 |
| | W-02 | 45 | 2.136 | 0.85 | 0.35 | 0 | 1.9 | 1.1 |
| | W-03 | 45 | 2.136 | 0.85 | 0.35 | 0 | 1.9 | 1.3 |
| | W-04 | 60 | 2.136 | 0.85 | 0.35 | 0 | 1.9 | 0.9 |
| | W-05 | 60 | 2.136 | 0.85 | 0.35 | 0 | 1.9 | 1.1 |
| | W-06 | 60 | 2.136 | 0.85 | 0.35 | 0 | 1.9 | 1.3 |
| Current-Environment | C-01 | 45 | 2.136 | 0.85 | 0.35 | 0.015 | 0 | 0 |
| | C-02 | 45 | 2.136 | 0.85 | 0.35 | 0.03 | 0 | 0 |
| | C-03 | 45 | 2.136 | 0.85 | 0.35 | 0.05 | 0 | 0 |
| | C-04 | 60 | 2.136 | 0.85 | 0.35 | 0.015 | 0 | 0 |
| | C-05 | 60 | 2.136 | 0.85 | 0.35 | 0.03 | 0 | 0 |
| | C-06 | 60 | 2.136 | 0.85 | 0.35 | 0.05 | 0 | 0 |
| Wave & Current Environment | WC-01 | 45 | 2.136 | 0.85 | 0.35 | 0.015 | 1.9 | 0.9 |
| | WC-02 | 45 | 2.136 | 0.85 | 0.35 | 0.015 | 1.9 | 1.1 |
| | WC-03 | 45 | 2.136 | 0.85 | 0.35 | 0.015 | 1.9 | 1.3 |
| | WC-04 | 45 | 2.136 | 0.85 | 0.35 | 0.03 | 1.9 | 0.9 |
| | WC-05 | 45 | 2.136 | 0.85 | 0.35 | 0.03 | 1.9 | 1.1 |
| | WC-06 | 45 | 2.136 | 0.85 | 0.35 | 0.03 | 1.9 | 1.3 |
| | WC-07 | 45 | 2.136 | 0.85 | 0.35 | 0.05 | 1.9 | 0.9 |
| | WC-08 | 45 | 2.136 | 0.85 | 0.35 | 0.05 | 1.9 | 1.1 |
| | WC-09 | 45 | 2.136 | 0.85 | 0.35 | 0.05 | 1.9 | 1.3 |
| | WC-10 | 60 | 2.136 | 0.85 | 0.35 | 0.015 | 1.9 | 0.9 |
| | WC-11 | 60 | 2.136 | 0.85 | 0.35 | 0.015 | 1.9 | 1.1 |
| | WC-12 | 60 | 2.136 | 0.85 | 0.35 | 0.015 | 1.9 | 1.3 |
| | WC-13 | 60 | 2.136 | 0.85 | 0.35 | 0.03 | 1.9 | 0.9 |
| | WC-14 | 60 | 2.136 | 0.85 | 0.35 | 0.03 | 1.9 | 1.1 |
| | WC-15 | 60 | 2.136 | 0.85 | 0.35 | 0.03 | 1.9 | 1.3 |
| | WC-16 | 60 | 2.136 | 0.85 | 0.35 | 0.05 | 1.9 | 0.9 |
| | WC-17 | 60 | 2.136 | 0.85 | 0.35 | 0.05 | 1.9 | 1.1 |
| | WC-18 | 60 | 2.136 | 0.85 | 0.35 | 0.05 | 1.9 | 1.3 |

## 4.3. Results and discussion

### 4.3.1. Jet development

In order to better understand the influence of wave parameters on the jet geometry, the behaviour of an INBJ in a wave environment (W-01) is shown in Figure 4.2. The instantaneous flow pattern can be observed in time series of pictures of the INBJ at different phases of the wave motion. From this figure, three different regions for the jet body, also spotted by Chyan and Hwung and (1993), can be observed in the presence of waves. The first region is where the jet tends to preserve its initial direction and maintain its initial shape and behaviour. In this region, the jet entrainment processes dominate, and the jet has more momentum. As such this region is called the *momentum dominated near field* (MDNF), as described by Rajaratnam and Langat (1995) for cross-flow. In this experiment condition (W-01), the jet is in MDNF from $x=0$ to $x=50$ mm. The next region is termed the *momentum dominated far field* (MDFF) or *transition region*, where the jet centerline is deflected by the wave motion, and which, in this case, could be observed between $x=50$ and $x=200$ *mm.*

As can be seen in Figure 4.2, jet deflection can be directed upward or downward, depending on the wave phase. At the same time, wave motions create a rotation in the trajectory of the INBJ. In this region, due to the interaction with the waves, the jet is further slowed down, until it reaches the region which is called the *passive plume region* (PPR). In this region, the jet is dominated by the ambient fluid motion and the effect of the jet initial momentum becomes negligible.

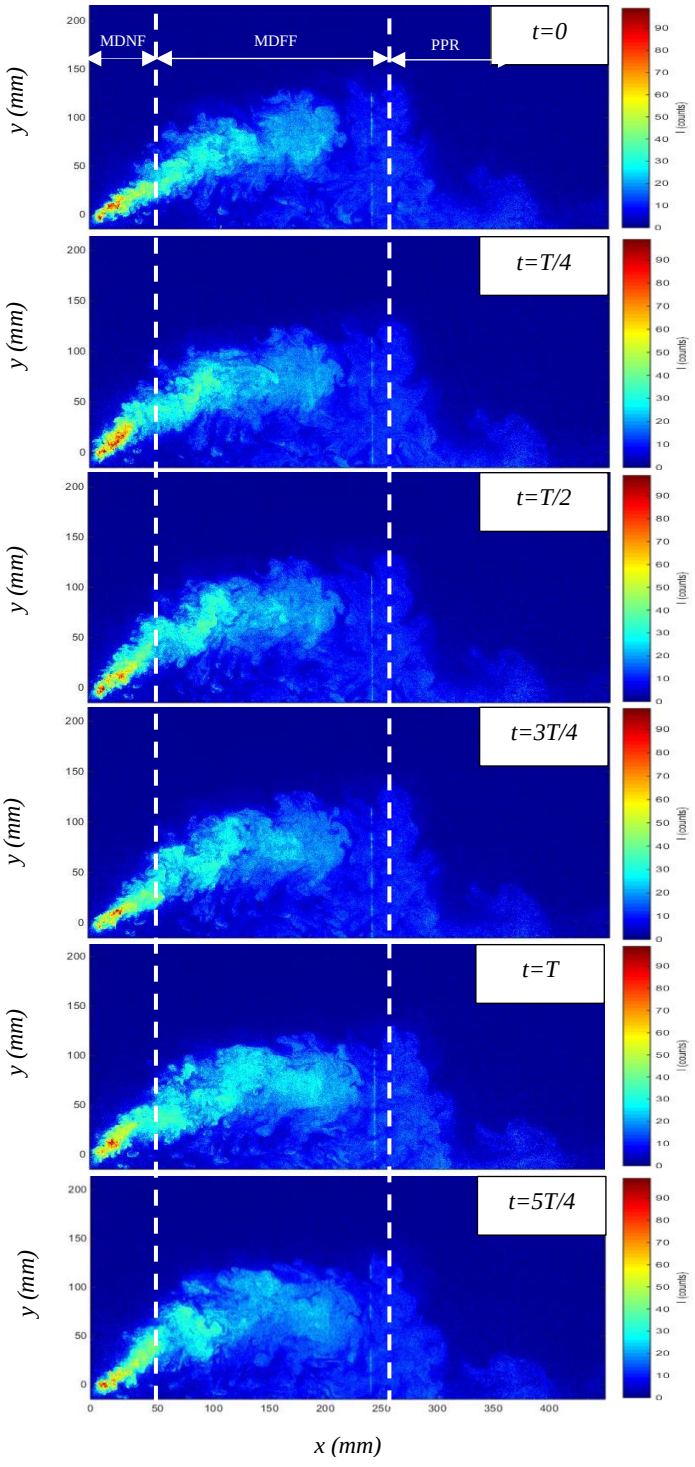


Figure 4-2. LIF images of mean concentration field of an INBJ with Fr=34 released with an angle of 45˚ to the horizontal in receiving environment with wave with T=0.9 (s) and H=1.9 cm

### 4.3.2. Jet axis trajectory and overall flow characteristics

The experimental procedure allowed the simultaneous determination of PIV and LIF fields. Figure 4.3 shows the time-averaged velocity vectors which are put over the concentration contour map, for the test W-01. For most of the tests, full field was captured. However, for current and wave & current tests, only the upstream portions of the discharges were captured due to the initial momentum and long trajectories of the jets. The gray scale bar shows the concentration scale, and a reference vector with a magnitude of the efflux velocity is also provided on Figure 4.3. PIV results were post-processed in the area of the interest, some of the unusual vectors on boundaries are removed and gaps were filled using interpolation.

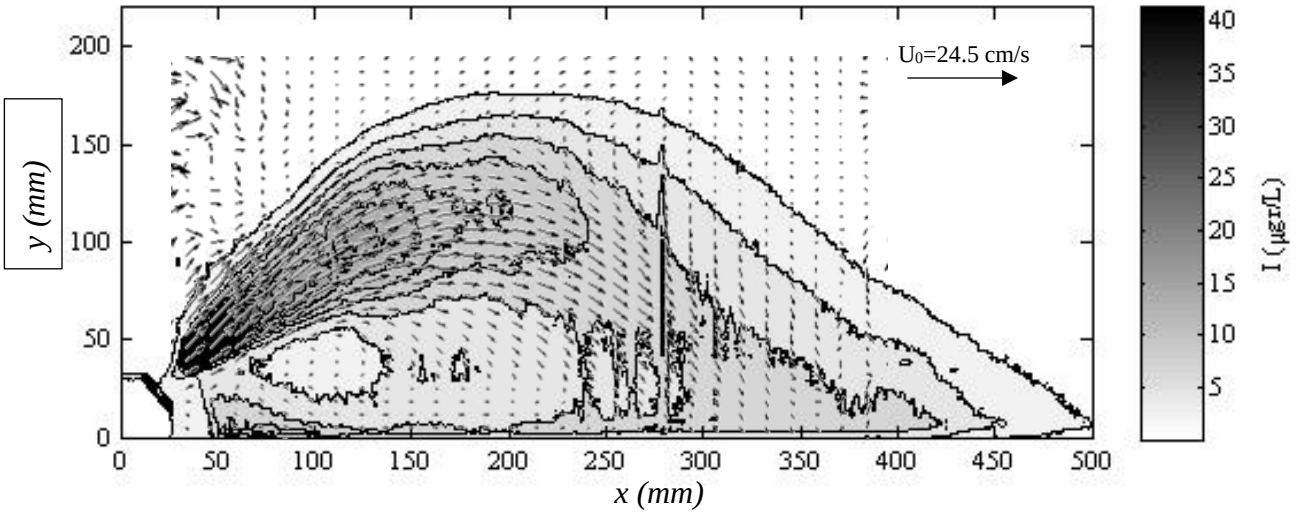


Figure 4-3. Jet centerline superimposed onto the contours of the velocity field (W-01)

Jet trajectory or jet centerline is an important component used to characterize the jet flow. This component can be derived from the maximum velocity or concentration location at different cross-sections perpendicular to the jet which according to Shao (2009), for an inclined dense jet, is only possible by a time-consuming iteration. So, in the case of the inclined dense jet, the best way to extract the jet centerline is to use the velocity vector map, starting from the center of the nozzle. It is also argued that the concentration and velocity axes almost concur, except for the fact the concentration axes tend to descend sooner and in faster rate. Centerline trajectories for stagnant conditions and wave environment with different wave periods are shown in Figure 4.4a and 4.4b for two different jet angles. The origin of the data for all test results shown in Figure 4.4 is the nozzle tip.

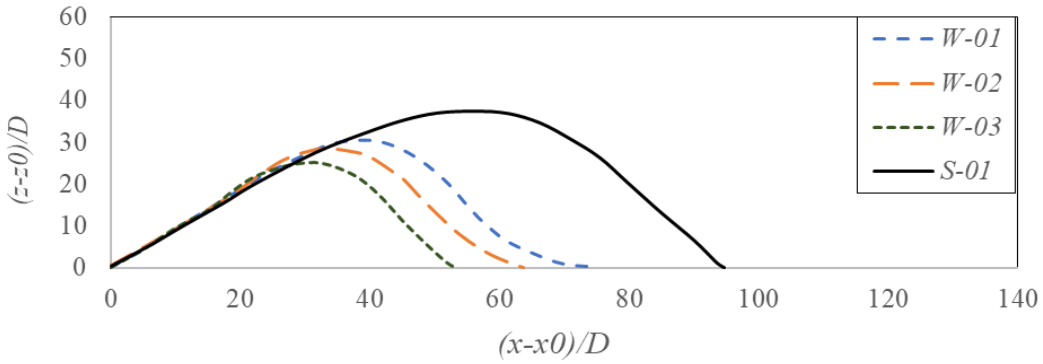


(a)

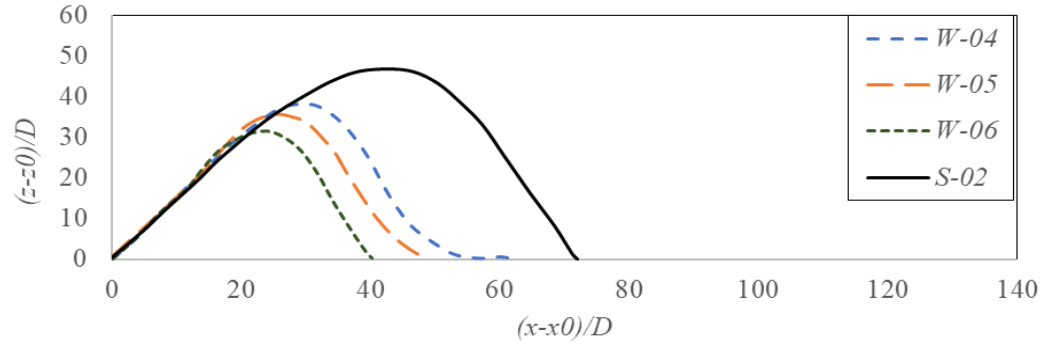


(b)

Figure 4-4 Comparison of dimensionless centerline trajectories of stagnant and wave tests with different wave periods and jets with two inclinations:(a) 45 ̊and (b) 60̊

As expected, the dense jet in stagnant water ambient shoots farther away from the nozzle tip when compared to the trajectories observed for the case of tests with wave. This decrease in the INBJ is due to the periodic oscillation of the initial direction of the jet which increases the entrainment, also the interaction between the two velocity fields (of the INBJ and of the wave motion) causes a larger dissipation of the momentum.

Moreover, while the wave height was kept constant in all experiments, the length of the trajectory decreased with an increase in the wave period.

The flow characteristics and definitions of variables for a single inclined dense jet in stagnant water are shown in Figure 4.5. In Table 4.2, different experimental coefficients for stagnant water

ambient with 45$^o$ and 60$^o$ jets are compared with previous studies which have attempted to derive these coefficients.

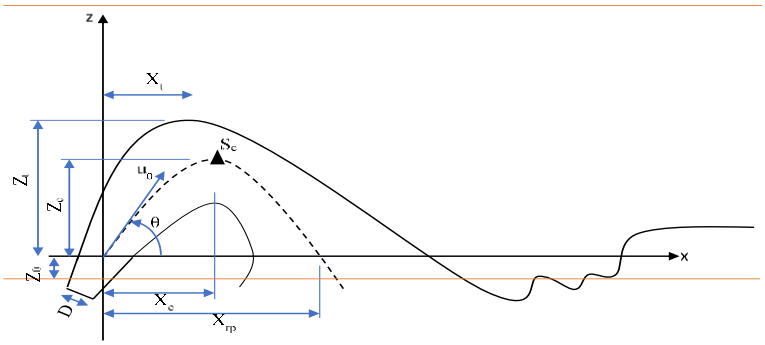


Figure 4-5. Characteristics of a single inclined dense jet in stagnant water

Table 4-2. Comparison of coefficients for stagnant ambient for deep water condition

| Parameter | Normalized Equation | Present study | | Roberts and Abessi 2015 | | Shao & Law 2010 | Zeitoun et al. 1970 |
|---|---|---|---|---|---|---|---|
| | | 45° | 60° | 45° | 60° | 45° | 45° |
| Terminal rise height | *Zt/DFr* | 1.54 | 1.84 | 1.80 | 2.25 | 1.47 | 1.43 |
| Horizontal location of return point | *Xr/DFr* | 3.18 | 2.41 | 3.60 | 2.75 | 2.83 | 3.33 |
| Vertical location of centerline peak | *Zc/DFr* | 1.10 | 1.37 | 1.33 | 1.65 | 1.14 | - |
| Horizontal location of centerline peak | *Xc/DFr* | 1.66 | 1.96 | 2.25 | 1.90 | 1.69 | - |
| Centerline peak dilution | *Sc/Fr* | 0.48 | 0.51 | 0.58 | 0.61 | 0.46 | 0.42 |

In Table 4.2 the dilution is defined as S =$c_o$/c, $c_o$ is the effluent tracer concentration equal to 100 µg/L in these experiments, and c is the local time-averaged tracer concentration. As shown in Table 4.2, the coefficient obtained from this study was found to be similar to the ones captured in previous studies.

The inclined negatively buoyant jets are characterized by the jet discharge volume flux ($Q_0$) and kinematic momentum flux ($M_0$), given below (Lai and Lee, 2012):

$$Q_0 = \frac{U_0 \pi D^2}{4} \tag{4.4}$$

$$M_0 = \frac{{U_0}^2 \pi D^2}{4} \tag{4.5}$$

$$B_0 = Q_0 g_0 \tag{4.6}$$

where $D$ is the jet diameter, $U_0$ is the jet velocity, $g_0$ is the effective gravity defined by:

$$g_0 = \frac{\Delta\rho}{\rho_0} g \tag{4.7}$$

Where $\Delta\rho$ is the initial density difference between the effluent and the ambient; $\rho_0$ is the initial density of the effluent; g is the acceleration due to gravity. For the jet in current only environment and wave only environment, following length scales are defined as (Fischer, et al. 1979):

$$l_m = \frac{{M_0}^{1/2}}{u_c} \tag{4.8}$$

$$l_w = \frac{{M_0}^{1/2}}{u_w} \tag{4.9}$$

$$z_m = \frac{B_0}{{u_c}^3} \tag{4.10}$$

$$z_w = \frac{B_0}{{u_w}^3} \tag{4.11}$$

where $u_c$ and $u_w$ are the crossflow velocity and characteristic wave velocity, respectively. For the turbulent jet for wave-current, the length scale is defined as: (Wang et al. 2015)

$$l_a = \frac{{M_0}^{1/2}}{u_a} \tag{4.12}$$

$$z_a = \frac{B_0}{{u_a}^3} \tag{4.13}$$

$$u_a = (u_w)^{1/5}(u_c)^{4/5} \tag{4.14}$$

Centerline trajectories of the jets versus horizontal distance in the presence of wave only and for the cases with wave and current, for their MDFF region, are shown in Figures 4.6a – 4.6d. The numbers are normalized by the length scales, $l_w$ and $l_a$, corresponding to each experimental condition.

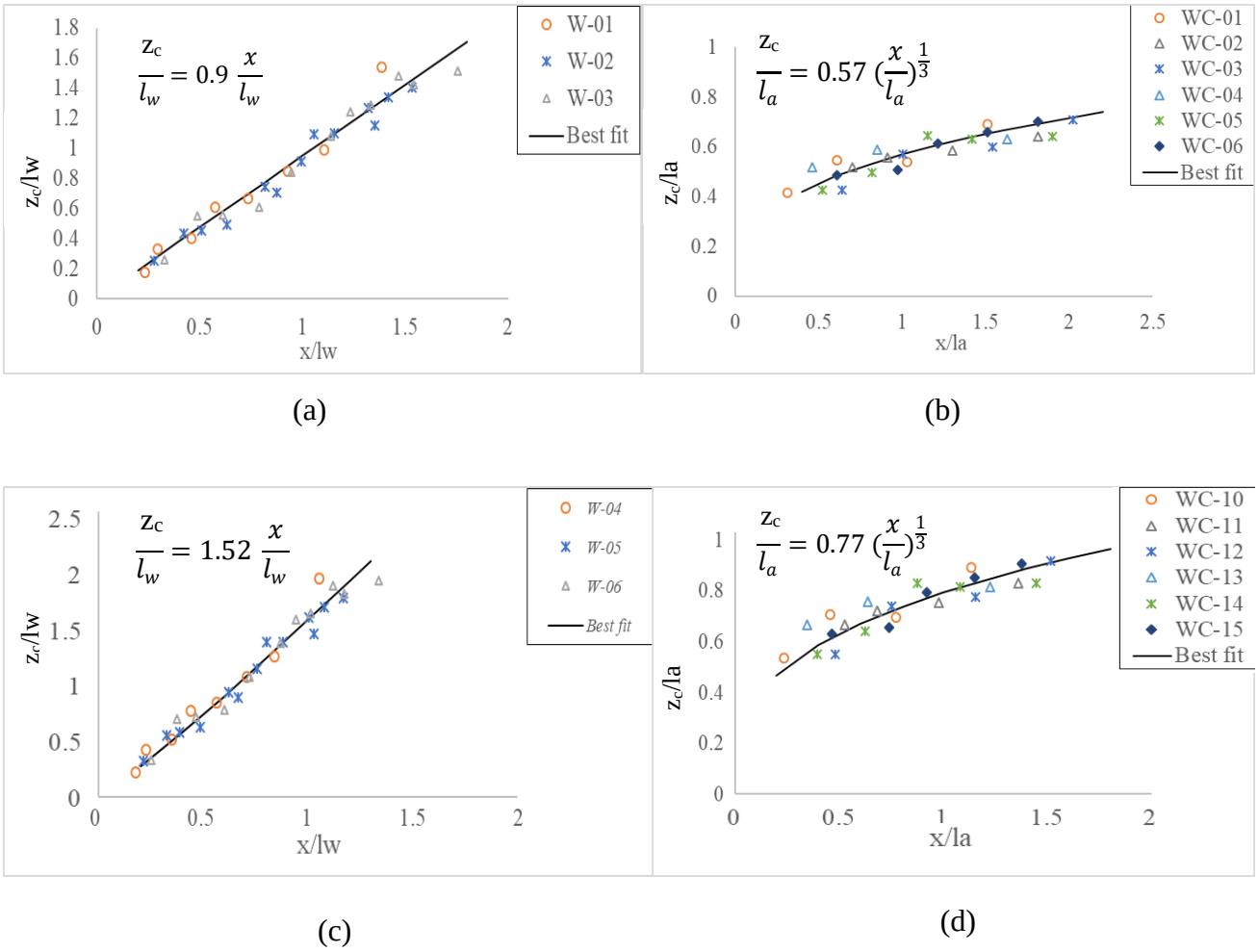


Figure 4-6. Dimensionless relationship between the centerline trajectory and the horizontal distance in MDFF region for the jet in (a) and (c) waves only for 45° and 60° (b) and (d) waves and current for 45° and 60°.

As shown in Figures 4.6a and 4.6c, the relationship between the jet centerline trajectory and the distance from the nozzle, in wave only environment, could be approximated by the following relationship:

$$\frac{z_c}{l_w} = E_{wcl}\ \frac{x}{l_w} \qquad (4.15)$$

where $E_{wcl}$ for the jets with angle of 45° and 60° is estimated to be 0.9 and 1.52 respectively.

Additionally, the experimental results for the tests with waves and current, could be approximated as:

$$\frac{z_c}{l_a} = E_{wccl}(\frac{x}{l_a})^{\frac{1}{3}} \qquad (4.16)$$

Similar equation was found by Chu (1996) and Wang (2015) for non-buoyant jet in waves-cross flow environment. While the power 1/3 is similar to the one proposed in their studies, different coefficient ($E_{wccl}$) in the present cases is obtained due to the differences in experiment conditions. For the case of this study, for buoyant jet and a densiometric Froude number, *Fr,* equal to 34, the $E_{wcc}$ for the jets with angle of 45˚and 60˚is equal to is equal to 0.57 and 0.77 respectively.

### 4.3.3. Terminal Rise Height

The terminal rise height for an inclined dense jet is the point where the vertical component of the initial momentum of the jet decreases to zero. As such, the jet will first rise to this terminal rise height and then it will fall onto the bed. This parameter is important for the design of brine discharge systems, as it can be used such that the plume is kept below the water surface.

Different terminologies for this parameter were reported in the literature (Shao and Law, 2010), such as the maximum rise height (Madni and Ahmed, 1989), maximum height of the top boundary (Zeitoun et al., 1970) and terminal rise height (Roberts and Toms, 1987). The latter term is adapted herein and denoted as $Z_t$. There are also different approaches to determine the terminal rise height. According to Jirka (2008), the terminal rise height can be determined as the visual boundary of the captured flow images. Jirka mentioned that this method involves many uncertainties due to the amount and type of dye used, the recording instrument sensitivities, and other parameters. The commonly-used integral model CORJET uses two cut-off levels of 3% and 25% for the visual boundary. In this paper, the 3% level is used to derive the terminal rise height, similar to the study performed by Shao and Law (2010).

The terminal rise height, $Z_t$, for the concentration is normalized by the nozzle diameter and is plotted versus its distance from the nozzle with the angles of 45˚ and 60˚ in Figure 4.7. The initial nozzle height, $Z_0$, is subtracted from the given $Z_t$. As previously shown, the influence of the wave on the geometry of inclined negatively buoyant jet resulted in its rotation. Compared to the stagnant water conditions, this rotation decreases the jet terminal rise height for the tests with waves.

Moreover, in the presence of only the current (symbols with red color), the terminal rise height was lower compared to the case of stagnant water.

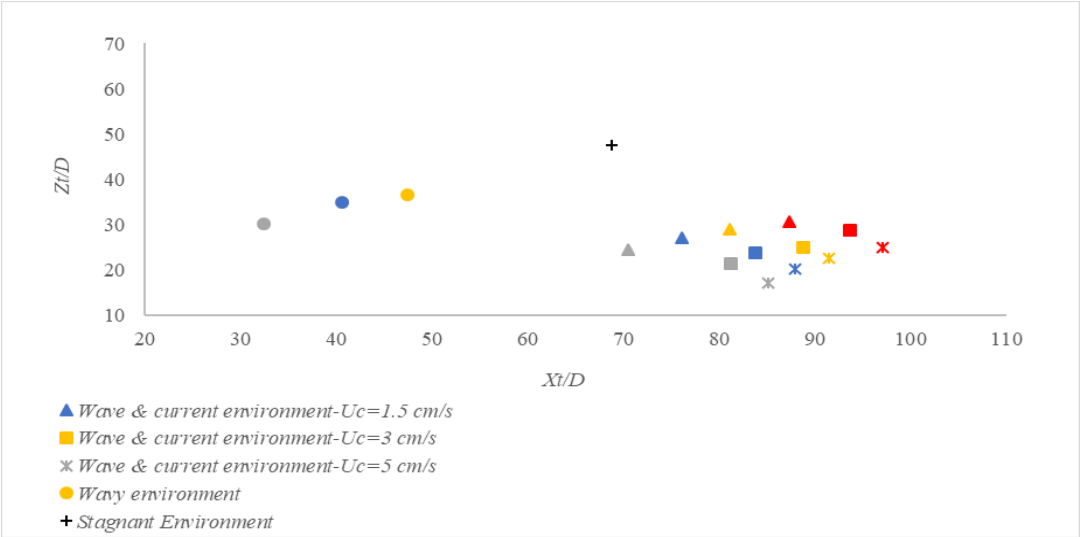


(a)

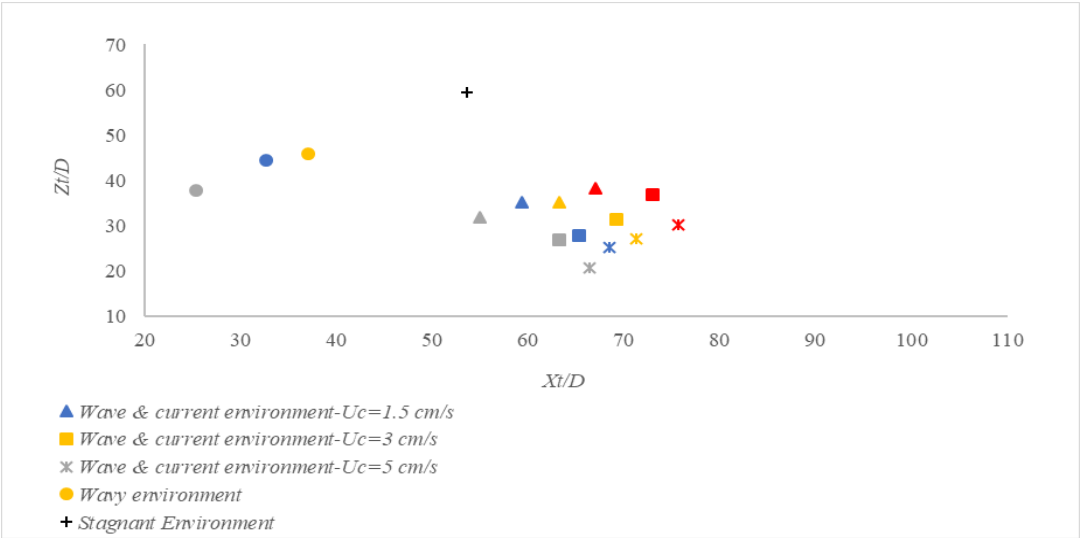


(b)

Figure 4-7. Normalized terminal height rise for different experimental conditions for different wave periods (T1=Yellow, T2= Blue, T3=Gray, without wave=Red), jet angle is (a) 45° (b) 60°

Figure 4.7 also depicts the terminal rise height in the presence of waves and in the wave-current environment, for a constant wave height and different wave periods, which are indicated in

Figure 4.7 with symbols of different color. It can be observed that, as the wave period increases, the terminal rise height decreases for all investigated conditions. This confirms the result of the study by Ferrari and Querzoli (2015).

Terminal rise height of the jet with an angle of 45˚versus various wave periods for the wave-only conditions, as well as for the combined wave and current cases, are shown in Figure 4.8a and 4.8b, respectively. The terminal rise heights are normalized by the length scales $z_w$ and $z_a$ corresponding to the wave-only and the wave-current conditions, respectively.

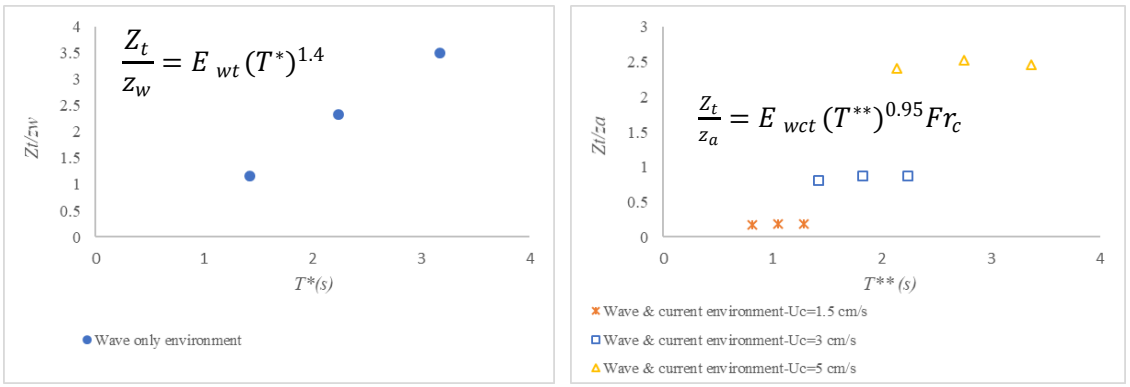


(a) (b)

Figure 4-8. Dimensionless relationship between the terminal rise height and the wave periods for the jet in (a) waves-only (b) wave and current conditions.

As shown in Figure 4.8a, that the relationship between the terminal rise height and the wave periods, in wave only environment, can be approximated by the following relationship:

$$\frac{Z_t}{z_w} = E_{wt}(T^*)^{1.4} \qquad u_c = 0 \; and \; u_w > 0 \qquad (4.17)$$

$$T^* = (Tu_w)/h \qquad (4.18)$$

Where $E_{wt}$ is estimated to be 0.73 for wave-only condition.

Additionally, the results of the experiments in wave-current environment, can be approximated as

$$\frac{Z_t}{z_a} = E_{wct}(T^{**})^{0.95}Fr_c \qquad u_c > 0 \;\; and \; u_w > 0 \qquad (4.18)$$

$$T^{**} = (Tu_a)/h \qquad (4.19)$$

Where $E_{wct}$ is estimated to be 4.85 in wave-current condition.

As mentioned before, this parameter is important for the design of brine discharge systems. Having the wave velocity and periods, engineers can evaluate if the plume is kept below the surface water especially in shallow coastal waters. As full submergence of the brine plume is generally preferable in design practices.

### 4.3.4. Centerline peak and mean concentration field

The jet centerline peak is the distance defined with respect to the centerline trajectory, which is previously determined and plotted. The horizontal and vertical locations ($X_c$, $Z_c$) of the centerline peak are normalized by the nozzle diameter and are further plotted versus the horizontal distance from the nozzle for different test conditions in Figure 4.9. Since jets with different angles show similar behavior, the results are only presented for the jet with angle of 45°.

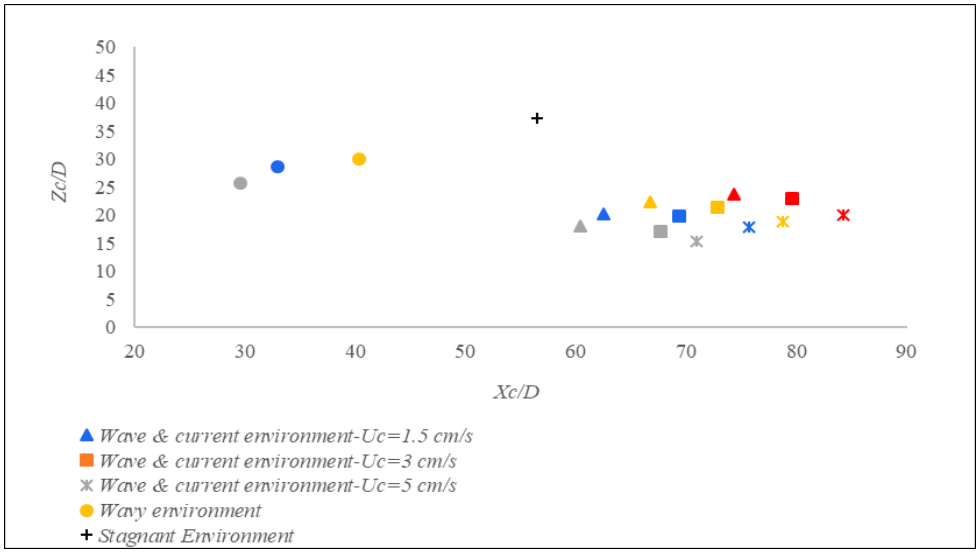


Figure 4-9. Normalized centerline peak in different experimental conditions for different (T1=Yellow, T2= Blue, T3=Gray, without waves=Red), jet angle is (a) 45° (b) 60°

Just as in the case of the terminal rise height, as the wave period increased, the centerline peak became smaller for all test conditions while with increasing current velocity, the centerline peak decreased.

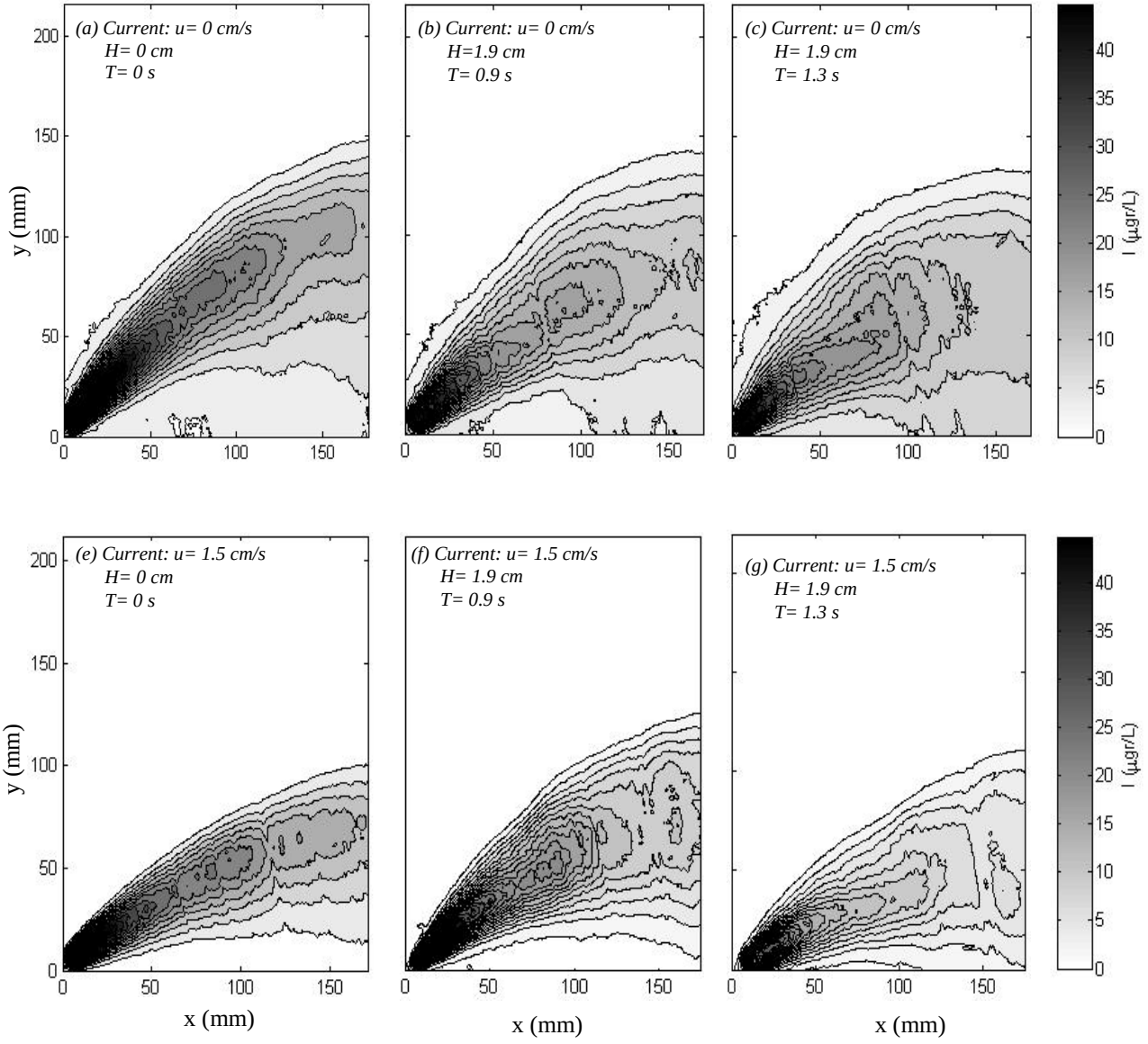


Figure 4-10. Comparison of mean concentration field of the jet in different wave and current conditions

Figures 4.10a through 4.10g show comparisons of the mean concentration field of the jet with 45° inclination for different wave periods, with and without the presence of current.

Comparing Figure 4.10b with Figure 4.10c, and Figure 4.10f with Figure 4.10g, one can observe that the jet dilution along the centerline will increase with an increase in the wave period, while the jet width does not significantly increase. At the same time, comparing Figure 4.10a with Figure 4.10b, and Figure 4.10e with Figure 4.10f under wave effect, shows that the jet width in wave-

only environment is significantly larger than that of the stagnant environment, and as a result, the dilution of the jet also increases. Similar behavior was observed for the jet with an angle of 60°.

### 4.3.5. Minimum dilution at centerline peak

The minimum dilution at specific locations inside or in the vicinity of the jet is important to better understand the dispersion processes and also in design of the discharge outfalls. The centerline peak is important to investigate when studying the jet behavior because, in environmental impact assessments, the dilution achieved in the mixing zone is of primary concern. Dilution at the jet centerline peak is normalized here by the Froude number, *Fr*, and plotted versus the wave period in Figure 4.11. As these results suggest, the wave period has a less significant effect on the ratio of $S_c/F_r$. Moreover, for the cases with waves combined with various current velocities, the $S_c/F_r$ ratio increased as the wave period increased. For tested wave -only conditions, the relationship between $S_c/F_r$ and the wave periods, can be approximated by the following equation:

$$\frac{S_c}{Fr} = E_m\,(T^*)^{0.12} \qquad \mathrm{u_c} = 0 \ \text{and}\ \mathrm{u_w} > 0 \qquad (4.19)$$

For waves-only conditions, $E_m$ is estimated to be 0.93. By examining the experimental data for the tests with co-existing of waves and current, the general form of the equation would be:

$$\frac{S_c}{Fr} = E_{mc}\,(T^{**})^{0.4}\,Fr_c^{\,0.5} \qquad \mathrm{u_c} > 0 \ \text{and}\ \mathrm{u_w} > 0 \qquad (4.20)$$

*where* $E_{mc}$ is estimated to be 6.55.

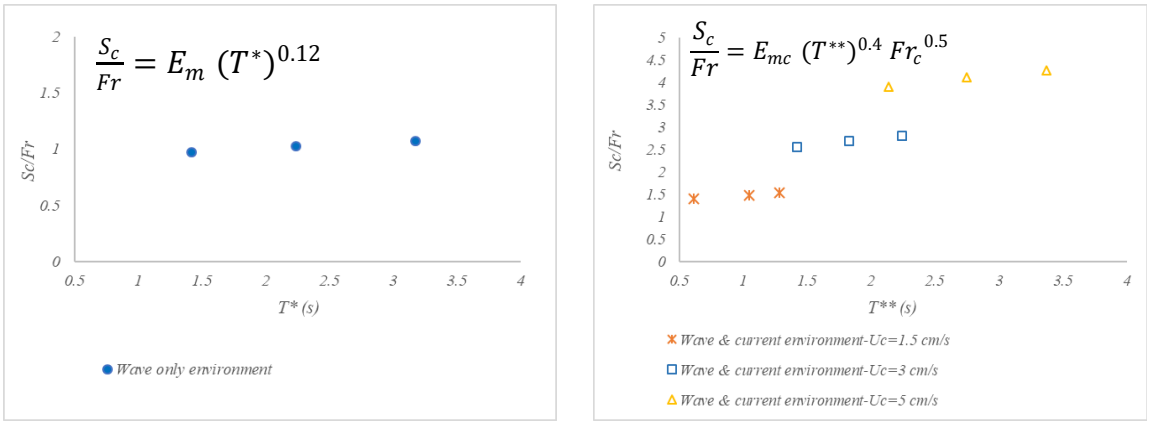


(a) (b)

Figure 4-4-21. Minimum dilution at centerline peak as a function of wave period for different environment condition

As mentioned before, for most of the tests, full field was captured in LIF and PIV record. However, for the wave-current tests and current-only tests, only the upstream portions of the discharges were captured due to the initial momentum leading to long jet trajectories. Thus, the return point dilution ($S_{rp}$), which is another important factor for designing the discharge outfalls, is presented in Figure 4.12 for wave-only tests.

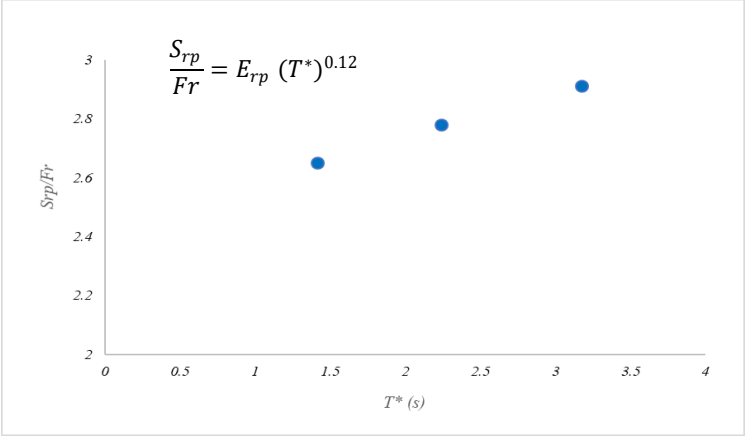


Figure 4-14-3. Minimum dilution at return point as a function of wave period

As shown in Figure 4.12, the $S_{rp}/F_r$ ratio increased as the wave period increased. For tested conditions, the relationship between $S_{rp}/F_r$ and the wave periods, can be approximated by the following equation:

$$\frac{S_{rp}}{Fr} = E_{rp}\ (T^*)^{0.12} \qquad (4.22)$$

where $E_{rp}$ is an empirical coefficient estimated to be 2.54. As the design of a marine outfall centers on the dilution required to meet the relevant guidelines, these empirical equations can be used to optimize the outfall location

### 4.3.6. Cross sectional velocity profile

Beside analyzing the concentration field and dilution, investigating the velocity field characteristics can also provide valuable insight into the behavior of the inclined dense jet. To do so, the planar axial velocity component, *U*, at various downstream locations for W-01 is shown in Figure 4.13. It can be observed that, for the first few cross-sections, the velocity profiles have a symmetric Gaussian distribution. However, as the jet location reaches a distance of 13D from the initial point, the lower half of the profile starts expanding laterally with respect to its propagation direction. For the jet with angle of 60° with the same ambient conditions (W-04), symmetric Gaussian distribution held up to 19D.

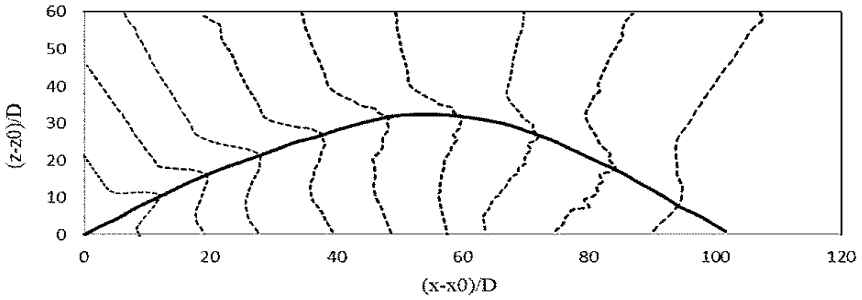


Figure 4-4-43. Cross-sectional velocity distribution at various locations (W-01) downstream of the nozzle

To better identify the changes in the Gaussian distribution, the normalized cross-sectional profiles of $U/U_c$ are plotted versus $r/b_u$ in Figure 4.14, where $U$ is the velocity along the cross-section, $U_c$ is the maximum velocity along the cross-section, $r$ is the radial distance, and $b_u$ is the velocity spread width, using the $e^{-1}$ notation as conducted by Shao and Law (2010) for the stagnant ambient.

Contrary to the upper half of the distribution, which follows an approximately Gaussian profile, one can observe that the lower half deviates from the Gaussian fit. Similar pattern was observed for all other experiments which are not presented herein due to space limitations. This behavior is similar to no-wave environment (Gildeh et al. 2015)

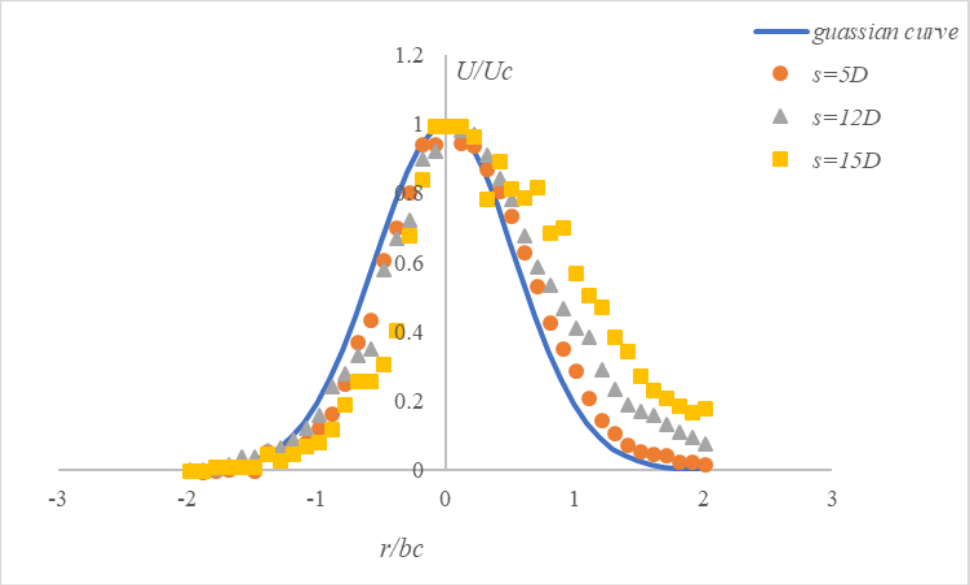


Figure 4-14. Normalized velocity profiles at various downstream cross-sections (W-01)

### 4.4. Conclusions

In the present study, a series of experiments were carried out on negatively buoyant jets in a wave-current flume. The main objective was to investigate the influence of the wave–only or wave-current ambient condition on the initial dilution and geometry of the negatively buoyant jets. Both the concentration and velocity fields were measured using LIF and PIV techniques, respectively. The following remarks were concluded from the work:

- This study confirmed that under the effect of waves, the jet's body could be divided into three regions: MDNF, MDFF, and PPR. In the case of the MDNF, the jet entrainment and the momentum dominate, such that the jet retains its original behavior. MDFF is the region where the centerline is deflected by the effects of wave motion and the jet is further slowed down. The last region is PPR, where the jet initial momentum becomes negligible and the jet is only affected by ambient flow hydrodynamic conditions.
- The trajectories of dense jet in stagnant ambient water was longer comparing to the jets in wavy conditions. Also, increasing the wave period decreases the length of the trajectory while the wave height remains almost constant. Empirical formulae for predicting the jet centerline trajectory from nozzle distance are proposed for wave-only as well as wave-current conditions.

- The wave motion affects the inclined negatively buoyant jet geometry, resulting in the jet's rotation and an increase in its width. This can result in a decrease of the maximum height and centerline peak of the plume. Compared to the stagnant water conditions, the jet rotation decreases the terminal rise height and centerline peak in wave conditions, where an increase in wave period, decreases the terminal rise height and centerline peak. Also, in current-only conditions, the terminal rise height and centerline peak are lower compared to the case of stagnant water. Empirical formulae for predicting jet terminal rise height from wave period are proposed for wave-only, and wave-current conditions. This parameter is important for the design of brine discharge systems, as full submergence of the brine plume is generally targeted as a design requirement.
- Using mean concentration field obtained from LIF images, it was found that the jet dilution along the centerline increases with an increase in the wave period, while the jet width does not significantly increase. Also, under the effect of waves, the jet width is significantly larger than that occurring in the stagnant environment; thus the dilution of the jet also increases.
- The minimum dilution at specific locations inside or near the jet is very important for design purposes. The design of a marine outfall is based on the degree of dilution required to meet relevant guidelines. More accurate calculation of the dilutions conducted in this study led to derivation of empirical formulae relating the minimum dilution at centerline peak and return point (for wave-only environment) to the Froude numbers and wave periods. These formulae can be used in environmental impact assessment study of outfalls and to optimize the location and configuration of marine outfalls. As such, engineers can configure the outfall design to maximize dilution in the near field.
- The cross-sectional velocity profile in the jet was also investigated. The velocity profile was found to approximately match a Gaussian profile only in the top half of the jet, while the lower part of the jet exhibited a flatter velocity profile, similar to the no-wave case.

It is expected that the findings from this study will help elucidate some of the less understood aspects of the mixing phenomena, with the ultimate goal of assisting practicing engineers to design more efficient outfall systems. The results from the present study address the needs for an accurate

estimation of the dilution parameters, by proposing the empirical formulae and providing additional insights into the mechanics of this complex problem.

# 5. RANS Numerical Simulation of the Effects of Waves on Mixing Processes of negatively buoyant jets[4]


## Abstract

In the presence of waves and currents, the dispersion of turbulent jets into coastal waters involves complex mixing processes. Thus, jet dilution processes are significantly affected compared to cases where a jet is discharged into a stagnant ambient environment. Accurate forecasting of the complex interactions of these jets with waves presents significant challenges and has yet to be fully elucidated. In this paper, numerical simulations of 45° inclined dense turbulent jets into wavy ambient water have been conducted. The wave characteristics were chosen to simulate a typical effluent discharge into the coastal waters of the Mediterranean Sea.

The mixing behavior of the dense jets is studied using a finite volume model (OpenFOAM), and the selected turbulence models include two Linear Eddy Viscosity models, i.e., the RNG k-ε and realizable k-ε; one Nonlinear Eddy Viscosity Model, i.e., the Nonlinear k-ε; and one Reynolds Stress model, i.e., the LRR. Based on the numerical results, the geometrical characteristics of the dense jets as well as their mixing and dilution characteristics have been studied through the analysis of the cross-sectional concentration and velocity profiles. The results of this study are compared to detailed, novel experimental investigations using LIF-PIV techniques done by the authors in a previous study, and comparative figures and tables are presented and discussed. It has been observed that the LRR and realizable k-ε models predict the flow more accurately out of the various turbulence models studied herein.



*Keywords*: Inclined negatively buoyant jets, Wave effects, Turbulence models, OpenFOAM


## 5.1. Introduction

Desalination plants remove dissolved minerals from coastal water bodies and produce brine flows with high salt concentrations. Upon discharge, these brine flows have a higher density than that of

[4] Sepideh Khorshid, Abdolmajid Mohammadian, Ioan Nistor "RANS Numerical Simulation of the Effects of Waves on Mixing Processes of negatively buoyant jets", Environmental Fluid Mechanics, Under Review.

the receiving water body, and, therefore, the discharged effluent tends to sink as a negatively buoyant jet. This can cause many environmental impacts, especially in the near field of outfall systems, which is the natural habitat of various marine species (Einav and Lokiec, 2003; Lattemann and Hoepner, 2008). Therefore, it is necessary to achieve rapid mixing and dispersion of concentrated brine discharge in order to minimize the negative environmental impacts of marine outfall systems.

Several experimental studies have been performed on Inclined Negatively Buoyant jets (INBJs) released into stagnant ambient water. For example, Zeitoun et al. (1970) and Roberts and Tom (1987) performed several experiments on INBJs for various angles as well as vertical dense jets using a point-based conductivity meter technique to measure trajectory and minimum dilution. They also reported empirical correlations of dilutions at jet terminal rise height and jet impact points. Lai and Lee (2012) reported a comprehensive investigation on the tracer concentration fields of inclined dense jets for various jet Froude numbers and a broad range of jet angles. They used PIV and LIF systems to measure concentration fields and instantaneous velocity vector map, and the experimental results were then compared to the VISJET model (2003) as well as other experimental data from previous studies.

Dense effluents are typically discharged into coastal waters, and therefore the state of the ambient water is an important influencer on jet behaviour. When a jet is discharged into a stagnant water body, the initial dilution of the jet is primarily controlled by the shear entrainment induced by the jet's initial momentum and/or the buoyancy forces. However, when a jet is discharged into coastal waters, due to the presence of waves and currents, more complex mixing processes can occur and significantly affect the jet dilution processes. Since this is the case for most coastal regions, it is necessary to understand the initial dilution under such conditions in order to have a more accurate assessment of the environmental impact on the surrounding waters.

There have been some experimental studies on the effects of waves on non-buoyant turbulent jets, including one by Chin (1988), who studied the effects of waves on turbulent round jet characteristics and noted that the dilution of the jet was significantly higher in a wavy environment compared to dilution in a stagnant ambient one. Koole and Swan (1994) studied the dispersion of non-buoyant jets beneath a series of gravity waves and showed that the zone of flow establishment is shorter in the presence of waves, and that the rate of entrainment increased in wave-induced

mixing conditions. Tam and Li (2008) carried out an experimental study of vertical jets discharged under random waves and showed that in the presence of waves, the centerline of the jet velocity shows a rapid decrease, while the waves enhance the jets' width and turbulence. This increase in turbulence is because when the jet is affected by waves, its mean kinetic energy decreases while its turbulent kinetic energy increases, and as a result, the jet dilution capacity increases.

Wang et al. (2015) conducted a series of physical experiments on the initial dilution of vertical non-buoyant round jets in a wave-current environment. Using a camcorder and a peristaltic suction pumping system, they were able to record the dilution processes and concentration fields, and proved that the jet width in a co-existent wave and current environment increases more significantly than in a current-only environment. They also suggested some empirical formulas to generalize their experimental findings.

While the above-mentioned experimental studies mostly focused on the effect of waves on the flow characteristics of non-buoyant jets, only in a few cases were buoyant jets studied, and therefore the effects of surface waves on buoyant plumes are less understood. One of the studies that has been carried out on the wave effects on positively buoyant plumes is the study by Shuto (1974). Using a point-measuring technique wherein samples were taken near the water surface and their salinity and concentration of chromium measured, Shuto investigated the surface dilution. Chin et al. (1987) investigated the influence of surface wave on buoyant jets and derived the relevant dimensionless variables, and their study included an experimental program to determine the relationship between surface wave parameters and dilution relative to the no-wave case.

Sharp et al. (2014) studied the effect of surface waves on a positively buoyant plume discharged from a multiport diffuser, and concentrations were measured using a Laser Induced Fluorescence (LIF) technique. The average increase in dilution of the plume due to wave effects was found to be similar to the increase in surface dilution previously reported by other researchers, and the greatest increase in dilution was found to be in the region near the diffuser before the individual plumes had merged.

While experimental studies have been conducted in this field of research, numerical studies have very rarely been performed for the case of dense inclined jets, which are just recently being pursued and need further investigation. Vafeiadou et al. (2005) studied inclined negatively buoyant jets numerically using a three-dimensional model named CFX-5. They employed the $k$-$\omega$ SST

(Shear Stress Transport) turbulence model, which is based on a blend of the *k*-$\varepsilon$ and the *k*-$\omega$ models and used an unstructured grid and more refined computational grid near the bottom and around the inflow nozzle. They compared their modeled results with experimental data from Roberts et al. (1997) and concluded that their model underestimated the terminal rise height and the return point. The FLOW-3D model, which is a commercial CFD package, along with the RNG *k*-$\varepsilon$ turbulence model was used by Kim and Cho (2006) to model buoyant flows of heated water discharged from surface and submerged side outfalls in both shallow and deep water with a cross-flow.

Focusing on vertical dense jets with no inclination, Elhaggag et al. (2011) performed both experimental tests and numerical simulations using the FLUENT CFD commercial software and compared the modeled results and experimental data.

Gildeh et al. (2014) performed a numerical study on the near-field flow and mixing characteristics of thermal and saline wall jets released from a submerged outfall into stagnant ambient water. The performance of different Reynolds-averaged Navier-Stokes (RANS) turbulence models were tested in their study, and the results were compared to both available experimental and numerical data. It was found that the realizable k-ε and LRR models performed best among the seven models chosen for their study.

Since to the best knowledge of the authors, the effects of waves on INBJs have never been numerically investigated, this study presents the numerical modelling results of the effects of waves on inclined dense jets. Negatively buoyant jets with the angle of 45° were studied using an open-source CFD code called OpenFOAM (OPEN Field Operation and Manipulation) (OpenFOAM user and programmer guides, 2013), which was modified by the authors to incorporate the effects of buoyancy and salinity transport. Numerical model characteristics were chosen to simulate a typical effluent discharge into the coastal waters of the Mediterranean Sea, and the equations were solved using a finite volume method. The mixing and dispersion characteristics of the jets were studied together with the influence of the geometrical outflow characteristics such as terminal rise height, return point, and centerline trajectory. The effects of wave periods were also investigated. Four turbulence models, including RNG *k*-$\varepsilon$, realizable *k*-$\varepsilon$; Nonlinear *k*-$\varepsilon$; and LRR, were tested.

The authors of this paper previously carried out a series of experiments on inclined negatively buoyant jets in the presence of waves in which the use of Particle Image Velocimetry (PIV) and

Laser Induced Fluorescence (LIF) techniques allowed not only investigation of the velocity fields, but also accurately investigating the diluting effect of surface waves on negatively buoyant jets (Khorshid et al., 2019). That investigation led to the development of empirical formulae that can be used for the design of outfalls for negatively buoyant jets in a wave-current environment. The results of the numerical simulations have been compared with experimental data, and comparative tables and graphs were presented.

This manuscript is organized as follows. Section 2 describes the numerical model plan and computational setup. In Section 3, the numerical results, including the jet developments and trajectories, terminal rise heights, centerline peaks, mean jet concentration fields, and minimum dilutions at centerline peaks, are presented and discussed. Additionally, empirical formulae suggested in a previous study by the authors (Khorshid et al., 2019) are verified using numerically modeled values. Finally, the conclusions of this study are presented.

### 5.2. Numerical Model

The computational domain was configured based on a series of flume tests carried out at the R+D Centre of Technological Innovation in the Building and Civil Engineering (CITEEC) Department of the University of A Coruña (Spain) with an experimental setup for a PIV-LIF study of buoyant plume under the combined effects of waves and current (Khorshid et al., 2019). The wave-current flume was 20 m long, 0.6 m wide, and 0.35 m deep. The jet nozzle, with a diameter of 3 mm, was located 10 mm vertically above a simulated sea bottom. Inclined negatively buoyant jets with a higher density than the ambient water ($\Delta\rho/\rho 0$ = 2.136 %) were released into the ambient water body in the flume at angles of 45 and 60 degrees. In the experiments, wave parameters were chosen to simulate certain scaled-down typical Mediterranean wave conditions with respect to kinematic similarity. The wave height was chosen to be 1.9 cm and the three most probable wave periods for the medium regime (according to the Oceanographic Data Bank, Ports of Spain, for the wave buoy of Cabo de Palos, Alicante) were also chosen as 0.9, 1,1, and 1.3 seconds in order to see the effect of wave period on the mixing process. The discharge velocity was 0.85 m/s.

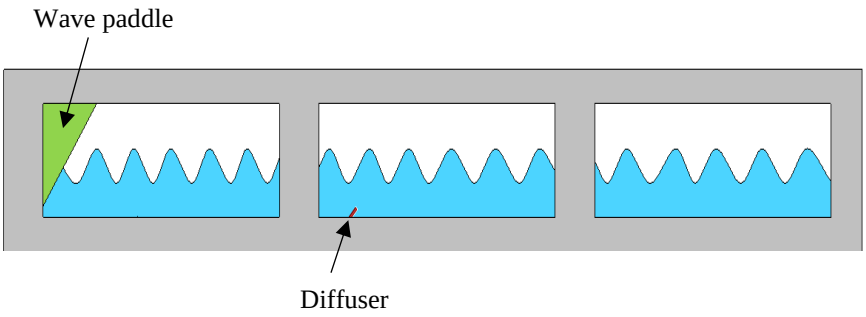


Figure 5-1 Experimental setup for PIV-LIF study of buoyant plumes under the combined effects of waves and current (Khorshid et al., 2019)

### 5.2.1. Boundary conditions and computational setup

The boundary conditions employed in this investigation are shown in Figure 5.2. The nozzle tip is defined as the inlet for salty water, and the inlet values for k and ε were chosen based on Huai et al. (2010). No-slip boundary conditions were specified at the lower wall and backwall boundary. The standard wall function was used for the boundary conditions of the other parameters at the lower wall (bottom of the flume) and back wall patch, and the standard wall functions for k and ε were used. The right wall was defined as the flow outlet, and the boundary conditions of the outlet patch were defined as zero-gradient in all cases. The inlet-outlet boundary condition was assigned for the top interface (atmosphere). This is normally the same as the zero-gradient open boundary condition, but it switches to the fixed-value boundary condition if any backward flow occurs. Only half of the dense jet domain was considered in this study, since the problem is symmetric. The symmetry boundary was modeled using zero-gradient conditions.

The computational domain was discretized using an unstructured mesh with increasing grid spacing from the center of the dune to the boundaries, as shown in Figure 5.2. The grids were created using the SALOME mesh generator and imported into OpenFOAM. More grid refinement was performed around the nozzle to capture the velocity and concentration at a better quality close to the nozzle. It is noteworthy to mention that a mesh independency test was performed to obtain the best density for the mesh grid.

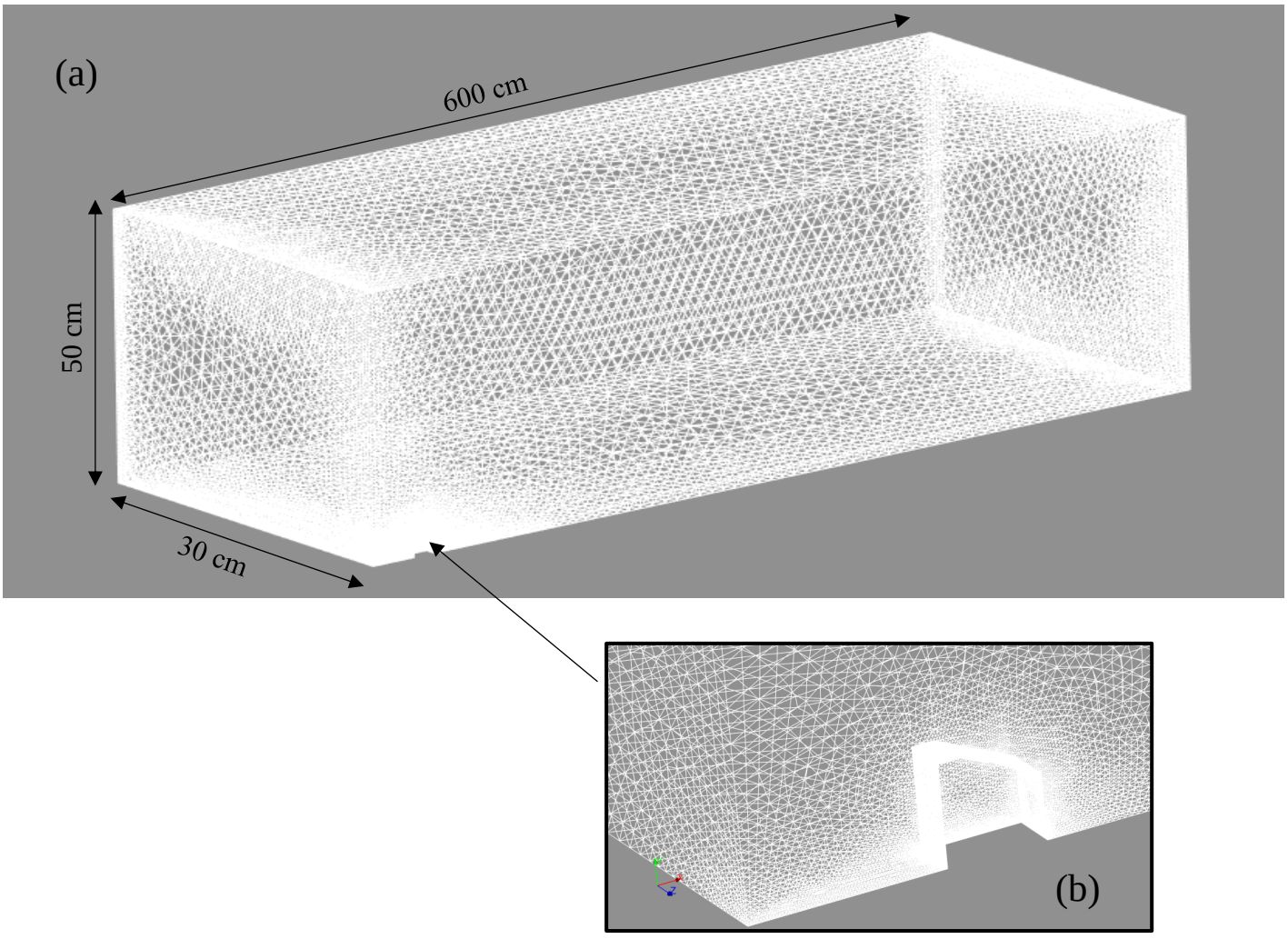


Figure 0-2. Computational domain: (a) refined unstructured mesh system; (b) mesh refinement around the nozzle (zoomed in)

### 5.2.2. Governing equations

Similar to the study by Gildeh et al. (2015), the Navier-Stokes equations for three-dimensional incompressible fluids are divided by the density (ρ), and the buoyancy term is added to the momentum equation in the vertical direction (y-coordinate) to account for variable density effects, as follows:

Continuity equation:

$$\frac{\partial u}{\partial x}+\frac{\partial v}{\partial y}+\frac{\partial w}{\partial z}=0 \qquad (5.1)$$

Momentum equations:

$$\frac{\partial u}{\partial t}+u\frac{\partial u}{\partial x}+v\frac{\partial u}{\partial y}+w\frac{\partial u}{\partial z}=-\frac{1}{\rho}\frac{\partial P}{\partial x}+\frac{\partial}{\partial x}\left(\vartheta_{eff}\left(\frac{\partial u}{\partial x}\right)\right)+\frac{\partial}{\partial y}\left(\vartheta_{eff}\left(\frac{\partial u}{\partial y}\right)\right)+\frac{\partial}{\partial z}\left(\vartheta_{eff}\left(\frac{\partial u}{\partial z}\right)\right) \quad (5.2)$$

$$\frac{\partial v}{\partial t}+u\frac{\partial v}{\partial x}+v\frac{\partial v}{\partial y}+w\frac{\partial v}{\partial z}$$
$$=-\frac{1}{\rho}\frac{\partial P}{\partial x}+\frac{\partial}{\partial x}\left(\vartheta_{eff}\left(\frac{\partial v}{\partial x}\right)\right)+\frac{\partial}{\partial y}\left(\vartheta_{eff}\left(\frac{\partial v}{\partial y}\right)\right)+\frac{\partial}{\partial z}\left(\vartheta_{eff}\left(\frac{\partial v}{\partial z}\right)\right)-g\frac{(\rho-\rho_0)}{\rho} \quad (5.3)$$

$$\frac{\partial w}{\partial t}+u\frac{\partial w}{\partial x}+v\frac{\partial w}{\partial y}+w\frac{\partial w}{\partial z}=-\frac{1}{\rho}\frac{\partial P}{\partial x}+\frac{\partial}{\partial x}\left(\vartheta_{eff}\left(\frac{\partial w}{\partial x}\right)\right)+\frac{\partial}{\partial y}\left(\vartheta_{eff}\left(\frac{\partial w}{\partial y}\right)\right)+\frac{\partial}{\partial z}\left(\vartheta_{eff}\left(\frac{\partial w}{\partial z}\right)\right) \quad (5.4)$$

where *u*, *v*, and *w* are the mean velocity components in the *x*, *y*, and z directions, respectively, *t* is the time, *P* is the fluid pressure, $\upsilon_{eff}$ represents the effective kinematic viscosity ($\upsilon_{eff}=\upsilon_t+\upsilon$), $\upsilon_t$ is the turbulent kinematic viscosity and υ is the kinematic viscosity, *g* is the gravity acceleration, ρ is the fluid density, and $\rho_0$ is the reference fluid density.

The density is calculated for both the jet and the ambient water according to the equation for the state of seawater proposed by Millero and Poisson (1981):

$$\rho=\rho_t+AS+BS^{3/2}+CS \quad (5.5)$$

where S is the salinity of water and:

$$A=8.24493\times10^{-1}-4.0899\times10^{-3}T+7.6438\times10^{-5}T^{2}-8.2467\times10^{-7}T^{3}+5.3875\times10^{-9}T^{4} \quad (5.6)$$

$$B=-5.72466\times10^{-3}+1.0227\times10^{-4}T-1.6546\times10^{-6}T^{2} \quad (5.7)$$

$$C=4.8314\times10^{-4} \quad (5.8)$$

and $\rho_t$ is the density of water that varies with the temperature (T=20 ℃), as follows:

$$\rho_t=999.842594+6.793952\times10^{-2}T-9.095290\times10^{-3}T^{2}+1.00168\times10^{-4}T^{3}$$
$$-1.120083\times10^{-6}T^{4}+6.536336\times10^{-9}T^{5} \quad (5.9)$$

The governing equations were numerically solved using the finite volume method, and the solver used within OpenFOAM is the modified interFoam. This solver is mostly used for incompressible isothermal immiscible fluids using a Volume of Fluid (VOF) phase-fraction-based interface-capturing approach. In the VOF method, the tracking of the interface between the phases is accomplished by the solution of a continuity equation for the volume fraction of phases. Also, an interface between the species is not explicitly computed, but rather emerges as a property of the

phase fraction field. Since the phase fraction can have any value between 0 and 1, the interface is never sharply defined, but occupies a volume around the region [OpenFOAM User Guide, 2018]. Simulated water and air phase fraction fields and water surface in this study are shown in Figure 5.3.

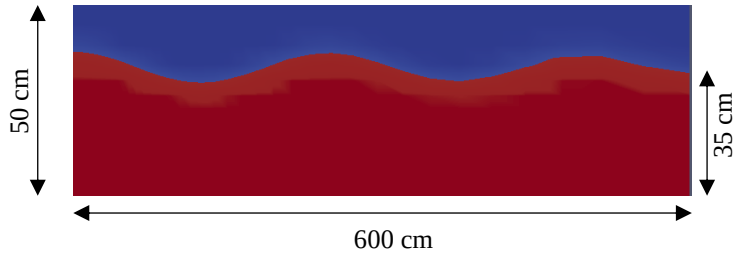


Figure 5-3. Water and air phases in simulated case

### 5.2.3. Turbulence models:

Considering the actual physics of the flow, the desired level of accuracy, and the available computational resources, four turbulence models were chosen for this study, as follows:

(i) RNG k-ε model (Renormalization Group), which is a Linear Eddy Viscosity Model that includes a modification to the transport equation for ε stemming from renormalization group theory. The normal turbulent stresses are positive by definition.

(ii) Realizable k-ε model, also a Linear Eddy Viscosity Model which uses certain mathematical constraints on the normal stresses in order to avoid having negative normal turbulent stresses (Ferbo, 2010).

(iii) Nonlinear k-ε model, a Nonlinear Eddy Viscosity Model where additional terms are introduced into the stress-strain relationship, making the Reynolds stresses a more general function of mean strain and vorticity.

(iv) LRR model (Launder-Reece-Rodi), which is a Reynolds Stress Model in which the turbulent stresses are determined directly by solving a transport equation for each stress component.

## 5.3. Results and discussion

Three different cases of a nozzle with a 45° angle have been numerically simulated for three different wave periods. All four turbulence models have been applied to each of these cases (totalling 12 simulations: 3 cases × 4 turbulence models), and the comparative results are presented in the following sections. The characteristics of the three cases are summarized below.

Table 5-1. Numerical cases - characteristic

| Experiment no. | Jet angle Θ | Δρ/ρ0 % | Discharge velocity U0 (m/s) | Water depth h (m) | Ambient water body velocity Ur (m/s) | Wave height H (cm) | Wave period T (s) |
|---|---|---|---|---|---|---|---|
| W-01 | 45 | 2.136 | 0.85 | 0.35 | 0 | 1.9 | 0.9 |
| W-02 | 45 | 2.136 | 0.85 | 0.35 | 0 | 1.9 | 1.1 |
| W-03 | 45 | 2.136 | 0.85 | 0.35 | 0 | 1.9 | 1.3 |

## 5.3.1. Dimensional Analysis

The inclined negatively buoyant jets are characterized by the jet discharge volume flux ($Q_0$) and the kinematic momentum flux ($M_0$), as given below (Lai and Lee, 2012):

$$Q_0 = \frac{U_0 \pi D^2}{4} \tag{5.10}$$

$$M_0 = \frac{{U_0}^2 \pi D^2}{4} \tag{5.11}$$

$$B_0 = \quad Q_0 \, {g_0}' \tag{5.12}$$

$$g_0 = \frac{\Delta\rho}{\rho_0} \, g \tag{5.13}$$

where $D$ is the jet diameter, $U_0$ is the jet velocity, $\Delta\rho$ is the initial density difference between the effluent and the ambient water, $\rho_0$ is the initial density of the effluent, and $g$ is the acceleration due to gravity (Figure 5.4).

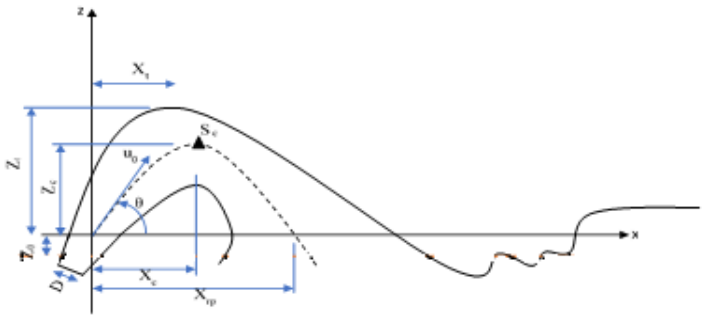

Figure 0-4. Schematic view of inclined dense jet

For a jet in the presence of wave field, the following length scales are defined (Fischer et al., 1979):

$$l_w = \frac{{M_0}^{1/2}}{u_w} \tag{5.14}$$

$$z_w = \frac{B_0}{{u_w}^3} \tag{5.15}$$

where $l_w$ is the length scale which measures the distance required for the buoyancy forces to dominate the plume behavior and $z_w$ measures the distance required for the buoyancy induced momentum to be on the order of the wave-induced momentum. The characteristic wave velocity ($u_w$) is defined below (Wang et al., 2015).

$$u_w = \frac{\pi H}{T} \frac{\cosh(\mathrm{kh})}{\sinh(\mathrm{kh})} \tag{5.16}$$

$$\mathrm{k} = \frac{2\pi}{L} \tag{5.17}$$

where $H$ and L are the wave height and wave length, respectively.

### 5.3.2. Jet Trajectory

Figure 5.5 shows the concentration contour map of an INBJ in a wave environment (W-01) in order to better understand the influence of wave parameters on the jet geometry. This figure is the result of the LRR model for the W-01 wave condition. The flow pattern can be observed in the time series of pictures of the INBJ at different phases of the wave motion. As was also observed in the experiments, three different regions of the jet body dispersion can be observed in the presence of waves. The first region is where the jet tends to preserve its initial direction and

maintain its initial shape and behavior. In this region, the jet entrainment processes dominate, and the jet has more momentum. As such, this region is termed the Jet Deflection Region (JDR). The next region is termed the Transition Region (TR), where the jet slows down through interaction with the waves and by entrainment. The jet centerline is deflected by the wave motion. In this region, due to the interaction with the waves, the jet is further slowed down until it reaches what is called the Developed Jet Region (DJR). In this region, the jet is dominated by the ambient fluid motion and the effect of the jet initial momentum becomes negligible. In Figure 5.5, the wave period is equally spaced in time by $\Delta T = T/4$. t=0 is when the wave trough is above the outlet and t=T/2 corresponds approximately to the instant when the wave crest is above the outlet.

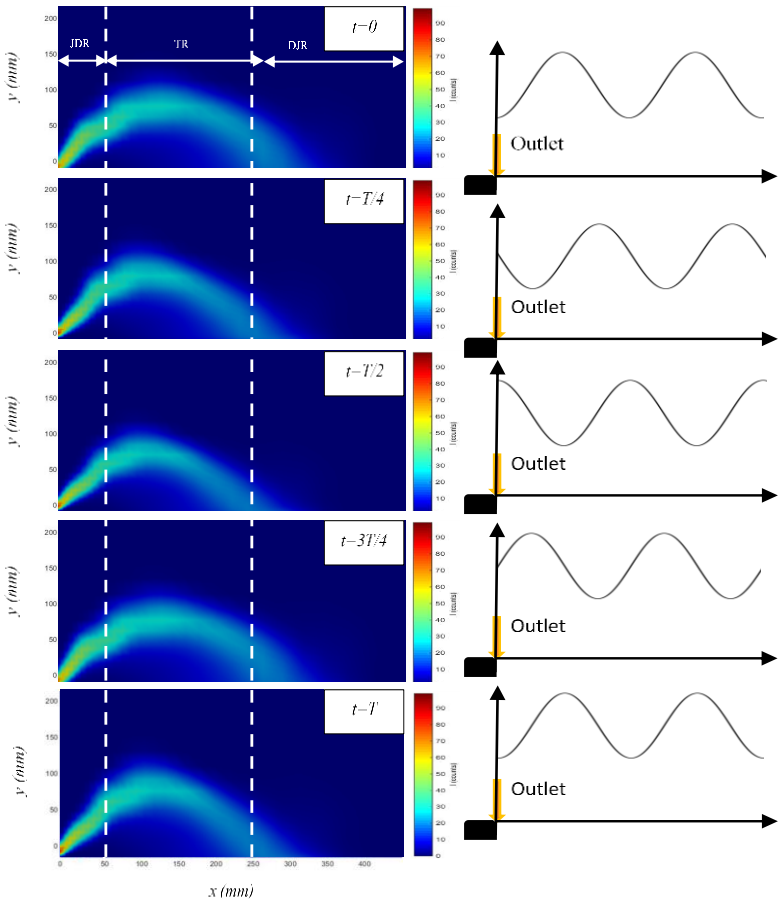


Figure 0-5. Concentration map of an INBJ in a receiving environment with waves of T=0.9 (s) and H=1.9 cm (W-01); results of LRR simulation

Centerline trajectories are also shown for different cases in Figures 5.6a to 5.6c. The origin of the data for all test results shown in Figure 5.6 is the nozzle tip. In the previous experimental study of the same authors, it was shown that, when the wave height was kept constant in all experiments, the length of the trajectory decreased with an increase in the wave period. The same pattern is observed here with the numerical simulations.

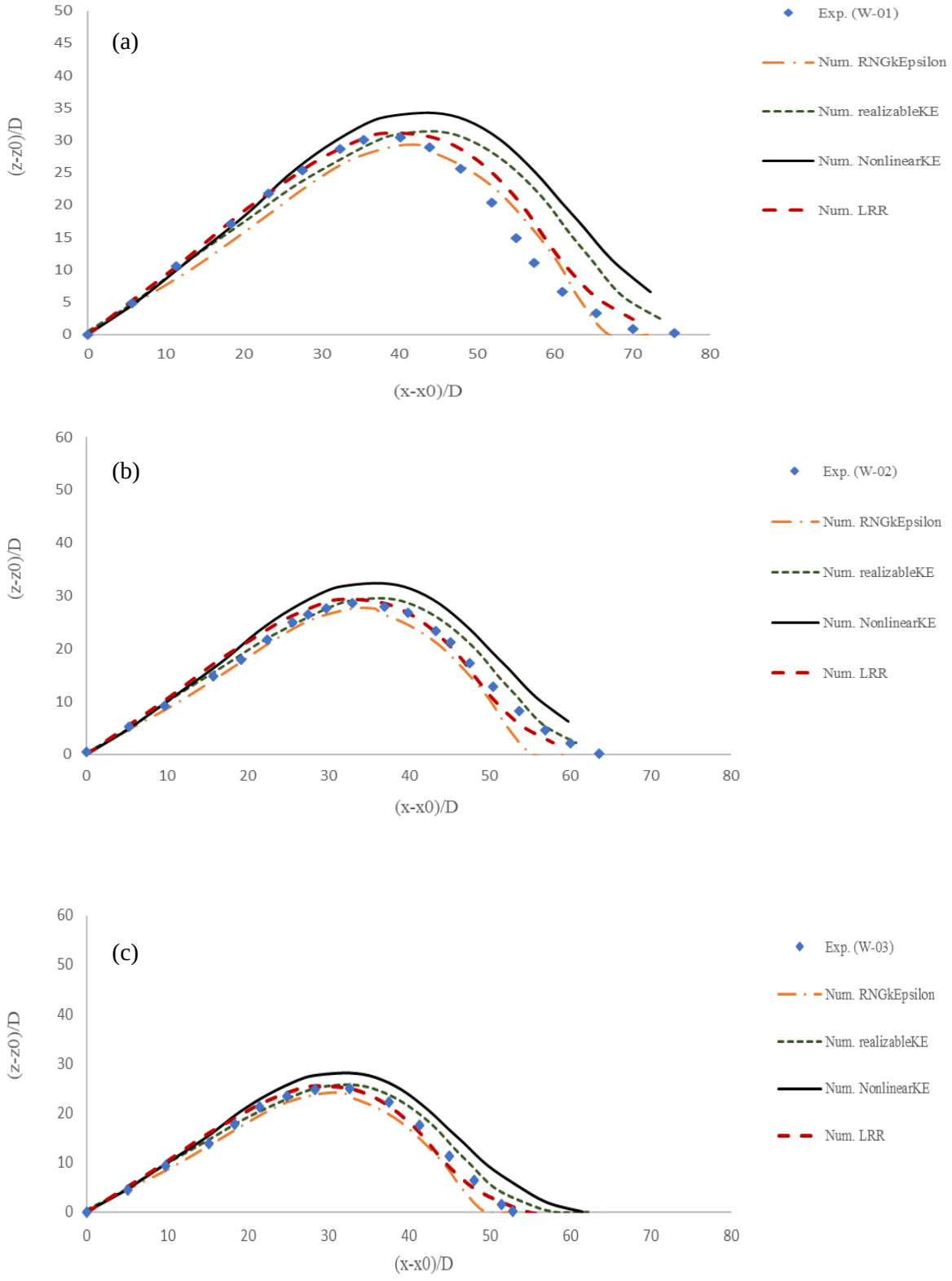


Figure 5-6. Centerline trajectories: (a)T=0.9 (s); (b) T=1.1 (s); (c) T=1.3 (s)

While all four turbulence models are in good agreement with the experimental results up to the maximum terminal rise height, it can be seen that the nonlinear k-ε model overpredicts the trajectory of the jet, especially for the descending portion of the jet flow. On the other hand, the RNG k-ε model slightly underpredicts the terminal rise height.

To obtain a quantitative measurement of the difference between the experimental and numerical results, the Root Mean Squared (RMSE) and R-Squared ($R^2$) were calculated for the centerline trajectories, as presented in Figures 5.6 and Table 5.2. Looking at the RMSE and $R^2$ values demonstrate that LRR and Realizable k-ε model provided a better match with the experimental data among the four turbulence models tested.

Table 5-2. Error coefficient of calculated the centerline trajectory using various turbulence models

| Turbulence model | RMSE | $R^2$ |
|---|---|---|
| RNG k-ε | 1.98 | 0.87 |
| Realizable k-ε | 0.85 | 0.93 |
| Nonlinear k-ε | 2.03 | 0.85 |
| LRR | 0.75 | 0.97 |

In Table 5.3-5.5, using dimensional analysis, the various geometrical and mixing quantities are shown proportionally correlated to the jet densiometric Froude number (coefficients), Fr, as well as, in some cases, the nozzle diameter, D (Shao, 2010).

Based on the graphs in Figure 5.6 and from Tables 5.3-5.5, the results of the realizable k-ε and LRR models are seen as being in better agreement with the experimental data; they show more accurate jet trajectories as well as better estimates of terminal rise height and other parameters, as shown in the tables below. These observations are in line with Gildeh et al. (2014) study on the application of different turbulence models on INBJs in stagnant ambient water.

Table 5-3. Comparison of numerical and experimental coefficients for wave period 0.9 (s)

| Parameter | Normalized Equation | Present study | | | | Experimental results |
|---|---|---|---|---|---|---|
| | | RNG | Realizable | Nonlinear | LRR | |
| Terminal rise height | $C_1=Zt/DFr$ | 1.11 | 1.18 | 1.29 | 1.18 | 1.16 |
| Horizontal location of return point | $C_2=Xr/DFr$ | 2.21 | 2.43 | 2.48 | 2.12 | 2.36 |
| Vertical location of centerline peak | $C_3=Zc/DFr$ | 0.91 | 0.99 | 1.09 | 0.97 | 0.95 |
| Horizontal location of centerline peak | $C_4=Xc/DFr$ | 1.35 | 1.41 | 1.38 | 1.18 | 1.25 |
| Centerline peak dilution | $C_5=Sc/Fr$ | 0.87 | 0.96 | 0.85 | 0.95 | 0.97 |
| Return point dilution | $C_6=Srp/Fr$ | 2.47 | 2.63 | 2.45 | 2.62 | 2.65 |

Table 5-4. Comparison of numerical and experimental coefficients for wave period 1.1 (s)

| Parameter | Normalized Equation | Present study | | | | Experimental results |
|---|---|---|---|---|---|---|
| | | RNG | Realizable | Nonlinear | LRR | |
| Terminal rise height | $C_1=Zt/DFr$ | 1.05 | 1.11 | 1.21 | 1.12 | 1.09 |
| Horizontal location of return point | $C_2=Xr/DFr$ | 1.73 | 2.01 | 2.145 | 1.90 | 1.99 |
| Vertical location of centerline peak | $C_3=Zc/DFr$ | 0.82 | 0.92 | 1.2 | 0.93 | 0.89 |
| Horizontal location of centerline peak | $C_4=Xc/DFr$ | 1.19 | 1.16 | 1.15 | 0.98 | 1.03 |
| Centerline peak dilution | $C_5=Sc/Fr$ | 0.91 | 1.01 | 0.89 | 0.99 | 1.02 |
| Return point dilution | $C_6=Srp/Fr$ | 2.60 | 2.73 | 2.64 | 2.75 | 2.78 |

Table 5-5. Comparison of numerical and experimental coefficients for wave period 1.3 (s)

| Parameter | Normalized Equation | Present study | | | | Experimental results |
|---|---|---|---|---|---|---|
| | | RNG | Realizable | Nonlinear | LRR | |
| Terminal rise height | $C_1=Zt/DFr$ | 0.91 | 0.96 | 1.08 | 0.95 | 0.94 |
| Horizontal location of return point | $C_2=Xr/DFr$ | 1.54 | 1.81 | 1.92 | 1.72 | 1.65 |
| Vertical location of centerline peak | $C_3=Zc/DFr$ | 0.74 | 0.81 | 0.89 | 0.80 | 0.78 |
| Horizontal location of centerline peak | $C_4=Xc/DFr$ | 1.00 | 1.04 | 1.03 | 0.94 | 0.92 |
| Centerline peak dilution | $C_5=Sc/Fr$ | 0.95 | 1.05 | 0.91 | 1.05 | 1.08 |

| | | | | | | |
|---|---|---|---|---|---|---|
| Return point dilution | $C_6$=*Srp/Fr* | 2.82 | 2.87 | 2.85 | 2.89 | 2.91 |

The centerline trajectories of the jets versus the horizontal distance in the presence of waves in the JDR region are plotted in Figures 5.7a–5.7d for all turbulence models. As the results correspond to the momentum-dominated area, the numbers are normalized by the length scales, $l_w$. As shown in Figures 5.7a–5.7d, the relationship between the jet centerline trajectory and the distance from the nozzle in the wavy environment can be approximated by the following relationship:

$$\frac{z_c}{l_w} = E_{wcl} \ \frac{x}{l_w} \tag{5.18}$$

where the $E_{wcl}$ coefficient for the jets is estimated for the RNG k-ε, realizable k-ε, nonlinear k-ε, and LRR models as equal to 0.85 and 0.96, 1.2, and 0.98 respectively. The results of these equations are consistent with the experimental results, and the $E_{wcl}$ for the experimental results was found to be 0.9.

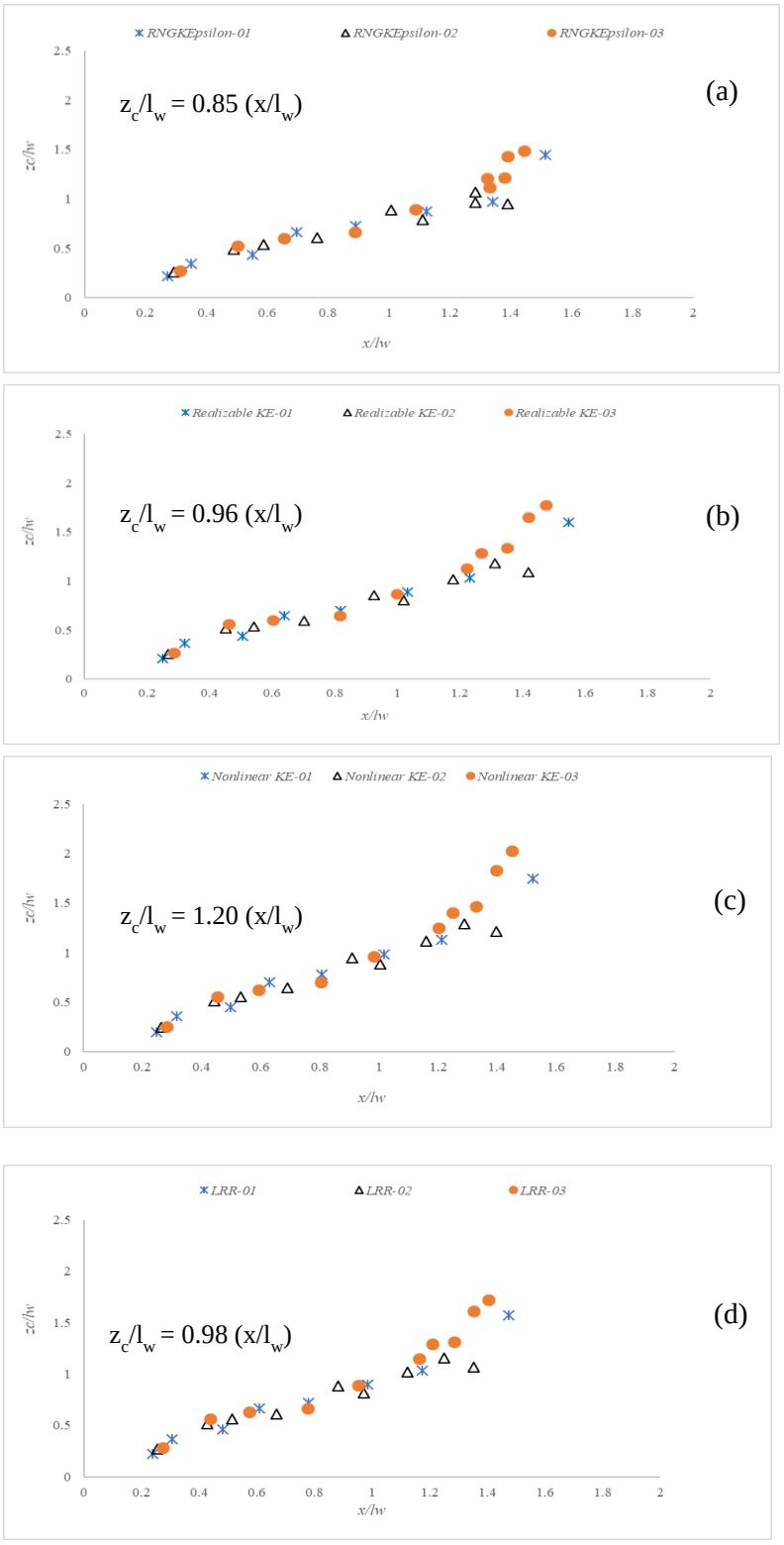


Figure 5-7. Dimensionless relationship between the centerline trajectory and the horizontal distance in the JDR region

To obtain a quantitative measurement of the difference between the experimental and numerical results, the RMSE and $R^2$ were calculated for the numbers presented in Figures 5.7 and summarized in Table 5.6. Looking at the RMSE and $R^2$ values, as well as the $E_{wcl}$ values of Equation (5.18) demonstrates that all these numerical models can provide reliable results, while the LRR and realizable k-ε models provide a better match with the experimental data.

Table 5-6. Error coefficient of calculated the centerline trajectory using various turbulence models in the JDR region

| Turbulence model | RMSE | $R^2$ |
|---|---|---|
| RNG k-ε | 0.13 | 0.93 |
| Realizable k-ε | 0.09 | 0.96 |
| Nonlinear k-ε | 0.14 | 0.91 |
| LRR | 0.07 | 0.97 |

### 5.3.3. Terminal Rise Height

The terminal rise height is the most critical parameter among the geometrical properties of the brine discharge, according to Shao and Law (2010). This is the point where the jet loses the vertical component of its initial momentum and as a result starts falling towards the bed. Therefore, it can be used to determine if the plume can be kept below the water surface.

Different methods are reported in literature for the determination of terminal rise height. Jirka (2008) used the visual boundary of captured flow images, but this method involves uncertainties due to the amount and type of dye used, recording instrument sensitivities, and other parameters. In this paper, the 3% level is used to derive the terminal rise height, which is the method used in the integral CORJET model and in the study performed by Shao and Law (2010). The terminal rise height, $Z_t$, for the concentration is normalized by the nozzle diameter and is plotted versus its distance from the nozzle in Figure 5.8. The initial nozzle height, $Z_0$, is subtracted from the given $Z_t$. The numerical results are compared with each other and with the experimental data. It can be seen that the numerical results of the different turbulence models are consistent with the experimental data. However, the nonlinear k-ε model overpredicts and RNG k-ε model slightly underpredicts the terminal rise height when compared to the other models.

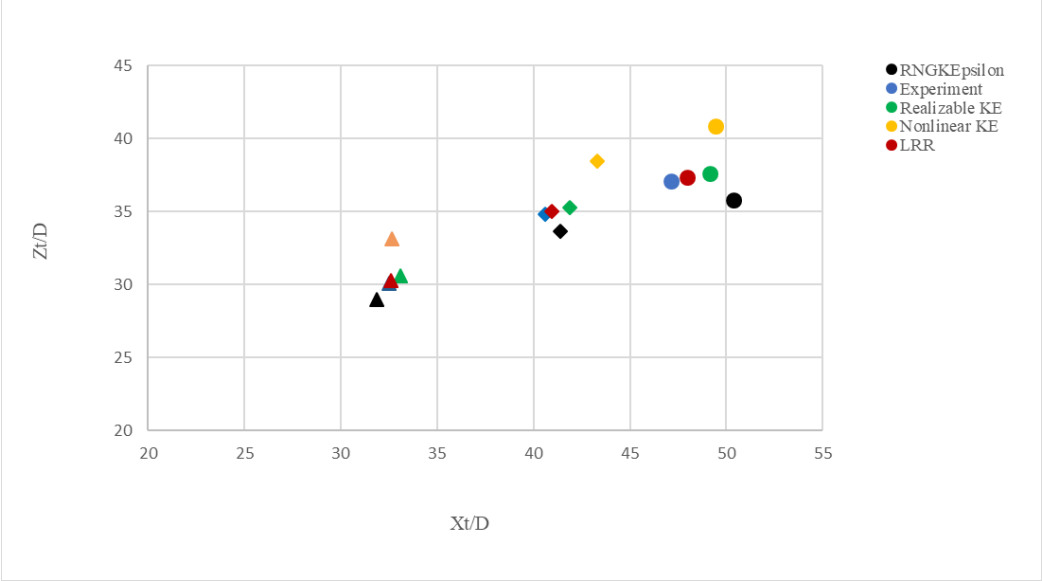


Figure 5-8. Normalized terminal rise height (circle symbol is associated to W-01, diamond symbols associated to W-02, and triangular symbols are associated to W-03)

To obtain a quantitative measurement of the difference between the experimental and numerical results for the terminal rise height ($Z_t$) and location ($X_t$), the RMSE and $R^2$ values were calculated and are summarized in Table 5.7 and Table 5.8. Based on these results, one can see that the LRR and realizable k-ε turbulence models provide a better match with the experimental data comparing to the RNG and the non-linear k-ε.

Table 5-7. Error coefficient of the calculated terminal rise height for various turbulence models

| Turbulence model | RMSE | $R^2$ |
|---|---|---|
| RNG k-ε | 1.16 | 0.17 |
| Realizable k-ε | 0.53 | 0.11 |
| Nonlinear k-ε | 3.52 | 0.24 |
| LRR | 0.21 | 0.078 |

Table 5-8. Error coefficient of the calculated terminal rise location for various turbulence models

| Turbulence model | RMSE | $R^2$ |
|---|---|---|
| RNG k-ε | 1.92 | 0.14 |
| Realizable k-ε | 1.39 | 0.13 |
| Nonlinear k-ε | 2.11 | 0. 22 |
| LRR | 0.5 | 0.09 |

Comparing the numerical results of the experiments W-01, W-02, W-03, one can see the influence of the waves on the geometry of the inclined negatively buoyant jet. It can be observed that, as the wave period increases, the terminal rise height decreases for all investigated conditions, which confirms the experimental results. This decrease is due to the fact that as the wave period increases, the wave orbital velocity also increases and wave hydrodynamics play a more important role on the interactions between the jet and the waves. Consequently, the increased dissipation of energy results in a decrease in the terminal rise height.

The terminal rise heights of the jets versus various wave periods are shown in Figures 5.9a-5.9d for all the models tested. The terminal rise heights are normalized by the length scales $z_w$ in order to consider buoyancy effects as well.

Based on the graphs shown in Figure 5.9, the relationship between the terminal rise height and the wave period can be approximated by the following equations:

$$\frac{z_t}{z_w} = E_{wt}(T^*)^{1.4} \qquad (5.19)$$

$$T^* = (Tu_w)/h \qquad (5.20)$$

where $T$ and $H$ are the wave period and wave height respectively. The values of the coefficient $E_{wt}$ for the jet is estimated by the RNG k-ε, realizable k-ε, nonlinear k-ε, and LRR models to be equal to 0.69,0.72, 0.84, and 0.74, respectively. The results of these equations are consistent with the experimental data, and the $E_{wt}$ value for the experimental data was found to be 1.35. As mentioned before, this important parameter can be used to evaluate, during the design stage, if the plume is fully submerged, especially for shallow waters.

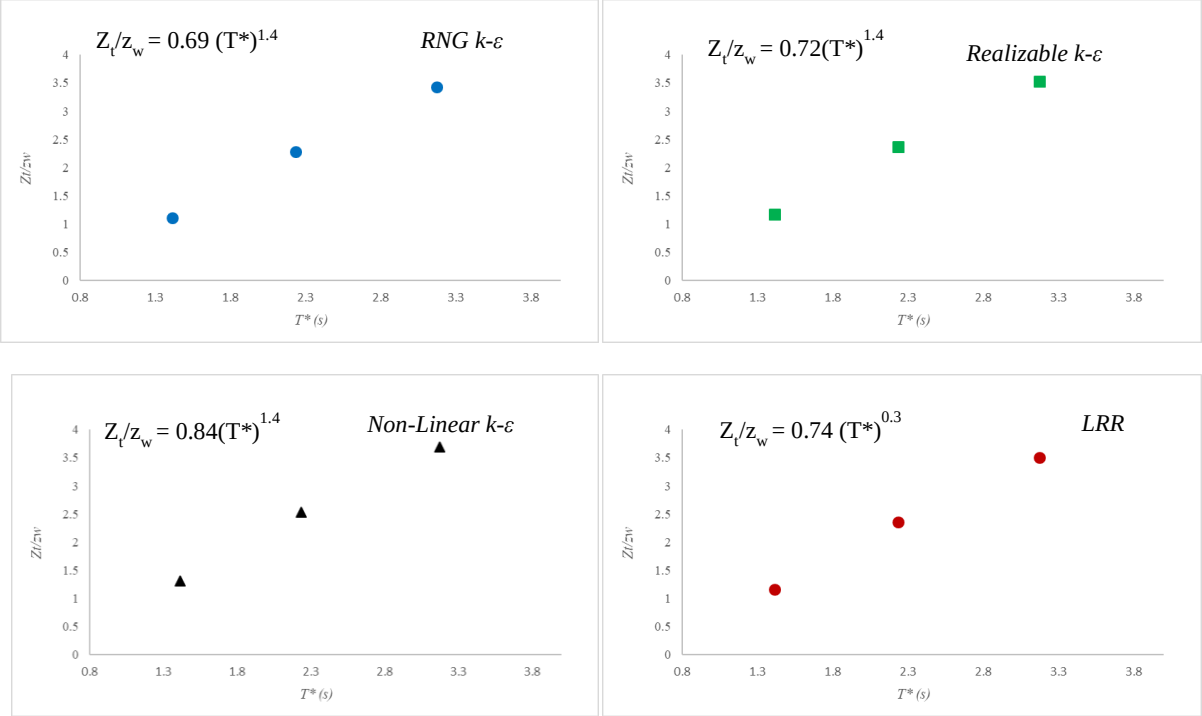


Figure 0-9. Dimensionless relationship between the terminal rise height and the wave periods for the jet

### 5.3.4. Minimum Dilution at Centerline Peak and Return Point

The minimum dilution at several points along the jet trajectory, including the centerline peak ($S_c$) and the return point ($S_{rp}$), are important in environmental impact assessments of jet dispersions. The dilution at the jet centerline peak was normalized herein by the densiometric Froude number, *Fr*, and is plotted against the wave period, for the different turbulence models, in Figure 5.10. As seen in this figure, the RNG k-ε and nonlinear k-ε numerical models underestimate the dilution value at the jet centerline peak, whereas the values predicted by the realizable k-ε and LRR numerical models are closer to the experimental data.

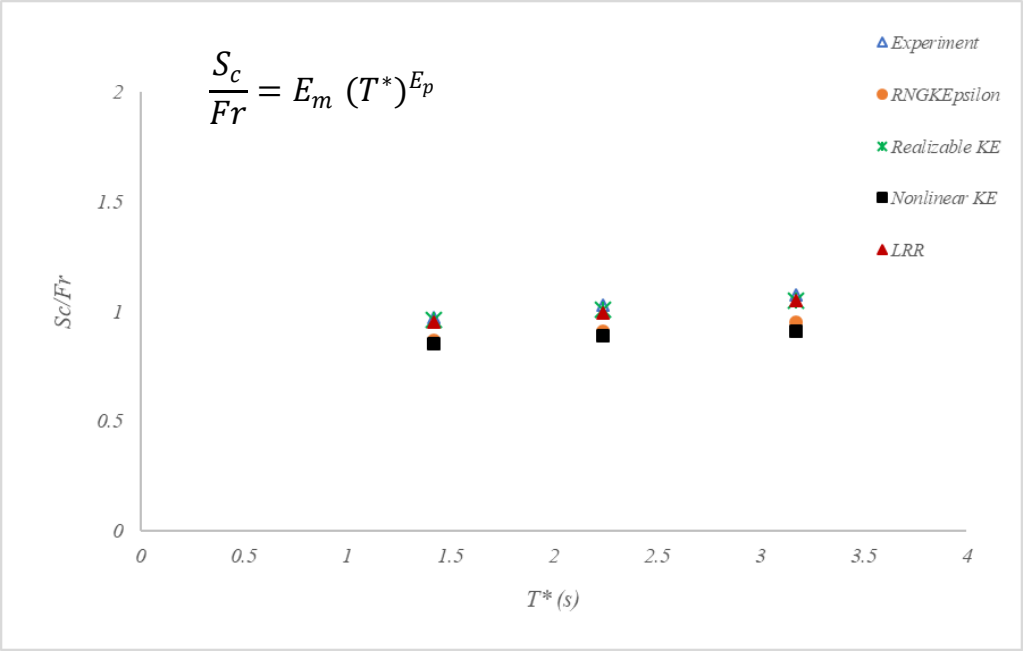


Figure 5-5-20. Minimum dilution at centerline peak

The $S_c/F_r$ ratio varies between 0.83 and 1.1 for the wave periods between 0.9 and 1.3 seconds. As the wave period increases, resulting in more intense interaction between the wave hydrodynamics and the jet, the $S_c/F_r$ ratio increased in all turbulence models. For all the investigated turbulence models, the relationship between $S_c/F_r$ and the wave periods can be approximated by the following equation:

$$\frac{S_c}{Fr} = E_m\ (T^*)^{E_p} \tag{5.21}$$

The estimated values for $E_m$ and $E_p$ for the RNG k-ε, realizable k-ε, nonlinear k-ε, and LRR models are presented in Table 5.9. The results of these equations are consistent with the experimental results.

Table 5-9. $E_m$ and $E_p$ values for four turbulence models and comparison with values from experimental results

| | Experiment | RNG k-e | Realizable k-e | Non-linear k-e | LRR |
|---|---|---|---|---|---|
| $E_m$ | 0.93 | 0.83 | 0.92 | 0.83 | 0.91 |
| $E_p$ | 0.12 | 0.11 | 0.11 | 0.08 | 0.12 |

In addition to the graphs and the coefficients in Equation (5.21), the RMSE and $R^2$ values were calculated, and again demonstrate the capability of the numerical models, especially the LRR and realizable k-ε models, to capture the effects of waves on dilution at the jet centerline peak.

Table 5-10. Error coefficient of calculated minimum dilution at centerline peak for the various turbulence models

| Turbulence model | RMSE | $R^2$ |
|---|---|---|
| RNG k-ε | 0.12 | 0.91 |
| Realizable k-ε | 0.018 | 0.97 |
| Nonlinear k-ε | 0.14 | 0.92 |
| LRR | 0.028 | 0.95 |

Another point of interest for dilution in designing outfall systems is the return point, where the dense jet returns to the source level. The minimum dilution at the return point ($S_{rp}$) is presented in Figure 5.11 for all turbulence models and the experimental data. As in the case of the dilution value at the jet centerline peak, the RNG k-ε and nonlinear k-ε numerical models underpredict the dilution value at the return point. It is also noteworthy that the realizable k-ε and LRR models are in better agreement with the experimental data than the other turbulence models.

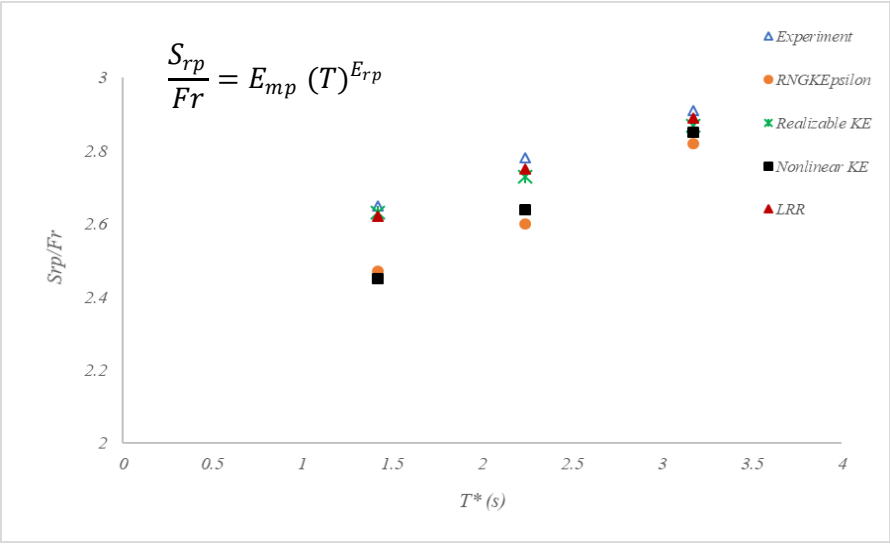


Figure 0-11. Minimum dilution at the return point as a function of wave period

In agreement with the experimental analysis and as shown in Figure 5.11, the $S_{rp}/F_r$ ratio increases as the wave period increases. For the tested conditions, the relationship between $S_{rp}/F_r$ and the wave periods can be approximated by the following equation:

$$\frac{S_{rp}}{Fr} = E_{mp}\,(T^*)^{E_{rp}} \qquad (5.22)$$

The estimated values for $E_{mp}$ and $E_{rp}$ for the RNG k-ε, realizable k-ε, nonlinear k-ε, and LRR models are presented in Table 5.11. These equations are consistent with the experimental results. As the design of a marine outfall centers on the dilution required to meet the relevant guidelines, these empirical equations can be used to optimize the outfall location. Based on the estimated coefficient values ($E_{rm}$ and $E_{rp}$), the realizable k-ε and LRR models are in best agreement with the experimental values.

Table 5-11. $E_{mp}$ and $E_{rp}$ values for the four turbulence models and comparison with values from experimental results

| | Experiment | RNG k-e | Realizable k-e | Non-linear k-e | LRR |
|---|---|---|---|---|---|
| $E_{rm}$ | 2.54 | 2.32 | 2.52 | 2.9 | 2.51 |
| $E_{rp}$ | 0.12 | 0.15 | 0.11 | 0.18 | 0.12 |

In addition to the graphs and the coefficient in Equation (5.22), the RMSE and $R^2$ values are shown in Table 5.12. The results show that the realizable k-ε and LRR models are in better agreement with the experimental results, with the LRR being slightly better than the realizable k-ε model.

Table 5-12. Error coefficient of calculated minimum dilution at the return point for the various turbulence models

| Turbulence model | RMSE | $R^2$ |
|---|---|---|
| RNG k-ε | 0.16 | 0.86 |
| Realizable k-ε | 0.038 | 0.96 |
| Nonlinear k-ε | 0.14 | 0.88 |
| LRR | 0.027 | 0.97 |

### 5.3.5. Cross-sectional Velocity Profile

In order to better evaluate the inclined dense jet behavior in a wave environment, the normalized cross sectional profiles of $U/U_c$ for the turbulence models are plotted versus $r/b_u$ in Figure 5.12 for the same cross-sections, where $U$ is the velocity along the cross-sections, $U_c$ is the maximum velocity along the cross-sections, $r$ is the radial distance, and $b_u$ is the velocity spread width, again using the $e^{-1}$ notation (Shao, 2010). The numerical results of each turbulence model are compared to the experimental data. The velocity profiles are extracted along several cross-sections (*s/D=5, s/D=12, and s/D=15*).

RNG KEpsilon

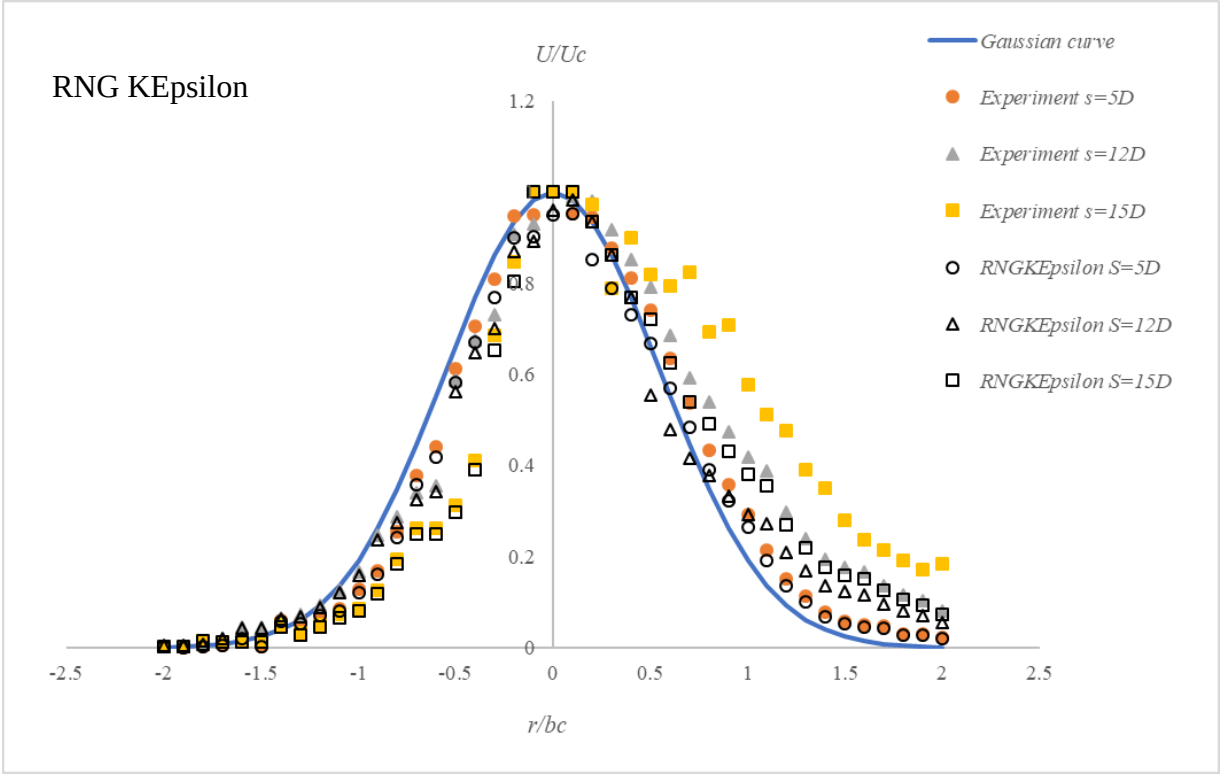


Realizable KE

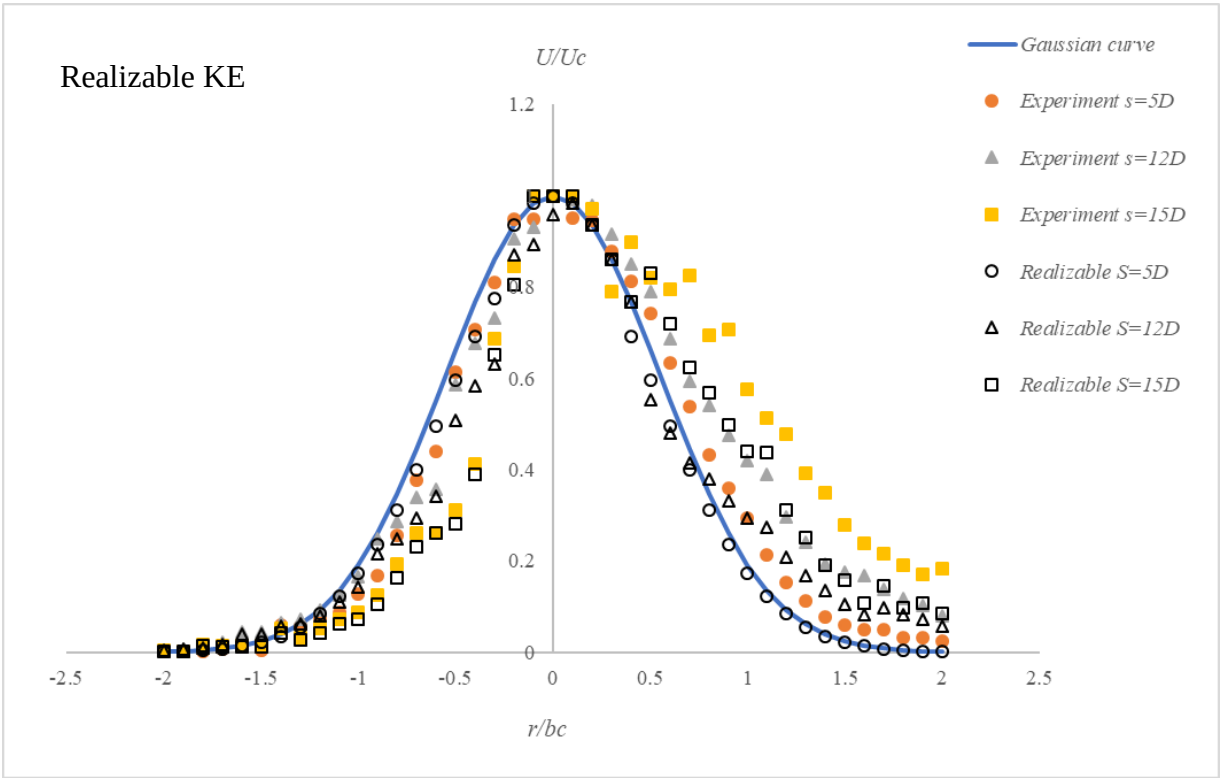

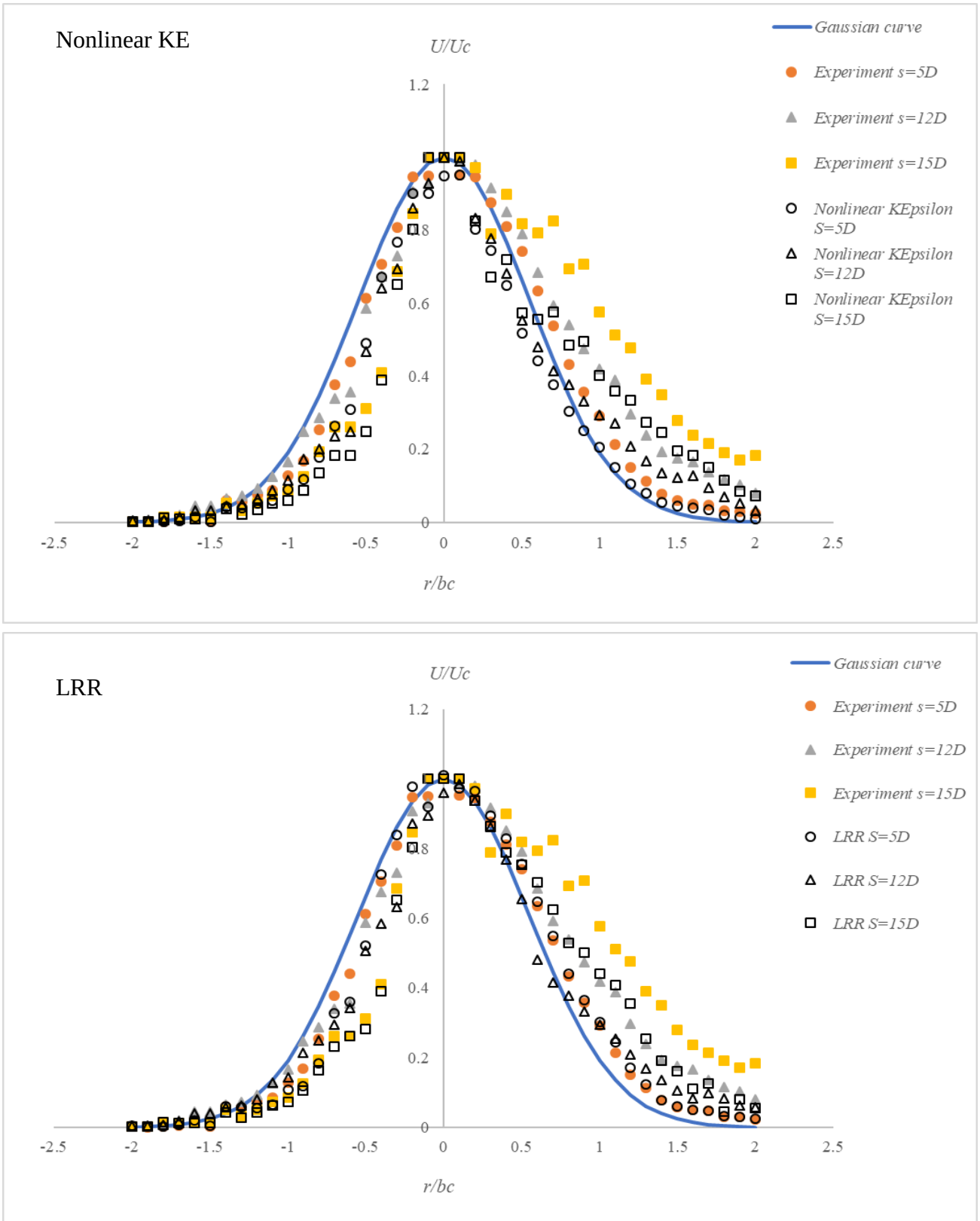


Figure 5-32. Normalized velocity profiles at various downstream cross-sections for 45° for W-01

As shown in Figure 5.12, a symmetric Gaussian distribution is obtained by all the turbulence models investigated. Model predictions are in good agreement with the experimental results for the top half of the jet. However, while it seems that all the models' predictions slightly underestimate the velocity of the lower half of the jet, the RNG k-ε, realizable k-ε, and LRR models show better agreement with the experimental results for the upper half compared to the nonlinear k-ε model. This is more evident for *s/D*=12 and *s/D*=15. The results of the calculated RMSE and $R^2$ errors for the normalized velocity in the upper half are presented in Table 5.13, which also proves that the nonlinear k-ε model has less agreement with the experimental results among the other models.

Table 5-13. Error coefficient of calculated normalized velocity for the upper half of the three cross-sections for the various turbulence models

| Turbulence model | *s/D*=5 | | *s/D*=12 | | *s/D*=15 | |
|---|---|---|---|---|---|---|
| | RMSE | $R^2$ | RMSE | $R^2$ | RMSE | $R^2$ |
| RNG k-ε | 0.029 | 0.96 | 0.040 | 0.92 | 0.017 | 0.98 |
| Realizable k-ε | 0.031 | 0.95 | 0.041 | 0.91 | 0.019 | 0.97 |
| Nonlinear k-ε | 0.056 | 0.89 | 0.054 | 0.88 | 0.036 | 0.91 |
| LRR | 0.037 | 0.92 | 0.040 | 0.91 | 0.018 | 0.97 |

### 5.4. Discussion and Conclusions

The main objective of this study was to evaluate the performance of numerical models in the simulation of inclined dense jets in wave ambient water by numerically investigating the geometric, concentration (dilution), and velocity characteristics of such jets. An experimental investigation was performed earlier by the authors and its results were used to verify the results of the numerical simulations. A negatively inclined dense jet with an angle of 45 degrees was selected to be modeled using the OpenFOAM CFD toolbox. The solver interFoam within the OpenFOAM toolbox was modified by adding buoyancy effects and the density variation caused by salinity concentration of the brine, as well as by adding an advection-diffusion transport equation for salinity. The wave characteristics were selected to simulate a typical Mediterranean wave condition. Three different wave periods were considered in this study, while the wave height was kept constant in order to see the effects of changing wave periods on the results, as had also been

investigated in the experimental program. In order to evaluate the accuracy and effect of using different turbulence models, four of them (RNG k-ε, realizable k-ε, LRR, and nonlinear k-ε) have been selected and further used in the numerical model. The governing equations were solved using the finite volume method on an unstructured, refined mesh grid system. The numerical results were compared to each other, as well as to the experimental data.

The comparison between the developed numerical models and the experimental data showed all the models investigated provided reliable results. However, in terms of the geometrical properties, jet dilution, and velocity profile, the LRR and realizable k–ε performed the best. A significant advantage of the LRR is that the model directly calculates Reynolds stresses by solving an equation for each Reynolds stress, so it is expected to be more accurate but also more computationally expensive. In the realizable k–ε model, the turbulent viscosity is calculated using an improved method. The model uses a non-constant value for dynamic viscosity coefficient ($c_\mu$) rather than assuming that it is constant – hence, this considers, to some extent, the anisotropy of turbulence. The RNG k-ε turbulence model differs from the realizable k-ε in the method of calculating the turbulent viscosity. The RNG k-ε model also assumes that the dynamic viscosity coefficient ($c_\mu$) is constant - this is not always true and may be the reason for the poor performance in the present case. It should be noted that the Realizable k-ε model is less computationally expensive, easier to implement, and has a better performance in numerical convergence than the more advanced turbulence methods such as LRR. As such, the use of the Realizable k-ε model for modeling outfall discharges is deemed more practical and economical and can be considered as a good compromise between accuracy and computational cost.

The conclusions of the present study are:

- The geometrical properties of the jet, including the terminal rise height and the centerline peak height, were studied using four turbulence models. In general, the realizable k-ε and LRR models' numerical results were in better agreement with the experimental data when compared to the RNG k-ε and nonlinear k-ε turbulence models, which showed more discrepancies compared to the experimental data.
- The jet dilution, as the key parameter in designing ocean outfall systems, was calculated for both the centerline peak and the return point. The RNG k-ε and nonlinear k-ε turbulence models underestimated of the dilution values, while the realizable k-ε and LRR models'

numerical values were in better agreement with the experimental results, with slight underestimation. Both models followed the same pattern (i.e., better agreement with experimental data), with the standard k–ε model performing slightly better than the realizable k–ε.

- An experimental study previously conducted by the authors as a result of more accurate calculations of dilution using LIF-PIV techniques led to the derivation of empirical formulae relating the minimum dilution at the centerline peak and return point to the Froude numbers and wave periods. Those relationships were also investigated in this study for all four turbulence models in order to verify if they could be captured numerically. The results showed a good agreement between the equations derived from the realizable k-ε and LRR models' numerical results and the ones from the experimental data. These formulae can be used in environmental impact assessment studies of outfalls and to optimize their locations and configurations. As such, engineers can configure the outfall designs to maximize dilution in the near field.

- The cross-sectional velocity profiles showed a Gaussian pattern for the top half of the jet. For the top half of the jet, there is a good agreement between the experimental data and all the numerical models, while for the lower half, the numerical models underpredicted the velocity compared to the experimental results. The lower half loses the Gaussian pattern as it goes farther downstream, as was also the case in the experimental study previously conducted by the authors as well as in other numerical studies on stagnant ambient water (Gildeh et al., 2014).

# 6. Summary and Concluding Remarks

This study was aimed at improving the understanding of the mixing patterns of different outfall systems with densities different from those of the receiving environment, which could be a river or an ocean, as well as the mixing patterns of two water bodies with different densities, and the numerical simulation of those processes.

In the first part of this study:

- An extension of a well-balanced central upwind scheme for variable density shallow water flow equations was introduced for triangular grids. Using such grids could be advantageous or even unavoidable in practice when dealing with complicated geometries.
- A Eulerian approach which is computationally less expensive than interface tracking technique was employed in this study. A strong stability preserving (SSP) Runge–Kutta (RK) time discretization method known as the Shu–Osher method was used because of its increased stability and higher temporal accuracy.
- In addition, to decrease the oscillations caused by probable phase errors, third-order spatial discretization with a slope limiter function was also applied in the solution.
- The positivity preserving property of the method was also achieved. The accuracy of the suggested method and its different properties were demonstrated for a number of well-known benchmark test cases. The proposed scheme is the first well balanced, positivity preserving scheme in the literature in the context of variable density flows.

In the second part of the study:

1. The mixing process of a two-layer flow over a dune was numerically simulated using LES with the Smagorinsky SGS models.
2. To assess the accuracy of the simulation, modeled results were compared with the experimental measurements performed using PIV-LIF techniques at University of A Coruña, Spain, by the candidate.
3. A numerical RANS simulation was also performed and included for comparison in order to demonstrate the superiority of the LES method. LES is computationally more expensive than the RANS approach; however, it resolves large turbulent motions of the

flow and models only the smaller scales, so it is able to capture the unsteadiness of the flow, which is the main goal of this research.

4. The comparisons covered the velocity and density distribution, shear layer thickness, Bulk Richardson number, and entrainment rate. The LES model was able to reproduce shear interface instabilities and fulfill the main goal of the study, as the LES predictions were in reasonable agreement with the experimental measurements.
5. The RANS approach, on the other hand, could produce good results up to the points that instabilities start to form. However, it could not reproduce the small-scale instabilities of the flow field, and this led to an inadequate description of the phenomena and generated results with more errors relative to the measured results.

In the third part of the study:

- The interaction between negatively buoyant jet and regular wave was experimentally investigated. The experiments were conducted in a co-directional wave-current flume at CITEEC-UDC, the Water and Environmental Engineering Group (GEAMA) at the University of A Coruña, Spain. The wave characteristics and jet angles were varied in the experiments and the Particle Image Velocimetry (PIV) technique and full-field Laser Induced Fluorescence (LIF) technique were used to investigate the velocity fields and the diluting effect of surface waves on buoyant plumes.
- The experimental results showed that the wave motion affects the inclined negatively buoyant jet geometry, resulting in jet rotation and increasing the jet width. This can result in a decrease of the maximum height and centerline peak of the plume. Compared to the stagnant water conditions, the jet rotation decreased the terminal rise height and centerline peak in wave environment, whereas an increase in wave period, decreased the terminal rise height and centerline peak. Empirical formulae for predicting jet terminal rise height were proposed for wave-only and wave-current conditions. These equations are of practical value for the design of brine discharge systems, as full submergence of the brine plume is generally targeted as a design requirement.
- The trajectories of dense jets in stagnant ambient water are longer compared to jets in wave conditions. Also, increasing the wave period decreases the length of the trajectory, while

the wave height remains almost constant. Empirical formulae for predicting jet centerline trajectories were proposed for wave-only and wave-current conditions.

- Using the mean concentration field obtained from the LIF images, it was found that jet dilution along the centerline increases with increases in the wave period, while the jet width does not significantly increase. Also, under wave effects, the jet width was significantly larger than that in the stagnant environment, and thus the dilution of the jet also increased.
- The minimum dilution at specific locations inside or near the jet is important for design purposes, as the design of a marine outfall is based on the dilution required to meet the relevant environmental guidelines. More accurate calculations of the dilution obtained in this study led to the derivation of empirical formulae relating the minimum dilution at centerline peak and return point (for wave environment) to the Froude numbers and wave periods, which can be used in environmental impact assessments of outfalls in industry and to optimize the location and configuration of marine outfalls. Thus, an engineer could configure the outfall design to maximize dilution in the near field.
- The cross-sectional velocity profile in the jet was also investigated, and the velocity profile was found to approximately match Gaussian profiles only in the top half of the jet, while the lower part of the jet showed a flatter velocity profile, similar to the no-wave case.

In the fourth part of the study:

- The effects of waves on the mixing and dispersion characteristics of inclined negatively buoyant jets, presented in the experimental research in Chapter 4, were numerically investigated by the candidate using a finite volume model (OpenFOAM).
- Four turbulence models, the RNG k-ε, realizable k-ε, LRR, and nonlinear k-ε were investigated to assess the accuracy of each of them in predicting effluent discharges in submerged outfalls.
- Investigating the geometrical properties of the jet, including terminal rise height and centerline peak height, showed that the realizable k-ε and LRR models' numerical results were in better agreement with the experimental data compared to the RNG k-ε and nonlinear k-ε turbulence models. The nonlinear k-ε turbulence model showed more discrepancies with respect to the experimental data when compared to the other models.

- The dilution was calculated for both the centerline peak and the return point. The RNG k-ε and nonlinear k-ε turbulence models underestimated the dilution, while the realizable k-ε and LRR models' numerical values were in better agreement with the experimental results, with slight underestimation.
- The empirical formulae from the experimental study were also studied for the four turbulence models used in order to investigate if the same relationships could be captured numerically. The results showed good agreement between the equations derived from the realizable k-ε and LRR models' numerical results and the ones from the experiments.
- The cross-sectional velocity profiles showed a Gaussian pattern for the top half of the jet. Good agreement was observed between the experimental data and all numerical models for the top half, while for the lower half, the numerical models underpredicted the velocity compared to the experimental results. The lower half loses the Gaussian pattern as it propagates farther downstream, as was also the case in the experimental study.

### 6.1. Recommendations for Future Studies

The following recommendations are proposed for future studies on the numerical modeling of density currents:

- For the 3D numerical modeling of flows of liquids with variable densities for two-layer exchange flows, LES and RANS have been applied as turbulence models in this study. Another interesting approach would be using detached-eddy simulation (DES), which is a hybrid RANS-LES method and combines the benefits of LES for resolving large turbulent structures away from the wall with the benefits of RANS near the wall, where the turbulent eddies are too small to resolve.
- Several numerical models have been applied for the cases considered herein. OpenFOAM usually contains the latest version of the turbulence models; however, it is useful if one searches for new ideas that may occur for turbulence modeling in the future and implement those ideas to the established models. This in itself would represent a good research line to investigate turbulence models within OpenFOAM.

- For flows of liquids with variable densities in the presence of waves, more jet inclination angles should be modelled to investigate their effects. For example, steeper jet angles could be modeled for regions with deeper ambient water.
- A wave-current ambient environment should also be numerically modeled and the results be compared to the experimental data obtained in Chapter 4 of this study.

# References


A.A. Abdel-Rahman, and M.A. Eleshaky, An experimental investigation of a plane jet in a wavy crossflow. *Proc. of the 4th ASME/JSME Joint Fluids Eng. Conf.*, Honolulu, Hawaii. (2003).

O. Abessi, and P.J.W. Roberts, Dense jet discharges in shallow water. *J. Hydraul. Eng.*, 10.1061/(ASCE)HY.1943-7900.0001057, 04015033 (2015).

O. Abessi, and P.J.W. Roberts, Multiport diffusers for dense discharges. *J. Hydraul. Eng.*, 10.1061/(ASCE) HY.1943-7900 .0000882, 04014032 (2014).

M. B. Abbott, Computational Hydraulics. Ashgate Publishing Co., Brookfield, Ct. (1979).

F. Alcrudo, and P. García-Navarro, A high-resolution Godunov-type scheme in finite volumes for the 2D shallow-water equations. *Int. J. Numer. Methods Fluids*; **16**:489–505 (1993).

H. Alfaifi, A. Mohammadian, H. K. Gildeh, A. Gharavi, Experimental and numerical study of the characteristics of thermal and nonthermal offset buoyant jets discharged into stagnant water. *Desalination and Water Treatment Journal*, 141, 171–186 (2019).

J. Anta, I. Mera, E. Peña, and A. Louro, Two-layer exchange flows over a dune: effect of large-scale bottom roughness. *Journal of Visualization* 14:99-101. doi 10.1007/s12650-011-0078-x (2011a).

J. Anta, E. Peña, A. Louro, and I. Mera, Combined PIV-LIF measurements of two-layer flows: analysis of mixing processes over different bottom macro-roughness. *7th International Symposium on Stratified Flows*, Rome, Italy (2011b).

J. Anta, M.A. Regueiro-Picallo, L. Cea, and E. Peña, Combined PIV-LIF measurements and numerical modeling of stratified flows over a dune and an array of dunes. *River Flow* ISBN 978-1-138-02913-2 (2016)

L. Armi, The hydraulics of two flowing layers with different densities. *J. Fluid Mech.*, 163, 27–58 (1986).

L. Armi, and D. M. Farmer, The flow of Mediterranean water through the Strait of Gibraltar. *Prog. Oceanogr.*, 21, 1–105 (1988).

E. Audusse, F. Bouchut, M.-O. Bristeau, R. Klein and B. Perthame, A fast and stable well-balanced scheme with hydrostatic reconstruction for shallow water flows. *SIAM Journal of Science Computational* 25 2050–2065 (2004).

A. Bermúdez, M. E. Vázquez, Upwind mehotd for hyperbolic conservation laws with source terms. *Journal of Computational Fluids.* 23 1049-1071 (1994).

T. Bleninger, A. Niepelt, G.H. Jirka Desalination plant discharge calculator. Paper BD 180 for EDS Congress, Baden, Germany (2009).

A. Bollermann, G. Chen, A. Kurganov and S. Noelle, A Well-Balanced Reconstruction of Wet/Dry Fronts for the Shallow Water Equations, *Journal of Scientific Computing* 56(2) (2013).

J. P. Boris, and D. L. Book, Flux-Corrected Transport III. Minimal Error FCT Algorithms. *J. Comput. Phys.;* 20:397-431 (1976).

J. Boussinesq, Essai sur la théorie des eaux courantes. *Mem. prés. div. Sav. Acad. Sci. Inst. Fr.*, 23:1–680 (1877).

L. Brice, C. Yarko Niño and M. CristiaN. Escauriaza, Finite volume modeling of variable density shallow-water flow equations for a well-mixed estuary: application to the Río Maipo estuary in central Chile, *Journal of Hydraulic Research,* 43:4 339-350 (2010).

S. Bryson, Y. Epshteyn, A. Kurganov and G. Petrova. Well-balanced positivity preserving central-upwind scheme on triangular grids for the Saint-Venant system, ESAIM: *Mathematical Modelling and Numerical Analysis*, (2010).

A. Chertock, S. Cui, A. Kurganov and T.Wu, Well-balanced positivity preserving central-upwind scheme for the shallow water system with friction terms, *International Journal for numerical methods in fluids.* 78:355–383 (2015).

A. Chertock, A. Kurganov and Y. Liu, Central-upwind schemes for the system of shallow water equations with horizontal temperature gradients, *Journal of Numerische Mathematik.* 127:595–639 (2014).

D.A Chin, Influence of Surface Waves on Outfall Dilution, *J. Waterway, Port, Coastal, Ocean Eng*.114(3), 331–345 (1987).

D. A. Chin, Model of buoyant-jet-surface-wave interaction. *J. Waterway Port Coastal Ocean Eng*., 114, 331–345 (1988).

C.P. Chu, Mixing of turbulent advected line puffs. Ph.D. Thesis, University of Hong Kong (1996).

J.M. Chyan, and H.H. Hwung, On the interaction of a turbulent jet with waves. *J. Hydraul. Res.*, 31:791-810 (1993).

B. Cockburn, and C. W. Shu, Nonlinearly stable compact schemes for shock calculations. *SIAM J. Numer. Anal.* 31:607–627(1994).

G. Constantinescu, LES of lock-exchange compositional gravity currents: a brief review of some recent results. *Environ Fluid Mech* 14:295–317. doi 10.1007/s10652-013-9289-0 (2014).

F. Costa, Physical model study of mixing processes of hyperdense spills and gravity currents. Ph.D. Thesis, University of A Coruña. (in Spanish) (2016).

W. B. Dade, J. R. Lister, and H. E. Huppert, Fine-sediment deposition from gravity surges on uniform slopes. *J. Sediment. Res.*, 64(3a), 423–432 (1994).

M.A. Darwish, R. Mohtar, Qatar water challenges, *Desalination and Water Treatment*, 51:1-3 (2013).

R. Dean, and R. A. Dalrymple, *Water Wave Mechanics for Engineers and Scientists*. Prentice-Hall, Englewood Cliffs, NJ (1984).

J. J. Dronkers. *Tidal Computations in Rivers and Coastal Waters.* North-Holland, New York. (1964).

S. K. Dube, P. C. Sinha and G. D. Roy. The numerical simulation of storm surges along the Bangladesh coast. *Dyn. Atmos. Oceans;* **9**:121–133(1985).

M.E. Elhaggag, M.H. Elgamal, M.I. Farouk. Experimental and numerical investigation of desalination plant outfalls in limited disposal areas, J Environ Protec 2:828-839 (2011).

T. H. Ellison, and J. S. Turner, Turbulent entrainment in stratified flows. *J. Fluid Mech*. 6, 423–448 (1959).

R. A. Falconer, An introduction to nearly horizontal flows, *Coastal, Estuarial and Harbour Engineers Reference Book (Abbott, M. B. & Price, W. A., eds). E & FNSpon Ltd.*, (1993).

E. Ferbo. Evaluation of RANS turbulence models for flow problems with significant impact of boundary layers. Technical report, FOI, Swedish Defence Research Agency (2010).

H. J. S. Fernando, Turbulent mixing in stratified fluids. *Annu. Rev. Fluid Mech.* 23, 455–493 (1991).

S. Ferrari, G. Querzoli, Laboratory experiments on the interaction between inclined negatively buoyant jets and regular waves, *EPJ Web of Conferences*, 92, 02018 (2015).

H.B. Fischer, E.J. List, R.C.Y. Koh, J. Imberger, N.H. Brooks. Mixing in inland and coastal waters." Academic Press (1979).

H. R. S. Fouli, An experimental study of interfacial waves and instabilities in exchange flows over a smooth sill. PhD thesis, Department of Civil and Environmental Engineering, Edmonton, University of Alberta (2006).

H. R. Fouli, D. Z. Zhu, Interfacial waves in two-layer exchange flows downslope of a bottom sill. *J. Fluid Mech*. 680, 194–224 (2011).

L. Fraccarollo and A. Armanini. A semi-analytical solution for the dam-break problem over a movable bed. Proc., *European Concerted Action on Dam-Break Modeling*. 145–152 (1998).

J. M. Gallardo, M. J. Castro, C. Parés and J. M. González-Vida, On a well-balanced high-order finite volume scheme for the shallow water equations with bottom topography and dry areas, *Journal of Computational Physics* 227(1) 574-601 (2007).

R. W. Garvine, Estuary plumes and fronts in shelf waters: A layer model. *J. Phys. Oceanogr*. 17:1877–1896 (1987).

D. L. George, Augmented Riemann solvers for the shallow water equations over variable topography with steady states and inundation. *J. Comput. Phys.* 227:3089-3113 (2008).

M. Germano, U. Piomelli, P. Moin, W.H. Cabot, A dynamic subgrid-scale eddy viscosity model. *Phys Fluids* A 3(7):1760 -1765 (1991).

H.K. Gildeh, A. Mohammadian, I. Nistor, CFD modeling and analysis of the behavior of 30 and 45 inclined dense jets—New numerical insights. *J. Appl. Water Eng*. Res 4.2: 1-16 (2015).

H. K., Gildeh, A. Mohammadian, I. Nistor, and H. Qiblawey. Numerical modeling of turbulent buoyant wall jets in stationary ambient water. *J. Hydraul. Eng*., 10.1061/(ASCE)HY.1943-7900.0000871, 04014012, (2014).

H. K., Gildeh, A. Mohammadian, I. Nistor, and H. Qiblawey. Numerical modeling of 30° and 45° inclined dense turbulent jets in stationary ambient." *Environ. Fluid Mech*., 15(3), 537–562 (2015).

S. P. Haigh, and G. A. Lawrence, Symmetric and nonsymmetric Holmboe instabilities in an inviscid flow. *Phys. Fluids* 11, 1459-1468 (1999).

P. F. Hamblin, and G. A. Lawrence, Exchange flows between Hamilton Harbour and Lake Ontario. Proc. Annual Conf. of Canadian Society for Civil Engineering, V, 140–148 (1990).

A. Harten, High Resolution Schemes for Hyperbolic Conservation Laws. *J. Comput. Phys.* **49**:357-293 (1983).

M. C. Hendershott, Long waves and ocean tides. *Evolution of Physical Oceanography. B. A. Warren and C. Wunsch, Eds., The MIT Press,* 292–341(1981).

S.C. Hsiao, T.W. Hsu, J.F. Lin, K.A. Chang, J. Mean and Turbulence Properties of a Neutrally Buoyant Round Jet in a Wave Environment. Waterway, Port, Coastal, Ocean Eng. 137(3), 109–122 (2011).

T. Y. Hsieh and J. C. Yang, Investigation on the suitability of two-dimensional depth-averaged models for bend-flow simulation. *Journal of Hydraulic Engineering*, 129(8) 597–612 (2003).

J.M. Chyan, and H.H Hwung, On the interaction of a turbulent jet with waves.'' *J. Hydraul. Res.*, 31, 791–810 (1993).

M.S. Isaacson, R.C.Y. Koh, and N.H. Brooks, Plume Dilution for Diffusers with Multi-Port Risers. *J. Hydraul. Eng.*, 109:199-219 (1983).

P. Jawahar and H. Kamath. A high-resolution procedure for Euler and Navier-Stokes computations on unstructured grids. *J. Comput. Phys*., 164(1):165–203 (2000).

M. Jin, D. L. Fread, 1D routing of mud/debris flow using NWS FLDWAV model. Debris Flow Hazard Mitigation: Mech., Pred. and Assessment, *ASCE. (1997).*

G.H. Kheirkhah, A. Mohammadian, I. Nistor, and H. Qiblawey, Numerical modeling of 30◦ and 45◦ inclined dense turbulent jets in stationary ambient. *Environ. Fluid Mech*. 15:537–562 (2015).

D.G. Kim, H.Y. Cho. Modeling the buoyant flow of heated water discharged from surface and submerged side outfalls in shallow and keep water with a cross flow. *J Environ. Fluid Mech*. 6:501-518 (2006).

B. C. Kneller, S. J. Bennett, and W. D. McCaffrey, Velocity structure, turbulence and fluid stresses in experimental gravity currents. *J. Geophys. Res.*, 104(C3), 5381–5391 (1999).

R. Koole, C. Swan, Measurements of a 2-D non-buoyant jet in a wave environment, *Coastal Engineerig Journal*, 24, 151-169 (1994).

A. Kurganov and G. Petrova, Central-upwind schemes on triangular grids for hyperbolic systems of conservation laws. *Numerical Methods for Partial Differential Equation Journal*, 21 536–552 (2005).

A. Kurganov and G. Petrova, A second-order well-balanced positivity preserving scheme for the Saint-Venant system. *Journal of Communications in Mathematical Science* 5 133–160 (2007).

C.C.K. Lai, and J.H.W. Lee, Mixing of inclined dense jets in stationary ambient. *J. Hydro-env. Res*. 6: 9-28 (2012).

D. Laigle, P. Coussot. Numerical modelling of mudflows. *Journal of Hydraulic Engineering*, 123(7) 617–623 (1997).

H. Lamb, Hydrodynamics. 6th ed., Dover, New York (1932).

G. A. Lawrence, On the hydraulics of Boussinesq and non-Boussinesq two-layer flows. J. Fluid Mech. 215, 457 (1990).

G. A. Lawrence, The hydraulics of steady two-layer flow over a fixed obstacle. *J. Fluid Mech.* 254, 605–633 (1993).

P. S. Laplace, Recherches sur plusieur points du système du monde. Mém. Acad. r. Sci.; **88**:75–182 (1775)

P. D. Lax, and B. Wenedroff, Systems of Conservation Laws. *Comm. Pure Appl. Math.* **13**:217–237(1960).

J.H.W. Lee, and P. Neville-Jones, Initial dilution of horizontal jet in crossflow, *J. Hydraul. Eng*., 1987, 113(5): 615-629

R. J. LeVeque, Wave propagation algorithms for multi-dimensional hyperbolic systems. *J. Comput. Phys.* 131:327-335 (1997).

Q. Liang, F. Marche. Numerical resolution of well-balanced shallow water equations with complex source terms. *Advances in Water Resources,* 32 873–884 (2009).

J. A. Liggett, *Fluid Mechanics.* McGraw-Hill, New York, NY, USA (1994).

D.K. Lily, A proposed modification of the germano-subgrid-scale closure method. *Phys Fluids A* 4(3):633–635 (1992).

J.F. Lin, S.C. Hsiao, T.W. Hsu, K.A. Chang, Buoyancy Effect on Turbulent Round Jet under Regular Waves. *J. Waterway, Port, Coastal, Ocean Eng*. 139, 190-208 (2013).

E.J. List, Turbulent Jets and Plumes. *Annual Review of Fluid Mechanics,*14, 189-212. http://dx.doi.org/10.1146/annurev.fl.14.010182.001201(1982)

R.W. MacCormack, The Effect of Viscosity in Hypervelocity Impact Cratering. *AIAA Paper*: 69-354 (1969).

I.K. Madni, and S.Z. Ahmad, Prediction of turbulent, axisymmetric, dense jets discharged to quiescent ambient. *Math. Comput. Model.* 12(3):363–370 (1989).

D. M. McDowell, and B. A. O'Connor, Hydraulic Behaviour of Estuaries. Macmillan Press, London (1977).

I. Mera, J. Anta, A. Louro, and E Peña, Parameter sensitivity analysis of the performance of Galician submarine outfalls: physical modeling. *Proc. 6$^{th}$ Int. Sym. Environ. Hydraul.*, Athens, 583-588 (2010).

F.J. Millero, A. Poisson. International one-atmosphere equation of state of sea water. *J Deep-Sea Research* 28A(6): 625 to 629 (1981).

A. Mohammadian and D. Y. Le Roux, Simulation of shallow flows over variable topographies using unstructured grids, *International Journal for numerical methods in fluids.* 52 473–498 (2006).

P. Moin, and J. Kim, Numerical investigation of turbulent channel flow. *J. Fluid Mech.* 118,341. (1982)

V.M. Morin, D.V. Zhu and M.R. Loewen, Supercritical exchange flow down a sill. *Journal of Hydraulic Engineering*, 130(6), 521-531(2004).

M.E. Negretti, D.V. Zhu, and G.H. Jirka, Barotropically induced interfacial waves in two-layer exchange flows over a sill. *Journal of Fluid Mechanics*, 592, 135-154 (2007).

S. Noelle, N. Pankratz, G. Puppo and J. Natvig, Well-balanced finite volume schemes of arbitrary order of accuracy for shallow water flows. *Journal of Computational Physics.* 213 474–499 (2006).

S. Nourazar, and M. Safavi. Two-Dimensional Large-Eddy Simulation of Density-Current Flow Propagating up a Slope. *J. Hydraul. Eng*. 143(9): 04017035. doi: 10.1061/(ASCE)HY.1943-7900.0001329 (2017).

J. S. O'Brien, P. J. Julien, W. T. Fullerton, Two-dimensional water flood and mudflow simulation. *Journal of Hydraulic Engineering*, 119 (1993).

C.J. Oliver, M.J. Davidson, and R.I. Nokes, Behaviour of dense discharges beyond the return point. *J. Hydraul. Eng.*, 10.1061/(ASCE)HY.1943-7900.0000781139 (2013).

OpenCFD, 2013. "OpenFOAM User and Programmer's Guide. OpenFOAM Foundation, OpenCFD Ltd." URL http://www.openfoam.com/

H. J. M. Ogink, Schatting van ruwheidslengte van zomer- bed Boven-Rijn en Waal. (in Dutch). *Rapport R2017. Water- loopkundig Laboratorium, Delft* (1986).

S. Osher, and J. A. Sethian, Fronts Propagating with Curvature Dependent Speed Algorithms Based on Hamilton-Jacobi Formulations. *J.Computational Physics*, **79**:121-49 (1988).

L. Ottolenghi, C. Adduce, R. Inghilesi, F. Roman, and V. Armenio, Large eddy simulation of gravity currents moving on upsloping boundaries. Proc., *Int. Conf. on Fluvial Hydraulics, RIVER FLOW, CRC Press, Boca Raton, FL*, 189–196 (2014).

L. Ottolenghi, C. Adduce, R. Inghilesi, V. Armenio, and F. Roman, Entrainment and mixing in unsteady gravity currents. J. Hydraul. Res., 54(5), 541–557 (2016).

T. M. Ozgokmen, and P. F. Fisher, On the role of bottom roughness in overflows. Ocean Model. 20, 336–361(2008).

T. M. Ozgokmen, P. F. Fisher, J. Duan, and T. Iliescu, Entrainment in bottom gravity currents over complex topography from three-dimensional nonhydrostatic simulations. Geophys. Res. Lett. 31, L13212, doi:10.1029/2004GL0200186 (2004).

D. Pan and J.-C. Cheng. Upwind finite-volume Navier-Stokes computations on unstructured triangular meshes. *AIAA journal,* 31(9):1618–1625 (1993).

B. Perthame and C. Simeoni, A kinetic scheme for the Saint-Venant system with a source term. *Calcolo* 38 201–231 (2001).

G. Platzman, Two-dimensional free oscillations in natural basins. *Journal of Physical Oceanography*, **2**: 117–138 (1972).

S. Pope, Turbulent flow. Cambridge University Press, Cambridge (2002).

L. J. Pratt, Rotating shocks in a separated laboratory channel flow. *J. Phys. Oceanogr.* 17, 483–491 (1987).

N. Rajaratnam, and J.K. Langat, Mixing region of circular turbulent wall jet in cross flows. *J. Hydraul. Eng.*, 10.1061/(ASCE)0733-9429 (1995).

H. Ridderinkhof, J. T. F. Zimmermann and M. E. Philippart, Tidal exchange between the North Sea and Dutch Wadden Sea and mixing time scales of the tidal basins. *Neth. J. Sea Res.,* **25**:331–350(1990).

P.J.W. Roberts, and G. Toms, Inclined dense jets in flowing current. *J. Hydraul Eng*, 10.1061/(ASCE)0733-9429 (1987).

P.J.W. Roberts, A. Ferrier, G. Daviero. Mixing in inclined dense jets." *J Hydraul Eng*, ASCE 123(8):693-699 (1997).

P.L. Roe, Approximate Riemann Solvers, Parameter Vectors and Difference Schemes. *J. Comput. Phys.;* **43**:357-372 (1981).

G. Russo and A. Khe, High order well balanced schemes for systems of balance laws, hyperbolic problems: theory, numeric and applications, *Proceedings of Symposia in Applied Mathematics*, 67 919–928 (2009).

Y. Ryu, K.A. Chang, N. Mori, J. Dispersion of Neutrally Buoyant Horizontal Round Jet in Wave Environment. *Hydr. Eng.* 131, 1088–1097 (2005).

A. J. C. de Saint-Venant, Thorie du mouvement non-permanent des eaux, avec application aux crues des rivires et a l'introduction des mares dans leur lit. C. R. Acad. Sc.Paris; 73:147–154 (1871).

D. Shao, Desalination discharge in shallow coastal waters. PhD thesis, Nanyang Technological University, Singapore (2009).

D. Shao, and L.W.K. Law, Mixing and boundary interactions of 30◦ and 45◦ inclined dense jets. *Environ. Fluid Mech.* 10.1007/s10652-010-9171-2 (2010).

D.B. Sharp, A. Shawcross, C.A Greated. LIF Measurement of the Diluting Effect of Surface Waves on Turbulent Buoyant Plumes. *Journal of Flow Control, Measurement & Visualization* 02(03):77-93 (2014)

H. Shirkhani, A. Mohammadian, O. seidou and A. Kurganov, A well-balanced positivity-preserving central-upwind scheme for shallow water equations on unstructured quadrilateral grids, *Journal of computers and Fluid 126 25 - 40 (2016).*

C.W. Shu, Total-variation-diminishing time discretization, *SIAM Journal on Scientific Statistics computing,* 9 1073–1084 (1988).

H. Shuto, and L.H. Ti, Wave Effects on Buoyant Plumes. *Proc. 14th Int. Con. Coastal Eng*., Copenhagen, 2199-2208 (1974).

P.A. Sleight, M. Berzins, PH. Gaskill and N.G. Wright, An unstructured finite-volume algorithm for predicting flow in rivers and estuaries. *Journal of Computational Fluids* 27 479-508 (1998).

B.F. Tam, and C.W. Li, Flow induced by a turbulent jet under random waves., *J. Hydraul. Eng.*, 10.1080/00221686.2008.9521926 (2008).

S. Thorpe, Laboratory observation of secondary structures in Kelvin–Helmholtz billows and consequences for ocean mixing. *Geophys. Astrophys. Fluid Dyn.* 35, 175–199 (1985).

E. F. Toro, Riemann Solvers and Numerical Methods for Fluid Dynamics. 2nd ed., Springer-Verlag (1999).

E.F. Toro, Shock capturing methods for free-surface shallow flows. John Wiley and Sons ISBN: 978-0-471-98766-6, (2001).

J. S. Turner, Buoyancy Effects in Fluids. Cambridge University Press (1973).

P. Vafeiadou, I. Papakonstantis, G. Christodoulou. Numerical simulation of inclined negatively buoyant jets." The 9th international conference on environmental science and technology, September 1-3, Rhodes island, Greece (2005).

B. Van Leer, Towards the Ultimate Conservative Difference Scheme V; A Secondorder Sequel to Godunov's Sequel. *J. Comput. Phys.* **32**:101-136 (1979).

C. B. Vreugdenhil, Numerical Methods for Shallow-Water Flow, *Kluwer Academic Publishers* (1994).

H. Wang and A. Law, Second-order integral model for a round turbulent buoyant jet, *J. Fluid Mech*. vol. 459, pp. 397–428, DOI: 10.1017/S0022112002008157 (2002).

Y.N. Wang, Y.P. Chen, Z.S. Xu, Y. Pan, C.K. Zhang, and C.W. Li, Initial dilution of a vertical round non-buoyant jet in wavy cross-flow environment. *China Ocean Eng.* ISSN: 0890-5487 (2015).

T. Weiyan, Shallow water hydrodynamics: Mathematical theory and numerical solution for a two-dimensional system of shallow water equations. *Nanjing research institute of hydrology and water resources.* Nanjing 210024, China (1992).

H. G. Wind, and C. B. Vreugdenhil, Rip-current generation near structures. *J. Fluid Mech.*; 171:459–476 (1986).

K. B. Winters, and H. E. Seim, The role of dissipation and mixing in exchange flow through a contracting channel. J. Fluid Mech. 407, 265–290 (2000)

Y. Xing and C.-W. Shu, A new approach of high order well-balanced finite volume WENO schemes and discontinuous Galerkin methods for a class of hyperbolic systems with source terms. Journal of *Communications in Computational Physics.* 1 100–134 (2006).

Y. Xing, X. Zhang, W. Shu, Positivity-preserving high order well-balanced discontinuous Galerkin methods for the shallow water equations, *Advances in Water Resources journal.* (2010).

Y. Xing, and W. Shu, A Survey of High Order Schemes for the Shallow Water Equations. *J. Math. Study*, 47: 221-249 (2014).

A. Yakhot, S. A. Orszag, V. Yakhot, and M. Israeli, Renormalization Group formulation of large-eddy simulations, *J. Sci. Comput*. 4,139 (1989).

M.A. Zeitoun, W.F. McHilhenny, and R.O. Reid, Conceptual designs of outfall systems for desalination plants. Research and development progress report no. 550. Office of Saline Water, United States Department of the Interior (1970).

D. Z. Zhu, & G. A. Lawrence, Hydraulics of exchange flows. *J. Hydraul. Eng* 126, 921–928 (2000)

D. Z. Zhu, and G. A. Lawrence, Holmboe instabilities in exchange flows. *J. Fluid Mech*., 429, 391–409 (2001).